THE HYBRID INTEGRATION OF ARSENIC TRISULFIDE AND LITHIUM NIOBATE OPTICAL WAVEGUIDES BY MAGNETRON SPUTTERING

A Dissertation

by

WEE CHONG TAN

Submitted to the Office of Graduate Studies of
Texas A&M University
in partial fulfillment of the requirements for the degree of

DOCTOR OF PHILOSOPHY

May 2011

Major Subject: Electrical Engineering

THE HYBRID INTEGRATION OF ARSENIC TRISULFIDE AND LITHIUM NIOBATE OPTICAL WAVEGUIDES BY MAGNETRON SPUTTERING

A Dissertation

by

WEE CHONG TAN

Submitted to the Office of Graduate Studies of
Texas A&M University
in partial fulfillment of the requirements for the degree of

DOCTOR OF PHILOSOPHY

Approved by:

Chair of Committee, Christi K. Madsen
Committee Members, Ohannes Eknoyan
Kai Chang
Alvin T. Yeh
Head of Department, Costas Georghiades

May 2011

Major Subject: Electrical Engineering

ABSTRACT

The Hybrid Integration of Arsenic Trisulfide and Lithium Niobate Optical Waveguides by Magnetron Sputtering.

(May 2011)

Wee Chong Tan, B.Sc., University of Saskatchewan; M.Sc., University of Saskatchewan

Chair of Advisory Committee: Dr. Christi K. Madsen

It is well known that thermally evaporated *a*-As_2S_3 thin films are prone to oxidation when exposed to an ambient environment. These As_2O_3 crystals are a major source of scattering loss in sub-micron optical integrated circuits. Magnetron sputtering *a*-As_2S_3 not only produces films that have optical properties closer to their equilibrium state, the as-deposited films also show no signs of photo-decomposed As_2O_3. The TM propagation loss of the as-deposited As_2S_3-on-Ti:$LiNbO_3$ waveguide is 0.20 ± 0.05 dB/cm, and it is the first low loss hybrid waveguide demonstration.

Using the recipe developed for sputtering As_2S_3, a hybrid Mach-Zehnder interferometer has been fabricated. This allows us to measure the group index of the integrated As_2S_3 waveguide and use it in the study of the group velocity dispersion in the sputtered film, as both material dispersion and waveguide dispersion may be present in the system. The average group index of the integrated As_2S_3 waveguide is 2.36 ± 0.01.

On-chip optical amplification was achieved through thermal diffusion of erbium into X-cut $LiNbO_3$. The net gain measured for a transverse magnetic propagation mode in an 11 μm wide Er:Ti:$LiNbO_3$ waveguide amplifier is 2.3 dB ± 0.1 dB, and its on-chip gain is 1.2 ± 0.1 dB/cm. The internal gain measured for a transverse electric propagation in an 7 μm wide Er:Ti:$LiNbO_3$ waveguide amplifier is 1.8 dB ± 0.1 dB and is among the highest reported in the literature. These gains were obtained with two 1488 nm lasers at a combined pump power of 182mW.

In order to increase further the on-chip gain, we have to improve the mode overlap between the pump and the signal. This can be done by doping erbium into As_2S_3 film using multi-layer magnetron sputtering. The Rutherford backscattering spectroscopy shows that the doping of Er:As_2S_3 film with 16 layers of erbium is homogeneous, and Raman spectroscopy confirms no significant amount of Er-S clusters in the sputtered film. The deposition method was used to fabricate an Er:As_2S_3 waveguide, and the presence of active erbium ions in the waveguide is evident from the green luminescence it emitted when it was pumped by 1488 nm diode laser.

ACKNOWLEDGEMENTS

First of all I would like to thank my advisor and committee chair, Dr. Christi K. Madsen, for her patience and guidance during the course of my studies. I am also grateful to my committee members, Dr. Ohannes Eknoyan, Dr. Chang and Dr. Alvin T. Yeh for their willingness to serve on the committee, as well as for their time and effort in following my research works.

I would also like to take the opportunity to acknowledge other people who have helped me in one way or another over the course of my research. I thank Mr. Robert Atkins and his staff, for making sure that the work place was always safe and clean, and Mr. Jim Gardner and Mr. Dennie Spears for their patience and understanding in the training and maintenance of the equipment, Dr. Lin Shao and his research group in the nuclear engineering department for assisting us with the RBS measurement in some of our samples, and Travis for depositing most of the samples reported in this work. I thank Renato C. Rabelo, and Mehmet Solmaz, for their time and effort in training me on how to make waveguides, Rafael for his guidance on the fabrication and testing of the waveguide amplifier, and Jung Hwan for the SEM. I thank all my friends and school mates, without whom this academic endeavour of mine would not have been be as enlightening and rewarding, they are Jae Woo, Won Ju, Jae Hyun, Sameer, Tim, Donnie, Xiao Min, Xia Xin, Yi Feng, Chen Qi, Wang Xin, Hui Feng, and Dehu.

Finally, I would like to share this moment with my family, for without their support and understanding, all of these would not be possible. Special thanks to my brothers and sisters for taking care of our parents when I was away. My deepest gratitude goes to my mother for her love and indulgence, and I will be forever thankful to her for never giving up on me.

TABLE OF CONTENTS

Page

Page

LIST OF FIGURES

Page

Page

Page

LIST OF TABLES

Page

1. INTRODUCTION

1.1 Background

Today, the field of optics is expanding at an explosive rate. The arrival of optical communications, personal computers, and digital television around the world has placed a heavy burden on materials and devices for signal transmission and processing. In telecommunication, the benefits of optical techniques for signal processing and transmission have already changed our lives in a major way by giving us access to the information superhighway.

At the same time, an intense research effort is currently under way to integrate multiple optical technologies onto a single chip to make smaller, faster and more power-efficient microprocessor chips than is possible with conventional technologies. Major chip manufacturer has started to integrate electrical and optical devices on the same piece of silicon, enabling computer chips to communicate using pulses of light instead of electrical signals. The following sections describe the current effort taken by two of the technology leader in the semiconductor industry.

This dissertation follows the style of Journal of Applied Optics.

1.1.1 The 50Gbps Silicon Photonics Link (by Intel)

Although innovations over recent years have enormously increased the speed of computational processes, as well as Internet bandwidths, the current technology leader, Intel Corporation, feels that the technologies that are currently in use for data transfer are already encountering their physical limits. According to Intel, there are two areas, namely data transfer via the Internet, and data transfer within and between microchips, in which new technology is needed in order to be able to maintain the speed of innovation into the future [1].

Firstly, data streams within the Internet have now reached immense proportions, and data traffic is growing from day to day. The result is a data traffic jam at the distributor center, where the data is first converted into electronic signals, sorted by routers and switches, and converted back into optical signal before being forwarded to the correct recipient. This is laborious, expensive and uses a lot of energy. An integrated optical receiver chip that could process the optical signals directly would work much faster and use less energy.

Secondly, the current technology for data transfer via metal conductor paths within computers, either between individual processor cores or the processor and the main memory, is also reaching its limits due to problems brought about by the close proximity of processors, memory and IO units (e.g. parasitic capacitance and heat dissipation) in the computer. Due to signal degradation that comes with using metals such as copper to

transmit data, the problem cannot be solved by simply placing those units far apart from one another. This therefore limits the design of computers, forcing processors, memory and other components to be placed just inches from each other. What is the use of an extremely fast processor core if it cannot transfer its data as quickly as it can process! In addition, high-speed electrical communication produces electromagnetic waves that interfere with neighboring electrical operations, since each tiny wire in a computer can act as an antenna. With optical communications, not only would interference and heating be reduced, developing low-power chips is also easier because there is less need to overpower all the interference. An integrated optical transmitter chip would not only permit today's supercomputers, which is housed in big cabinets and linked together in enormous halls, to be shrunk down to the size of a notebook, but would also revolutionize system design for microcomputer in such a way that a future data rate of more than one Terabit per second (Tbps) can be achieved using low-cost manufacturing techniques familiar to the semiconductor industry.

An integrated optical transmitter chip is shown in Fig. 1. In the upper left of the figure is the prototype of the transmitter module. It is flipped over to show the bonding pads. The block diagram in the same figure illustrates how the electrical signal from four data channels are being converted into a 50Gbps optical signal for transmission over a single optical fiber by the integrated optical circuit. The transmitter chip is composed of four hybrid silicon lasers, whose light beams each travel into an optical modulator that encodes data onto them at 12.5Gbps. The hybrid silicon laser is created by bonding

indium phosphide (InP) onto silicon. Each of the lasers has its own emitting wavelength which is determined by the grating pitch that is etched into the silicon. The light is first emitted by the indium phosphide when it is electrically stimulated. It then bounces back and forth, undergoing stimulated emission in the InP based material. The modulator is based on a Mach-Zehnder interferometer with a reverse-biased pn junction in each of the arms. When a reverse voltage is applied to the junction, free carriers are pulled out of the junction, changing its refractive index via the free-carrier effect [2]. The intensity of the light transmitted through the Mach-Zehnder interferometer is modulated by modulating the phase difference between the interferometer's two arms [3]. The optical multiplexer can be an arrayed waveguide grating, which uses constructive and destructive interference to combine light wave of different wavelength, an Echelle grating that is based on diffraction principles, or a device made up of a cascade of asymmetric Mach-Zehnder interferometers [4].

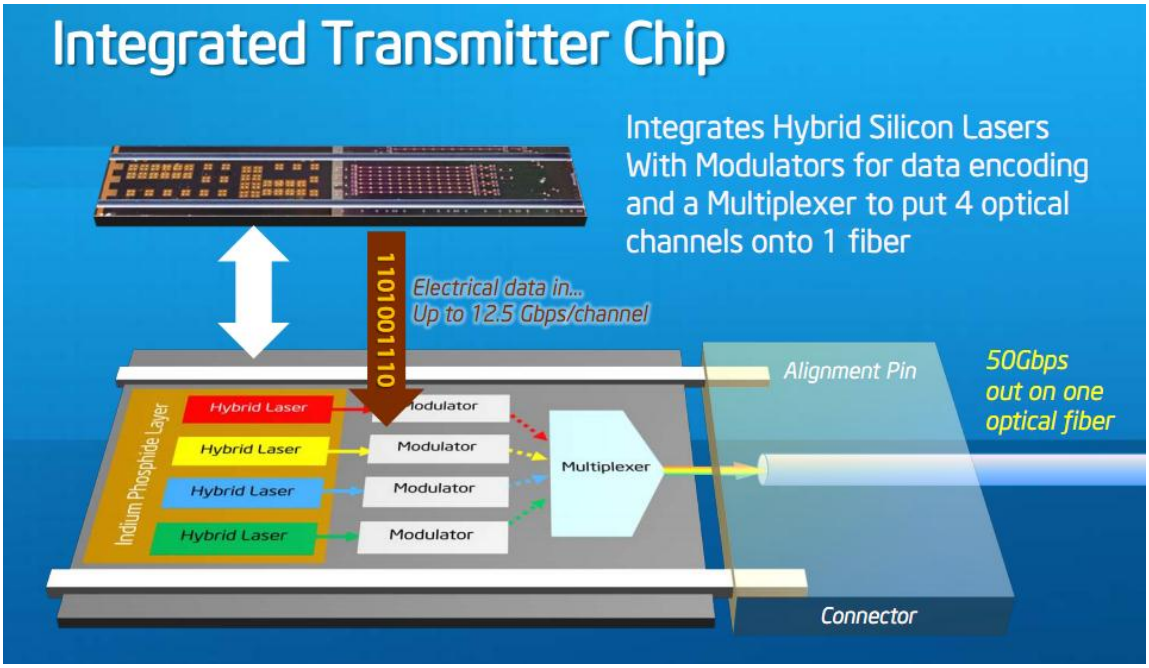

Fig. 1. An integrated optical transmitter chip. In the upper left of the picture is the physical prototype of the transmitter module. It is flipped over to show the bonding pads. The block diagram illustrates how the electrical signal from 4 data channels are converted into a single 50Gbps optical signal. (Courtesy of Intel [5])

The Fig. 2 shows an integrated optical receiver chip. In the upper right of the picture is the prototype of the receiver module with the device flipped over to show its bonding pads. The block diagram in the same figure illustrates how the electrical signal from 4 data channels are being recovered from a single optical fiber. The working principle of the demultiplexer is similar to the multiplexer while the photodetector is a silicon-based avalanche photodetector (APD) [6].

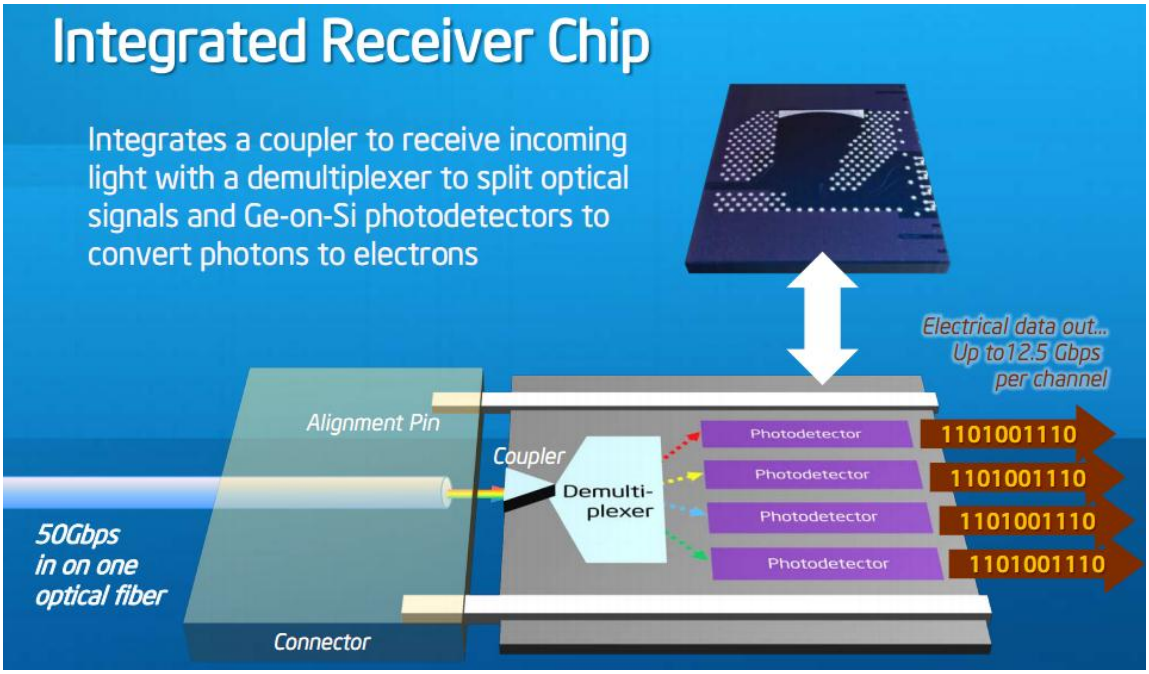

Fig. 2. An integrated optical receiver chip. In the upper right of the picture is the physical prototype of the receiver module. It is flipped over to show the bonding pads. The block diagram illustrates how the electrical data from 4 channels are being recovered from the 50Gbps optical signal transmitted by a single fiber. (Courtesy of Intel [5])

The silicon photonics data link prototype presented in 2008 worked with eight channels, i.e. eight modulators, eight lasers and eight demodulators on one chip. Each of these was able to transfer 25Gbps, amounting to a data throughput of 200Gbps. The 1000Gbps or 1Tbps tera-scale microchip that will be presented soon contains 25 channels, each with a throughput of 40Gbps. The chip will be used in optical telecommunications to avoid the bottlenecks in internet data transfers. The diagram in Fig. 3 shows how the prototype can be scaled up or scaled out to achieve a data rate of more than 1Tbps.

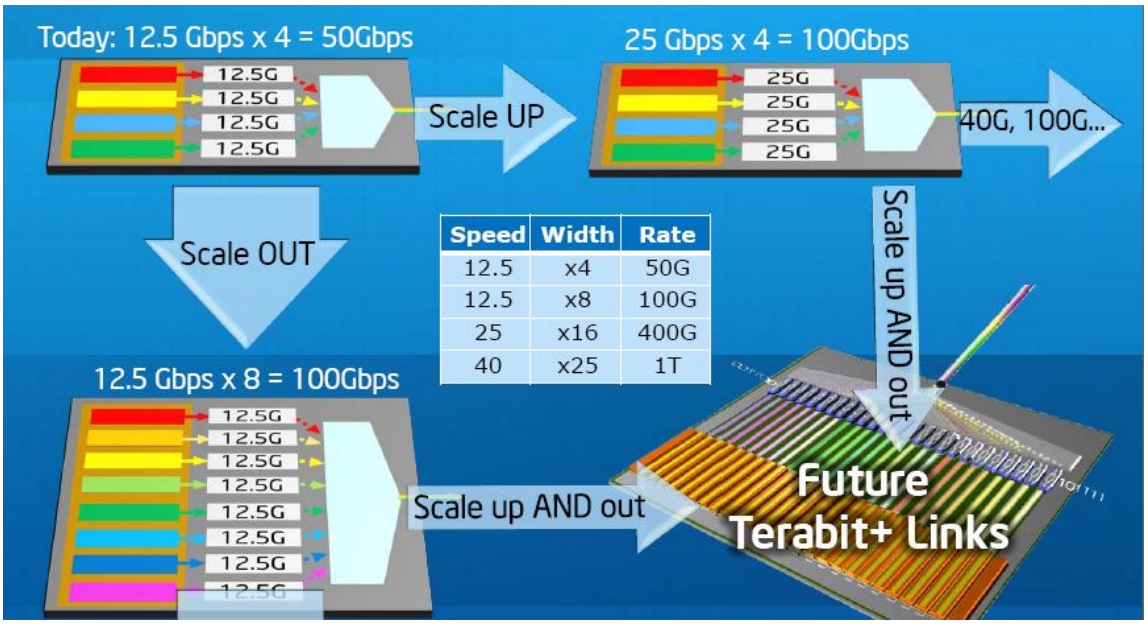

Fig. 3. The path to tera-scale data transfer rate. The diagram illustrates the different ways to increase the data rate of the prototype from 50Gbps to more than 1Tbps (Courtesy of Intel [5]).

1.1.2 Silicon Integrated Nanophotonics (by IBM)

Although both Intel (July 27, 2010) and IBM (December 1, 2010) announced advances in the quest to use light beams to replace the use of electrons to carry data in and around computers, there are some difference in their approach toward this objective at the moment. One of the major differences is that Intel started off by making its CMOS and nanophotonic devices separately and then bonding them together, while IBM begin by trying to integrate them all on the same piece of silicon. According to IBM, this future 3D-integated chip consists of several layers connected with each other with very dense

and small pitch interlayer vias. The lower layer is a processor itself with many hundreds of individual cores. Memory layers are bonded on top to provide fast access to local caches. On top of the stack is the photonic layer with many thousands of individual optical devices (modulators, detectors, switches) as well as analogue electrical circuits (amplifiers, drivers, latches, etc.). The key role of a photonic layer is not only to provide point-to-point broad bandwidth optical link between different cores and/or the off-chip traffic, but also to route this traffic with an array of nanophotonic switches [7].

IBM's technology today consists of an optical transceiver unit with six optical communication links. The optical chip itself has more than one transmitter and receiver, each capable of handling six channels of data through the multiplexing technology. Also built in are modulators, which control the laser that generates the light signals. The laser itself is a separate component. Each modulator can manage bandwidth of 20Gbps, a major step toward IBM's goal of a chip with an aggregate capacity 1Tbps. For reference, today's conventional Ethernet operates at 1Gbps and sometimes at 10Gbps in higher-end servers. A capacity of 1Tbps would be enough to transfer the data of 26 DVDs in a second. The nanoscale silicon photonics circuits that are being developed here are targeted to enable the monolithic integration of complete optical systems on a semiconductor chip [8].

The role of an integrated optical circuit will only expand further when the advances in the integration of various optical functions finds its way into sensor applications in transportation, medicine, biotechnologies, and environmental pollution detection.

1.2 Lithium Niobate as a Substrate for Integrated Optical Circuits

Lithium niobate as a substrate is a very versatile material for integrated optics. An array of new optical devices based on this material, including waveguide structures, electro-optical wavelength filters and polarization controllers, lasers with remarkable properties, nonlinear frequency converters of exceptional efficiency, ultrafast all-optical signal processing devices and single photon sources have been demonstrated to date [9].

We use lithium niobate as the substrate material because it is a mature technology with good long-term stability, and it has a strong electro-optic coefficient that leads to low drive voltages. Other advantages are its low optical loss and its capability to operate at high frequencies. For example, high speed $LiNbO_3$ based modulator operating at 40Gbps had already been demonstrated in 2000, while Intel researchers were only able to match this speed with a silicon modulator in 2007 [10]. Optical modulators are essential in any signal processing system and are used to encode a high-quality data signal onto an optical beam, effectively by turning the beam on and off rapidly to create ones and zeros. Before the year 2004, no one had built an optical modulator from silicon that was faster than about 20 MHz.

Although silicon photonics have reach an important milestone in the fabrication of integrated optical circuits, the followings components are still missing in the technology. They are ultra-low threshold lasers (low power is key), high power optical amplifiers, short pulse mode locked lasers, optical isolator, polarizer, and polarization controller. Among those listed, $LiNbO_3$ based isolator, polarizers, and polarizer controller, are very serious contenders because $LiNbO_3$ by nature is birefringent, where light of different polarization will travel at different speed inside the material depending on how the wafer is diced. We described in the following the various components that $LiNbO_3$ based devices has an advantage over silicon photonics.

One important aspect of optical signal is the state of polarization, or the way in which an electromagnetic wave is restricted in the direction of vibration. A polarizer is a device that converts a beam of electromagnetic waves (light) of undefined or mixed polarization into a beam with well-defined polarization. The common types of polarizers are linear polarizers and circular polarizers. Polarizers are used in many optical techniques and instruments. Since $LiNbO_3$ is by nature birefringent, polarization angle in a $LiNbO_3$ based waveplate can be easily fabricated by cutting the wafer in certain way, e.g. rectangular or wedge shaped.

Optical fibers are not perfectly circular, and the polarization is split into two different components that propagate at different speeds. Polarization mode dispersion (PMD) is a

form of modal dispersion where two different polarizations of light in a waveguide, which normally travel at the same speed, travel at different speeds due to random imperfections and asymmetries, causing random spreading of optical pulses. Unless it is compensated, which is difficult, this ultimately limits the rate at which data can be transmitted over a fiber. A polarization controller is used to continuously rotate the polarization of input beams of electromagnetic energy at a certain, predetermined angle. Other than being used to compensate for PMD in fibers, a polarization controller or rotator is also used in an optical isolator and multiplexer. Many $LiNbO_3$ based polarization controllers have been demonstrated [11, 12]. Other than polarization controllers, $LiNbO_3$ based isolators have also been demonstrated [13]. An optical isolator is an optical component which allows the transmission of light in only one direction. It is typically used to prevent unwanted feedback into an optical oscillator, such as a laser cavity.

Besides its versatility, the fabrication process of an optical channel waveguide with low insertion and propagation loss in lithium niobate has been well-studied. It is reliable and has been used for more than 10 years. Typical lithium niobate waveguides are made using titanium-indiffusion or proton exchange. The resulting waveguides have low optical confinement and are weakly guiding structures with relatively large waveguide cross-sections and thus large mode distributions. This effectively means they can only achieve low loss for bend radii larger than about one centimeter in the 1400 nm to 1620 nm wavelength range without incurring excess loss. This bend radius restriction

substantially limits the number of optical devices and functions operating in the low loss optical fiber transmission wavelength window that can be fabricated on a single substrate. Consequently, the type and quality of optical filtering that can be realized on-chip is exceedingly limited [9]. However, this problem can be resolved with the integration of As_2S_3 waveguides on top of the $LiNbO_3$.

1.3 Arsenic Trisulfide as an Optical Material for Integrated Optics

Amorphous As_2S_3 (*a*-As_2S_3) belongs to a group of amorphous semiconductors called the chalcogenide glasses, which contain a non-oxide group VI element (S, Se, or Te) as one of their components. It is photosensitive when exposed to near bandgap energy (E_g ~ 2.35 eV) and has a wide optical transmission band extending roughly from 0.7 to 10 μm. It's high refractive index and low processing temperatures allow very compact optical interconnects to be fabricated on different substrate materials, and their nonlinear coefficient is two orders of magnitude larger than that of silica [14-16]. This property has gained increasing recognition and has led to a number of recent demonstrations of all-optical processes including switching, regeneration, wavelength conversion, amplification, lasing, pulse compression, and slow light [17]. All these properties make *a*-As_2S_3 an attractive candidate for advancing the next generation of integrated optics and biochemical sensors [18-23].

Being a glass, the chalcogenides are a versatile platform. Apart from bulk optic components, chalcogenide glass fiber and planar waveguide devices have been

developed. Importantly chalcogenide glasses can be formed with a variety of compositions and doped with additional elements, e.g. rare earth elements, to provide further functionality [24-26].

The main reasons a chalcogenide host such as As_2S_3 is particularly suited as a host for erbium are that it has very low phonon energies and it does not inherently contain any hydroxyl or silicon oxide groups. Hosts with low-phonon energy hosts are desired for rare-earth ions because multi-phonon relaxation pathways can result in a rapid depopulation of the upper excited state and cause quenching of the photoluminescence.

On the other hand, hosts with inherent hydroxyl or silicon oxide groups will not only exhibit optical absorption at around 950 nm, 1240 nm, and 1400 nm, the presence of the IR absorption of Si-O species will also introduce a band-tail, which marks the long-wavelength limit of the second telecommunications window. Furthermore, the presence of impurities also causes Rayleigh scattering which determines the short wavelength limit of the amplifier.

From here, we can see that if a chalcogenide glass such as As_2S_3 is doped with erbium, the devices fabricated with this material can potentially access the entire telecommunications spectrum from 1200 nm wavelength to 1600 nm wavelength thus enabling access to an extra 100 nm or 25 % more wavelength channels over silica based devices [27].

1.4 Erbium as a Material for Optical Amplification

Erbium is a chemical element in the lanthanide series, with the symbol Er and atomic number 68. A silvery-white solid metal when artificially isolated, natural erbium is always found in chemical combination with other elements on Earth. This lanthanide series begins with the element lanthanum (Z = 57) and ends with the elements lutetium (Z = 71). The elements of this series are generally found in the +3 oxidation state and the 4f shell can accommodate a total of 14 electrons.

The lanthanides display a very interesting property in its electronic configuration due to the shielding of the partially filled 4f shell by the electrons on the outer shells. This shielding has the effect that the energy levels of this 4f shell are largely insensitive to the environment that they reside in. As a result, the atomic-like energy levels of the rare-earth element do not drastically change as they are inserted into a crystalline or amorphous host material. Due to these unique optical properties, the elements in the lanthanide series are often employed in a wide variety of host matrices as a dopant that will provide the host material with their unique features without altering the properties of its host drastically.

From among the lanthanides series, the element erbium has emerged as one of the most important rare-earth elements for telecommunications. The Er^{3+} ion contains 11 electrons in its 4f shell and the ground state is labeled as $^4I_{15/2}$. The electrons from this

ground state can be promoted to any one of the higher energy states through the absorption of a photon with a corresponding energy. The trivalent erbium ion, Er^{3+}, exhibits a strong emission band that is situated around 1535 nm wavelength from the emission of a photon due to the transition of an electron from the $^4I_{13/2}$ meta-stable state to the $^4I_{15/2}$ ground state. The $^4I_{13/2}$ is the meta-stable state that exhibits long luminescent lifetimes, which enable this atom to sustain population inversion long enough for an efficient amplification process to be carried out in this material [27].

One of the most important applications of erbium today is its inclusion into silica to form the erbium doped fiber amplifier (EDFA). The EDFA has become a very important component in optical telecommunications as they are routinely used for signal boosting during long-distance signal transmission to maintain signal quality. The EDFA is particularly attractive because it allows the amplification of an optical signal without the need to first convert the optical signal into an electrical signal before the amplification. This resulted in a dramatic simplification of the equipment used in the overall network. Moreover, with the advent of high-capacity communication network that employs wavelength division multiplexing to increase the number of channels carried by the signal, erbium's unique broad gain spectrum in the telecommunication window help makes EDFAs an essential and integral part of any existing long-haul optical data carrier network in used today.

Due to its prominence in the telecommunications field, great research effort has been placed on Er-doped materials. The host materials for the Er can be crystalline, such as Si, SiC, GaAs, and $LiNbO_3$ (lithium niobate) or amorphous, such as silica, alumina and in chalcogenide glasses. All of these systems have advantages as hosts for the Er^{3+} ions. However, we will pay particular attention to the advances of erbium doping in $LiNbO_3$ and As_2S_3 hosts because of the interest in these materials in our current work.

1.5 Sputtering as a Deposition Method for As_2S_3 Waveguide

Thin film deposition basically can be divided into physical vapor deposition or chemical vapor deposition. Currently, the more popular methods for depositing As_2S_3 film involve the use of a physical vaporization technique. Physical vapor deposition (PVD) is a general term used to describe any deposition methods which deposit thin films by the condensation of a vaporized form of the material onto a substrate. In other words, As_2S_3 material in its bulk or pallet form is first vaporized into the gas-phase and then subsequently collected onto a substrate to form a thin film. Some of the more common PVD methods are electron beam evaporation, thermal evaporation, pulsed laser deposition, and magnetron sputtering.

Electron beam evaporation is a physical vapor deposition in which the material to be deposited is heated to a high vapor pressure by electron bombardment in high vacuum, Thermal evaporation is similar to electron beam but the material to be deposited is heated to a high vapor pressure by electrically resistive heating in relatively lower

vacuum. Pulsed laser deposition is also a PVD in which a high power laser ablates material from the target into a vapor. Lastly, in magnetron sputtering, a highly localized glow plasma discharge bombards the material and sputters some material away as a vapor. These various types of vaporization techniques can be divided into two main categories that depend on the gas-phase species that are generated.

The first category of vaporization techniques uses a highly intense energy source that interacts with the As_2S_3 precursor for a very short time. Due to the short interaction time between the incident energy source and the source material, local heating is dominant and complete thermal fragmentation of the material cannot be achieved. Therefore, these vaporization techniques do not cause any significant bond dissociation or rearrangement in the material that is emitted or ejected from the source. The technique that exhibits this behavior is magnetron sputtering, where fast ion-bombardment impacts and dislodges material into the gas-phase, with a chemical composition and structure that is similar to that of the precursor at the source. Although there are some who would put electron beam evaporation and pulsed laser deposition into the same category as magnetron sputtering, in the case of an As_2S_3 film, they actually belong to the category best represented by thermal evaporation [27]. This observation is based on the optical properties reported for As_2S_3 film prepared by these techniques and will be made clear in section three.

In contrast to the first, the second category of vaporization techniques is known for producing As_2S_3 films that are significantly different both chemically and structurally from the As_2S_3 precursor. It is best described by the thermal evaporation deposition. As mentioned earlier, thermal evaporation is similar to electron beam evaporation except that the As_2S_3 to be deposited is heated to a high vapor pressure by electrically resistive heating. It is a well-known technique used for producing photosensitive thin films of As_2S_3. This vaporization technique involves the use of an oven which allows the precursor at the source to be thermally heated in a slow and controllable manner, thus enabling a more complete fragmentation of the precursor glass to take place. In this process, the As_2S_3 glass precursor, usually in pallet form, is thermally heated in a high-vacuum environment until it evaporates into the gas-phase. Fig. 4 shows the schematic diagram of a thermal evaporator for the deposition of amorphous selenium film.

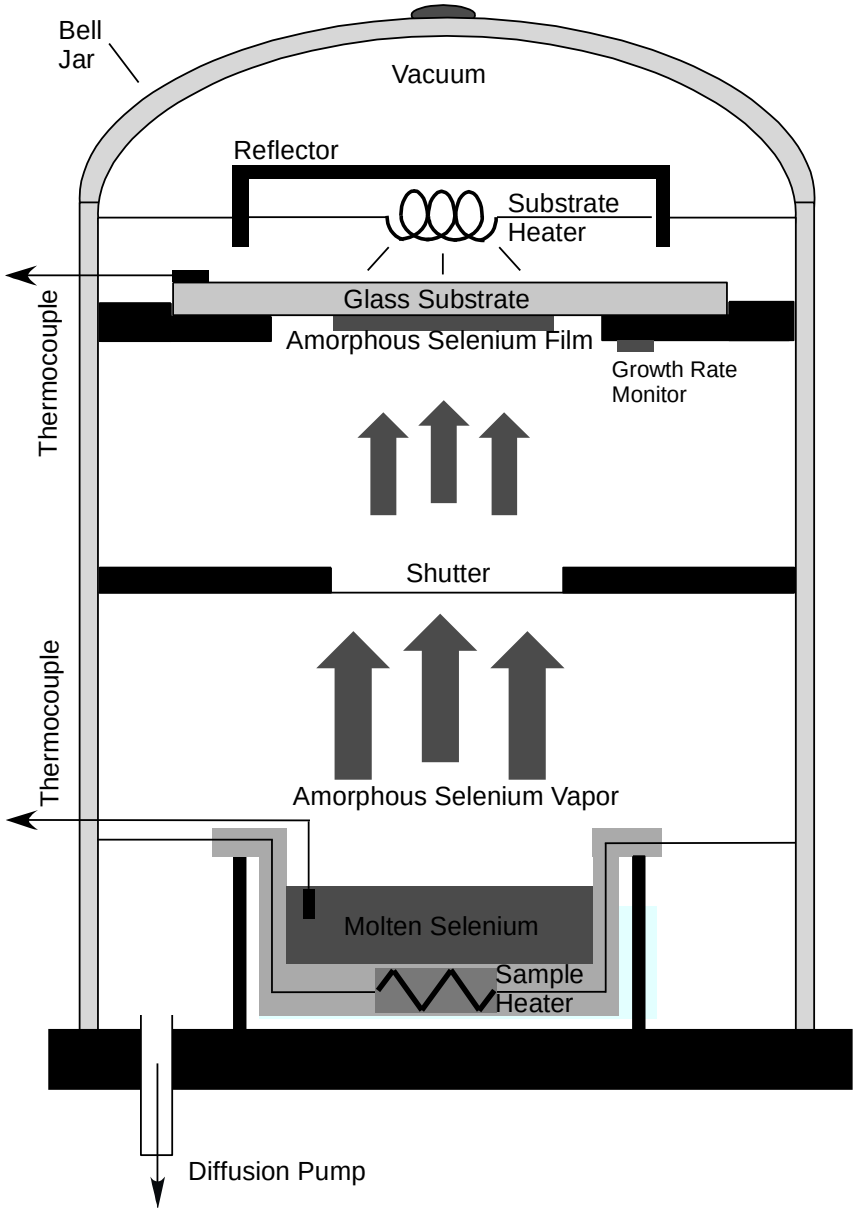

Fig. 4. Schematic diagram of a thermal deposition system. The figure shows the typical features of an evaporator and the deposition process of an amorphous selenium film [28].

During the evaporation process of As_2S_3, the precursor glass defragments and rearranges in the gas-phase to yield individual molecular fragments or "monomers". Due to the

random gas-phase fragmentation process, a host of arsenic and sulfur molecules can be identified in the gas-phase. However, the most abundant molecular fragments that have been identified in the gas-phase, and collected on the substrate, are the molecules of S_8, As_4S_4 and As_4S_6. Once the As_2S_3 precursor has been fragmented into this monomer form, it can then be re-polymerized via the use of light sources with sufficient photon energies. The entire thermal evaporation process takes place in a high vacuum chamber to reduce contamination from oxygen and water, and also serves to lower the boiling point of the As_2S_3 precursor thus allowing lower heating temperatures to be used. Using this method, it is possible to produce thin films composed of molecules that are chemically and structurally different from the original bulky As_2S_3 [27].

Although thermal evaporation seems to be an ideal method for producing a photosensitive film, it has some serious disadvantages when it is used in the fabrication integrated As_2S_3 waveguide. Again, this will be explained in section three where we will show why magnetron sputtering is more superior to other methods when it comes to the deposition of As_2S_3 thin film for making integrated optics.

1.6 Research Objective and Dissertation Outline

The main purpose of this work is to demonstrate the viability of the fabricating As_2S_3 waveguides with magnetron sputtering and also the feasibility of integrating them on $LiNbO_3$ substrate with on-chip optical amplification.

The dissertation is divided into a total of six sections. Following this introductory section, a brief literature review of amorphous semiconductors, chalcogenide glass, and As_2S_3, will be given in Section 2. The magnetron sputtering of As_2S_3 thin film and the fabrication process of a hybrid straight waveguide and an integrated Mach-Zehnder interferometer can be found in Section 3. Section 4 will describe in detail how on-chip amplification can be achieved with the diffusion of erbium into the substrate and section 5 introduces the novel method of doping erbium into As_2S_3 thin film by multi-layer magnetron sputtering. Section 6 summarizes all the findings and provides the conclusions of this work.

2. A LITERATURE REVIEW ON AMORPHOUS ARSENIC TRISULFIDE

2.1 Background

In order to gain some measure of understanding of the unique electronic and optical properties of amorphous arsenic trisulfide, a theoretical grasp of the energy band structure of an amorphous semiconductor is required. This can be done by applying quantum mechanics to an amorphous system. However, due to the absence of periodicity, or more specifically the loss of long range order in an amorphous material, quantum mechanical methods that so effectively predict the behavior of crystalline semiconductors become mathematically too complex to apply in such a system. As a result, the behavior of an amorphous semiconductor cannot be derived in the same manner as in a crystalline material but are determined by studying the energy band structure that was mapped from observations obtained from various rigorous experiments. The section will begin with a brief introduction to an amorphous solid in general before narrowing down to the discussion of chalcogenide glasses and specifically amorphous arsenic trisulfide. Part of the theory reported in this section is reprinted from the reference in the literature [28].

2.2 The Atomic Structure of Amorphous Solids

All solids that do not have long range periodicity in their arrangement of its atoms can be termed as amorphous or “structureless”. They are best defined when compared to a crystalline solid which has a distinctive regular spatial arrangement of atoms throughout

the whole material. In fact they are often simply referred to as non-crystalline materials. Although their structure appears random over the long range, an amorphous substance still has a high degree of short range spatial order in its atomic structure. This is because individual atoms in an amorphous solid must still fulfill their requirement for valence bonding. However, unlike their crystalline counterpart, there are some small deviations in the bonding angles between adjacent atoms and this leads to a disruption of the periodicity in the material. Fig. 5 illustrates the difference between a crystalline and an amorphous solid.

2.3 Band Theory of Amorphous Semiconductors

Although an amorphous semiconductor is a non-crystalline material, the band theory of amorphous semiconductors is closely related to its crystalline counterpart. The theory was called the band theory because when quantum mechanics was applied to a crystal, bands of allowable energy states were brought into existence. Besides these bands of allowable states, which are often grouped into two principle bands labeled as the valence and conduction bands, there is also a bandgap separating the two bands where no electron states can exist. Very often the density of states (DOS) diagram is used to explain or predict the properties of a material in the band theory. It denotes the number of electron states per unit energy per electron, g(E), a material will have at an energy level and is used successfully to describe many of the characteristics found in a crystalline semiconductor.

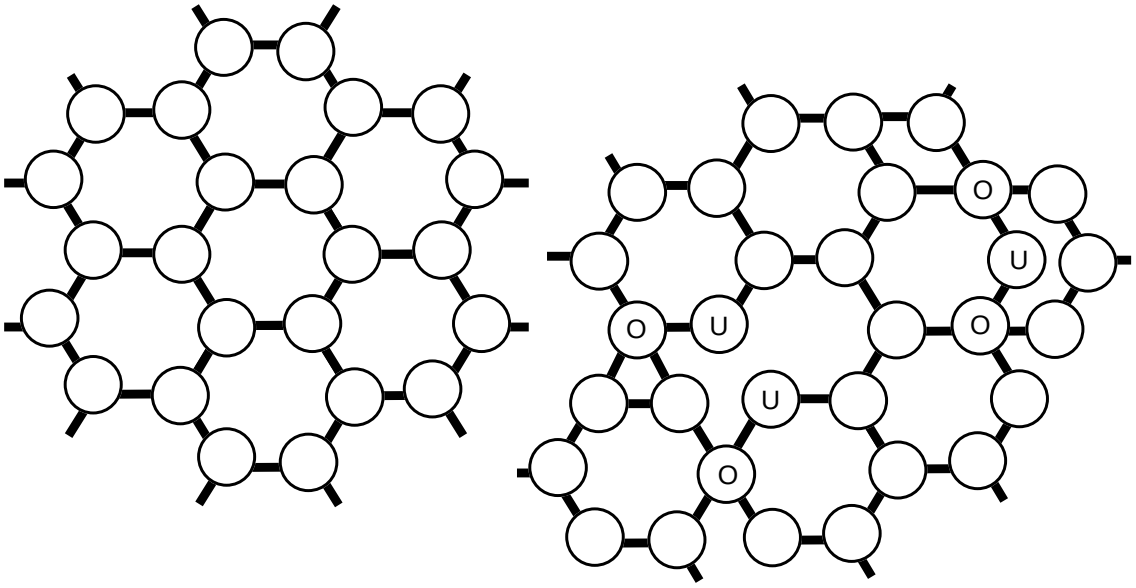

(a) (b)

Fig. 5. An illustration of a crystalline and an amorphous solid. Two dimensional representation of the structure of (a) a crystalline solid and (b) an amorphous solid. Atoms marked “O” represent over-coordinated atoms with more than usual numbers of bonding with adjacent atoms and “U” represent under-coordinated atoms with less than the usual number of bonds with adjacent atoms.

When it was discovered that amorphous and crystalline semiconductors shared the same basic electronic and optical properties, it immediately led to the thinking that the DOS of the amorphous semiconductor might be similar to that of its crystalline counterpart and not completely different as it was thought initially. This can be seen in the three popular density of states models proposed shown in Fig. 6. In the figure, the hatched regions denote localized states, which is different from the extended states in the conduction band. As can be seen in the Fig. 6 (a), the energy bandgap of a crystalline semiconductor is defined as $E_g = E_c - E_v$, where the starting energy level of the conduction band is

denoted as E_c and the highest energy level of the valence band is denoted as E_v. There are no available states within this energy gap. This is in contrast to the energy bandgap of an amorphous semiconductor shown by the three models in Fig. 6 (b), (c), and (d). In all of these models, the energy gap where no states are available is always smaller than the bandgap of a crystalline semiconductor, $E_g = E_c - E_v$. The energy bandgap of an amorphous semiconductor is usually refers to as the optical bandgap and can be obtained from an optical spectrometer [28]. Lastly, the Fermi level, E_F, in the figure represents the energy of the highest occupied quantum state an electron can have at absolute zero temperature.

One important difference between crystalline and amorphous semiconductors is the existence of localized states in the mobility gap. Unlike the extended states found in the two principal bands, electrons in the localized states are not free to travel anywhere in the material and thus have zero mobility. While some of these localized states are created by defects, the majorities of them are created by the loss of long range order and is unique to solids which are amorphous.

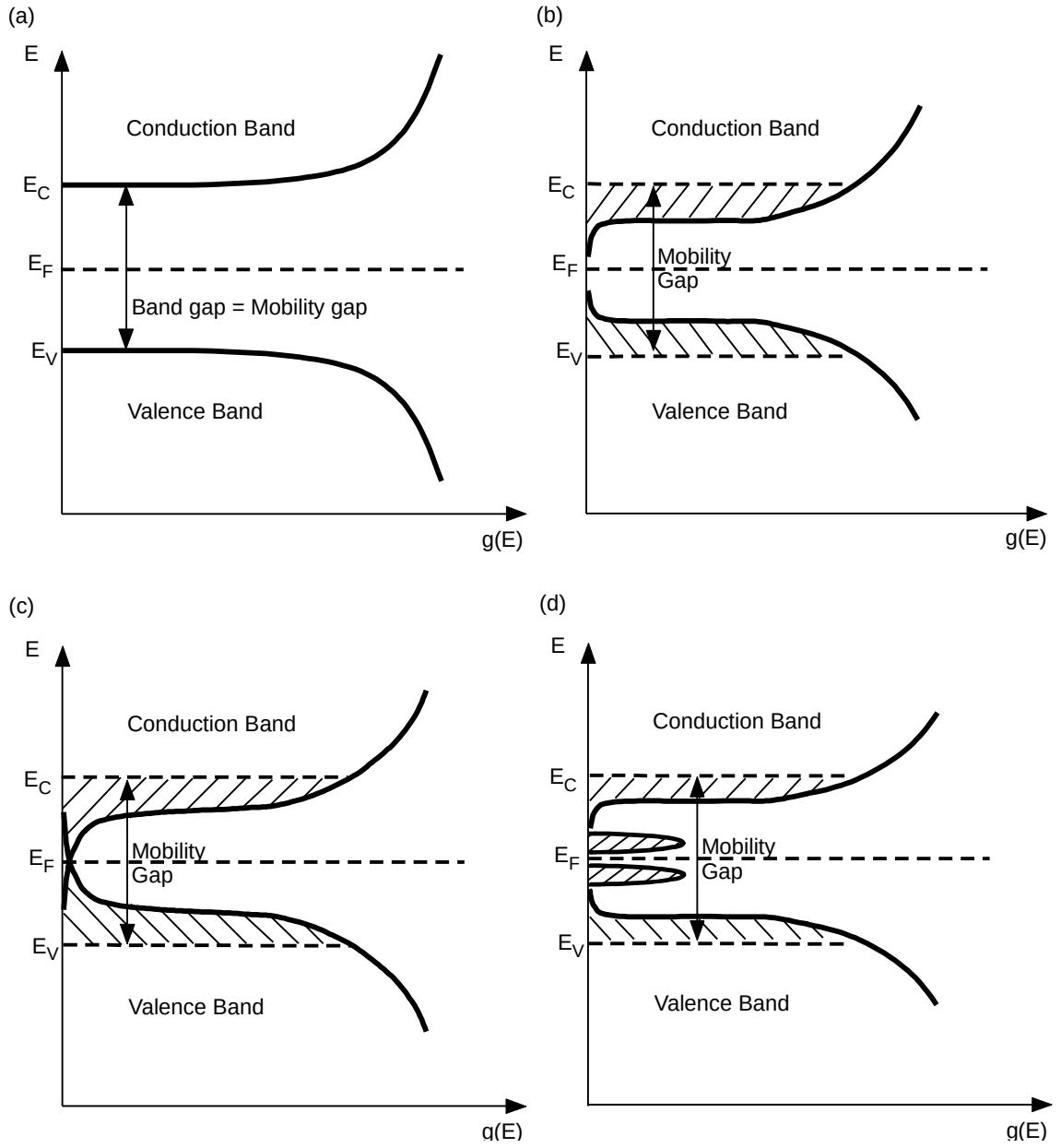

Fig. 6. Density of states model of amorphous semiconductor. (a) DOS of a crystalline semiconductor; (b) DOS models proposed by Mott [29], (c) DOS models proposed by Cohen, Fritzsche and Ovshinski (CFO) [30], and (d) DOS models proposed by Marshall and Owen [31]. The hatched regions denote localized states. Note: the x-axis in all the 4 figures is logarithmic**.** E_c refers to the starting energy level of the conduction band and E_v refers to the highest energy level of the valence band. E_F is the Fermi level, which represents the energy of the highest occupied quantum state an electron can have at absolute zero temperature.

2.4 The Optical Properties of Amorphous Semiconductors

In general, the optical properties of a material describe how the characteristics of light are affected when it passes through it. The two most important optical constants are the refractive index n and absorption coefficient α. The refractive index of an optical material or dielectric medium is generally defined as the ratio of the speed of light c in vacuum to its velocity v in the medium. In materials where an electromagnetic wave can lose its energy during propagation, the refractive index becomes complex. The real part of this complex refractive index N is the refractive index n while the imaginary part is referred to as the extinction coefficient K, which is related to the absorption coefficient α through $K = c\alpha / 2\omega$, where ω is the frequency of interest. While the importance of the absorption coefficient, which dictates how readily photons will be absorbed by the material, can be understood from the viewpoint of a photoconductor, the interest in the refractive index, which ultimately determines the coupling and guiding of optical signal, and the amount of dispersion, is important in the engineering of optical waveguides. Although our understanding of these two properties in amorphous semiconductors is limited and not complete, some perspectives on the optical properties of amorphous semiconductor can still be gained from the proposed models.

2.4.1 The Absorption Coefficient of Amorphous Semiconductor

The absorption edge of many amorphous compound semiconductors has the shape that looks like the one depicted in Fig. 7. There will be a high absorption region A, which is

also referred to as the fundamental absorption edge, where the absorption coefficient is $\alpha > 10^4 \text{cm}^{-1}$. An exponential region B, which is usually referred to as the Urbach edge and has values that extend over 4 orders of magnitude of α, and a weak absorption tail C called the Urbach tail. Very often the density of states proposed by different models mentioned previously in section 2.3 is used to describe optical transitions in semiconductors. The basic difference between models used for crystalline semiconductors and those used for amorphous semiconductors is the change in the character of the wavefunctions, some of which no longer extend over the whole volume of the sample but become localized over a certain volume.

Many semiconducting glasses have been observed to have absorption, α that has the following frequency dependence in the region where the absorption is high, i.e. region A of Fig. 7,

$$\alpha\hbar\omega(\omega) = A\left(\hbar\omega - E_g^{opt}\right)^r, (\alpha \geq 10^4 \text{ cm}^{-1}) \quad (1)$$

where A and r are physical constants that depend on the material properties, $\hbar\omega$ is the energy of the photon and E_g^{opt} is a parameter that has been called optical bandgap energy.

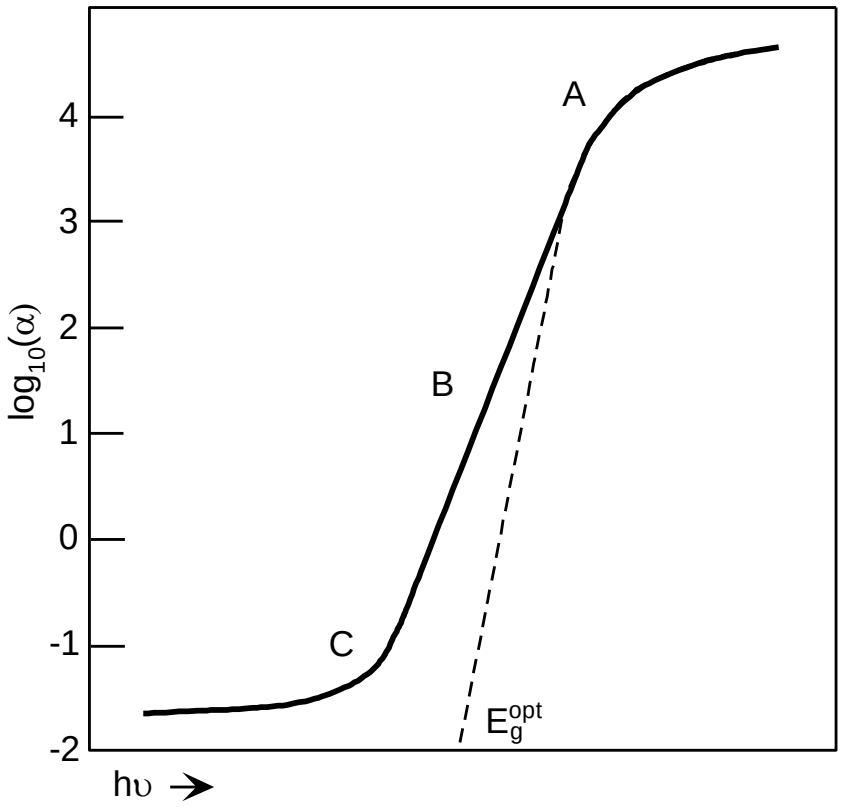

Fig. 7. A typical absorption edge of an amorphous semiconductor. In the figure, A represents a region where $\alpha \geq 10^4 \text{cm}^{-1}$, called the fundamental absorption edge, B represents a region changing exponentially, which is referred to as the Urbach edge, and C represents a region referred to as the weak absorption tail or Urbach tail. E_g^{opt} is the optical bandgap [32].

In many direct bandgap crystalline semiconductors, r has been found to have a value of $r = 2$ and $A = 10^5$ to $10^6\ \text{cm}^{-1}\ \text{eV}^{-1}$. Many amorphous semiconductors also have $r = 2$ (e.g. a-Si:H, As_2Se_3 etc.) while some complicated glasses have $r = 3$, and $r = 1$ for a relatively simple glass, such as a-Se [32, 33].

In the exponential region B of the absorption edge of Fig. 7, whose existence was said to be the evidence of the presence of localized states, the absorption coefficient was found to have the following properties. Firstly, it has a frequency dependency of the form: $\alpha(\upsilon) \propto \exp(h\upsilon/\Delta E)$, where ΔE is the energy characterizing the slope. Secondly, at low temperatures, usually below room temperature, the energy ΔE is almost temperature independent and has, in many semiconducting glasses, the value between 0.05 eV and 0.08 eV. While at high temperatures, $\Delta E \propto T$. Lastly, in many amorphous semiconductors except *a*-Se, parts A and B of Fig. 7 move as a whole [32]. In a crystalline semiconductor, similar exponential tails have been observed and these tails are usually referred to as Urbach edges. The theories of the Urbach edge are based on the idea that the sharp absorption edge is broadened by some kind of mechanism. In ionic crystals it is the optical phonons which are responsible for the Urbach edges. Although developed for crystals, the Urbach edge was successfully applied to the temperature dependence of the absorption edge of *a*-Se .

Of the three absorption regions in Fig. 7, part C is the most difficult to study. This is because absorption at such low levels may only be apparent or false due to the possibility that it might be light scattering or simply noise in the system. This absorption tail lies below the exponential part of the absorption edge B and its strength and shape were found to depend on the preparation, purity and thermal history of the material, and vary very little with its thickness. Nevertheless it is still possible to study the optical transition in this region if the sample is properly prepared. This can be seen when light

scattering had been experimentally tested on the sample with an absorption tail shown in Fig. 8. In this experiment, the attenuation that is due to scattering was found to be α_{scatter} ≈ 0.04 per cm for a sample that was free of large macroscopic inhomogeneities. This is about an order of magnitude lower than the absorption level in the region of the weak absorption tail, as can be seen in Fig. 8. Similar results were also observed for other chalcogenide glasses [32].

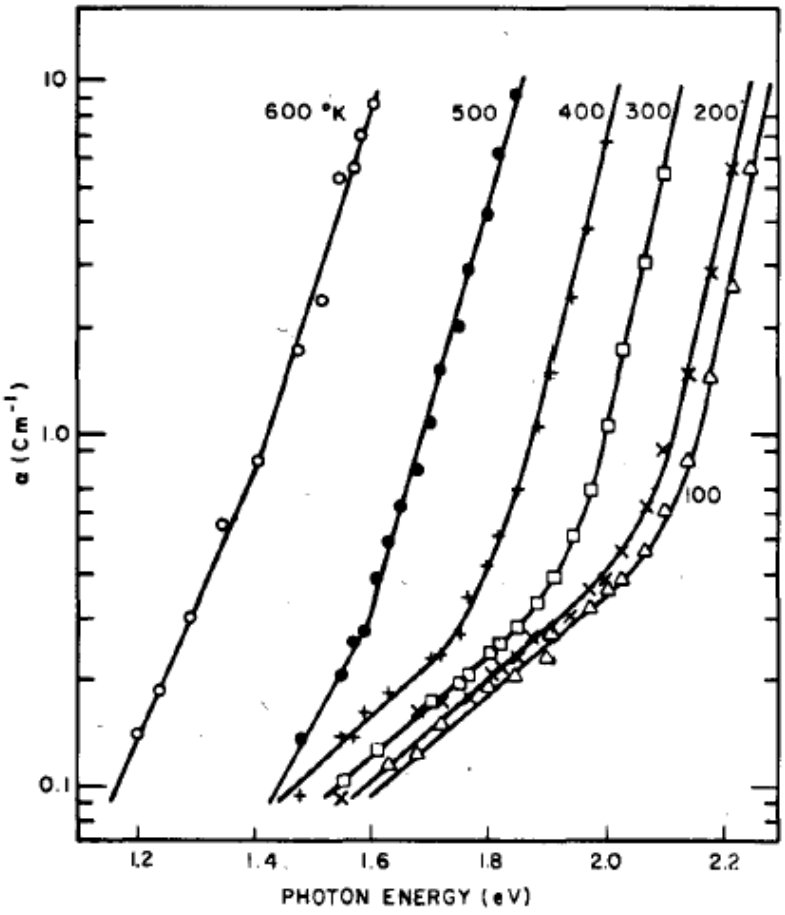

Fig. 8. The weak absorption tail of *a*-As_2S_3. The absorption edge of *a*-As_2S_3, at low absorption levels at various temperatures [32].

There are two possible forms of optical transitions in this region, i.e. part C of Fig. 7, that are considered to be most probable. First, the optical transitions may be of the kind that corresponds to electron transitions from an impurity ion to an ion of the host lattice, or vice versa, that is the initial and final states are localized at different centers. Although one has observed formulations of similar tails in crystals, it has not been studied quantitatively. Second, the optical transitions may be of the kind that is similar to what was suggested for the exponential region B of the absorption edge in Fig. 7. This is to say that the initial state is localized and the final state is extended, or vice versa.

In summary, Tauc compared the absorption edge of amorphous and crystalline As_2S_3 and showed that the high absorption ($\alpha > 10^4$ cm^{-1}) region was mostly associated with transitions from localized valence band states below E_v to conduction band states above E_c (delocalized), or vice-versa. For 1 $cm^{-1} < \alpha < 10^4$ cm^{-1}, the absorption was declared to be due to the presence of band tail states that extends into the gap. The third region of the band ($\alpha < 1$ cm^{-1}) was found to be related to the preparation, purity and thermal history of the material.

2.4.2 Index of Refraction

As mentioned earlier, the refractive index *n* of an optical or dielectric medium is defined as $n = c/v$, where *c* is the velocity of light in vacuum and *v* is the velocity in the medium.

In a lossy material, this refractive index becomes complex and can be expressed as $N = n - jK$, where N is the complex refractive index, n is the refractive index and K is the extinction coefficient.

The optical constants, n and K can be determined by measuring the reflectance from the surface of a material as a function of polarization and the angle of incidence. For normal incidence, the reflection coefficient, r, is obtained as

$$r = \frac{1-N}{1+N} = \frac{1-n+jK}{1+n-jK} \tag{2}$$

and thus the reflectance R is,

$$R = |r|^2 = \left|\frac{1-n+jK}{1+n-jK}\right|^2 = \frac{(1-n)^2 + K^2}{(1+n)^2 + K^2} \tag{3}$$

So by fitting this equation to the measured reflectance R at normal incidence, the optical constants, n and K can be calculated [34]. The refractive index, n is also related to the relative permittivity through an equation derived from the Maxwell's equations, which is $n = (\varepsilon_r \mu_r)^{1/2}$, where ε_r is the static dielectric constant or relative permittivity and μ_r is the relative magnetic permeability. This equation associates the dielectric properties of a material to its optical properties.

For a lossy nonmagnetic medium, where $\mu_r = 1$, both its refractive index and relative permittivity will have an imaginary component that represent the attenuation. If the complex static dielectric constant is given by

$$\varepsilon_r = \varepsilon_r' - j\varepsilon_r'' \tag{4}$$

where ε_r' and ε_r'' are just the real and imaginary part of the complex permittivity respectively, then from $N = (\varepsilon_r \mu_r)^{1/2}$, it will become $n - jK = \sqrt{\varepsilon_r' - j\varepsilon_r''}$, and thus either

$$n^2 - K^2 = \varepsilon_r' \tag{5}$$

and

$$2nK = \varepsilon_r'' \tag{6}$$

or

$$n = (1/\sqrt{2})[\sqrt{\varepsilon_r'^2 + \varepsilon_r''^2} + \varepsilon_r']^{1/2} \tag{7}$$

and

$$K = (1/\sqrt{2})[\sqrt{\varepsilon_r'^2 + \varepsilon_r''^2} - \varepsilon_r']^{1/2} \tag{8}$$

The above equations, Eq. (5) to Eq. (8), relate the complex relative permittivity of the material to its index of refraction regardless of the mechanism of loss. Since the optical properties of materials are typically presented either by showing the frequency dependencies of *n* and *K* or ε_r' and ε_r'', a link to the complex permittivity allows us to relate macroscopic optical properties, like *n* and *K* to a microscopic properties such as electronic polarizability, α_e. This can be done through a model used for the study of dielectric dispersion in material. The model is based on a single oscillator, in which the

electric field of the incident EM wave induces dipole oscillations in the material with a single resonant frequency ω_o, in such a way that

$$\varepsilon_r' = 1 + \frac{N_{\text{at}}}{\varepsilon_o}\alpha_e' \tag{9}$$

and

$$\varepsilon_r'' = 1 + \frac{N_{\text{at}}}{\varepsilon_o}\alpha_e'' \tag{10}$$

where N_{at} is the number of atoms per unit volume, ε_o is the permittivity of free space, and α_e' and α_e'' are the real and imaginary parts of the electronic polarizability, given respectively by:

$$\alpha_e' = \alpha_{eo}\frac{1-(\omega/\omega_o)^2}{[1-(\omega/\omega_o)^2]^2 + (\gamma/\omega_o)^2(\omega/\omega_o)^2} \tag{11}$$

and

$$\alpha_e'' = \alpha_{eo}\frac{(\gamma/\omega_o)(\omega/\omega_o)}{[1-(\omega/\omega_o)^2]^2 + (\gamma/\omega_o)^2(\omega/\omega_o)^2} \tag{12}$$

where α_{eo} is the DC polarizability corresponding to $\omega = 0$ and γ is the loss coefficient that characterizes the attenuation of the EM wave within the material system [34].

There are several popular models describing the spectral dependence of refractive index *n* in a material. Such dispersion relationships are essential in designing photonic devices, such as waveguides. In the *Cauchy* equation, the dispersion relationship is commonly described as follows:

$$n = A + \frac{B}{\lambda^2} + \frac{C}{\lambda^4} \tag{13}$$

where *A*, *B* and *C* are material dependent constants determined through curve fittings, *n* is the refractive index and λ is the wavelength. It is typically used in the visible spectrum region for various optical glasses. Besides Cauchy's dispersion model, there is also the *Sellmeier* equation, which is an empirical formula made up of a series of lossless single dipole *Lorentz* oscillator terms, each of which having the same wavelength dependence of the type $\lambda^2/(\lambda^2-\lambda_i^2)$ with different strengths, i.e.

$$n^2 = 1 + \frac{A_1\lambda^2}{\lambda^2-\lambda_1^2} + \frac{A_2\lambda^2}{\lambda^2-\lambda_2^2} + \frac{A_3\lambda^2}{\lambda^2-\lambda_3^2} + \ldots \tag{14}$$

where the *Sellmeier coefficients*, A_i *and* λ_i, with integer i = 1,2,3,…, are determined through curve fitting. Since any number of resonance type or oscillator terms can be summed together to get as wide a range of wavelength dependence as possible with this model, it is the most popular dispersion relation. Its main drawback is that it does not accurately represent the refractive index when there is a contribution arising from free carriers in narrow bandgap or doped semiconductors [34].

Another model that is based on the single oscillator is the *Wemple-DiDominico* equation. It is a semi-empirical dispersion relation for determining the refractive index at photon energies below the inter-band absorption edge. It is expressed as:

$$n^2 = 1 + \frac{E_o E_d}{E_o^2 - (h\upsilon)^2} \tag{15}$$

where υ is the frequency, *h* is the Planck constant, E_o is the single oscillator energy and E_d is the dispersion energy which measures the average strength of inter-band optical

transitions. It is given by $E_d = \beta N_c Z_a N_e$ (eV), where N_c is the effective coordination number of the cation nearest-neighbor to the anion, Z_a is the formal chemical valency of the anion, N_e is the effective number of valence electrons per anion excluding the cores, and β is a two-valued constant that depends on whether the inter-atomic bond is ionic or covalent ($\beta_i = 0.26 \pm 0.03$eV and $\beta_c = 0.37 \pm 0.04$eV respectively). It was said that E_d (corrected for differences in densities) depends on the short range order only and is the same in the crystalline and amorphous forms if the short-range order (the first coordination number) is the same [35].

The refractive index of a semiconductor (typically for $h\upsilon < E_g$) usually decreases with increasing energy bandgap E_g. There are various empirical and semi-empirical rules and expressions that relate n to E_g. In the *Hervé-Vandamme* relationship [36],

$$n^2 = 1 + \left(\frac{A}{E_g + B} \right)^2 \tag{16}$$

where A and B are constants, typically $A \approx 13.6$eV and $B \approx 3.4$eV. The temperature dependence of n arises from the variation of E_g with temperature T and typically increases with increasing temperature.

2.5 Photoinduced Phenomena in Chalcogenide Glasses

Chalcogenide glasses (ChG) are amorphous semiconductors formed by the addition of other elements such as As, Ge, or Ga, into chalcogen elements, S, Se, and Te. These glasses have low phonon energy and are generally transparent from the visible up to

infrared. They are sensitive to the absorption of electromagnetic radiation and show a variety of photoinduced effects as a result of illumination. Chalcogenide glasses can also be doped with rare-earth elements, such as Er, Nd, Pr, etc., and thus have applications in active optical devices. It was shown that impurities only play a predominant role in determining the optically-induced properties of arsenic chalcogenides when it is in the crystalline state [37]. In other words, the doping of rare-earth elements ("impurities") into chalcogenide glasses should not affect the photo-induced properties of As_2S_3.

On the other hand, as the glass state is characterized by the lack of thermodynamic equilibrium, all the physical properties of the glasses are time dependent, and this behavior is generally referred to as a physical aging phenomenon. To avoid the changes in physical properties caused by physical aging, a material with completely saturated aging should be used in chalcogenide-based devices. However, natural physical aging requires years at low temperatures; therefore, γ-ray irradiation, photo-exposure, and thermal annealing are usually applied to accelerate the relaxation process [38].

A study was conducted, using differential scanning calorimetry (DSC) to identify the physical parameters that are uniquely related to the aging process, on an amorphous As_2S_3 film deposited by ultra-fast laser ablation method. Firstly, although no crystalline composition was found in the as-deposited film and bulk materials, a substantial amount of crystalline phase had formed in those films annealed above 160°C for 15 hours. The formation of crystalline phase was also found on samples annealed at 140°C for more

than 200 hours, suggesting that the crystalline phase could be formed even at a lower annealing temperature at a very slow rate. The study also shows that unlike a pulsed laser deposited film, As_2S_3 bulk glass is strongly resistant to crystallization [38]. Similar study using DSC has not been carried out on a magnetron sputtered As_2S_3 film.

Due to the low coordination of chalcogens that made amorphous chalcogenides more structurally flexible, several distinct photoinduced phenomena can be observed in amorphous chalcogenides upon illumination with electromagnetic radiation having photon energy near the optical band gap of the chalcogenide. These changes are usually accompanied by changes in their physical and optical properties, i.e. thickness, refractive index and absorption coefficient, and thermal annealing chalcogenide glasses can affect these photoinduced changes. In particular, irreversible effects can occur in as-deposited films, while reversible effects occur in well-annealed films as well as bulk glasses. In the following, we will describe some of the main photoinduced phenomena found in chalcogenide glasses that will be relevant to the fabrication of As_2S_3 waveguides.

Photodecomposition is a process whereby the chemical content of the chalcogenide glass is irreversibly changed when it is exposed to electromagnetic radiation. It was used to explain the dissociation of As_2S_3 film, and the formation of S and As_2O_3 crystals at the surface of the exposed film by Berkes as follows [39]:

$$As_2S_3 \xrightarrow{h\upsilon} 2As + 3S \tag{17}$$

The liberated arsenic on the surface then oxidizes in the following manner:

$$4As + 3O_2 \xrightarrow{H_2O} 2As_2O_3 \quad (18)$$

Photodarkening is a process whereby the optical bandgap of the chalcogenide glass is reversibly reduced and its absorption band edge is shifted toward lower energies when it is exposed to electromagnetic radiation. The refractive index usually increases as a result. Thermal annealing the film near its glass-transition temperature can erase the "darkened" state and this process is often referred to as photo-bleaching. Fig. 9 shows the reversible photodarkening process of a thermally evaporated chalcogenide film taken from a study in the literature [39]. Reversible photo-structural changes are defined as modifications induced by light in amorphous bulk and thin films, which when annealed below the glass transition temperature can be cancelled or reversed by thermal treatment. The photo-exposure was conducted with a 632.8 nm laser at an intensity of 10^{16} photons per cm^2 per sec. First of all, curve A-to-B in the figure represents the temperature dependent transmittance of a virgin As_2Se_3 film which has not been exposed to light. If a sample is cooled from A-to-B, i.e. from room temperature to 120 K, subsequently photodarkened with a laser from B-to-C and allowed to heat up to room temperature again, it will finally attain a transmittance specified by D and not the virgin state at A.

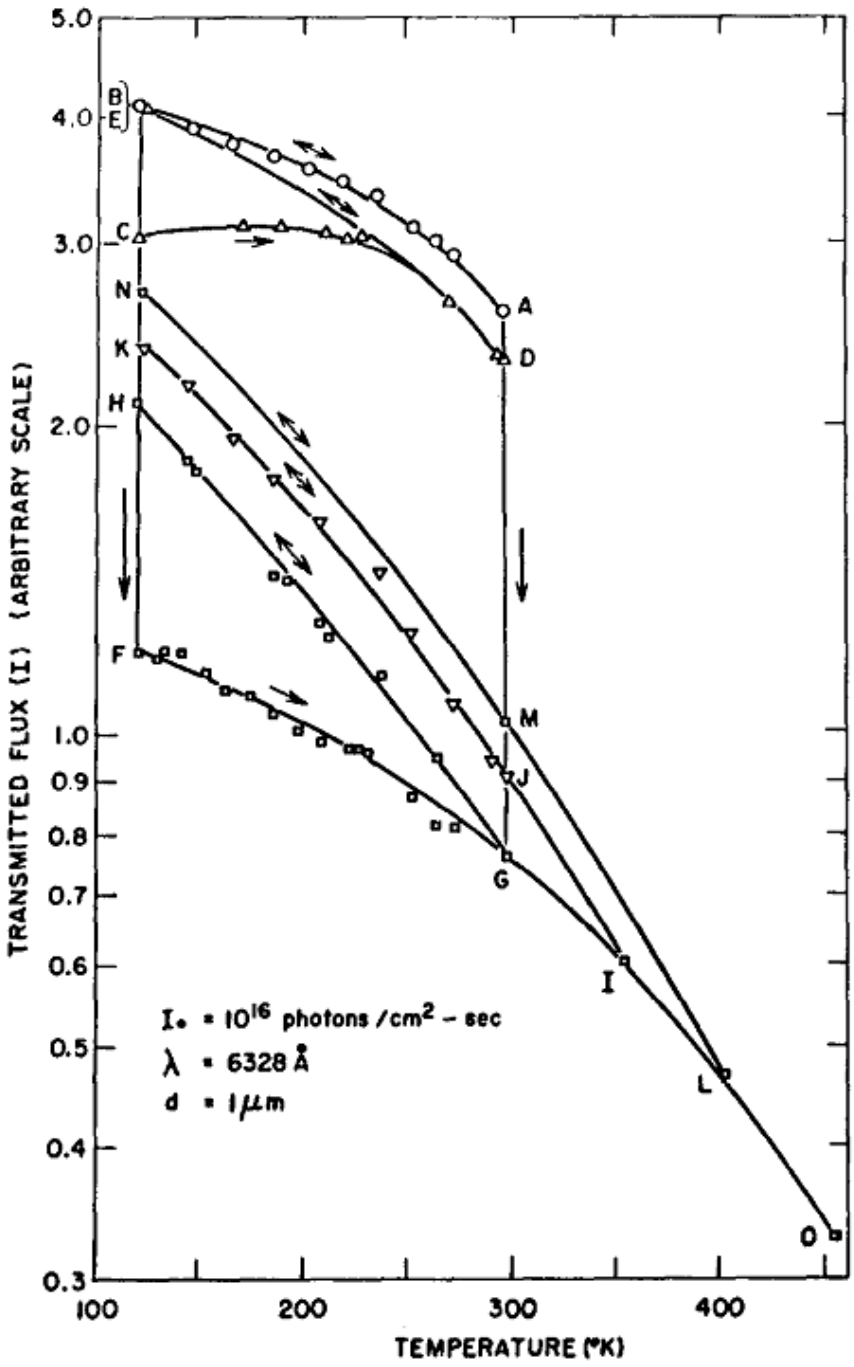

Fig. 9. Reversible photodarkening process of As_2Se_3. The arrows indicate possible traverse directions. All vertical arrows represent isothermal exposures and all other arrows indicate temperature dependent optical density paths traversable in complete darkness by an As_2Se_3 film. The arrows also indicate whether any particular path can be traversed reversibly or not [39].

Furthermore, when this sample is again cooled to 120 K, the transmittance curve followed is not D-to-C but D-to-E. The net result is that the average optical transmission of this material is now approximately equal or greater than the initial value at B. The line D-to-E can be reversibly traversed, indicating that the material has attained a reasonable stable phase state different from the virgin material. Repeated traversing of the loop E-to-C-to-D-to-E is possible by cycling the sample through exposure, heating and cooling. If an as-deposited film were exposed to light at room temperature and optically densify from A-to-G. Subsequent heating by thermal annealing to L and cooling back to room temperature would result in a transmittance level specified by M. Repeated traversing of the loop M-to-G-to-L-to-M is also possible by cycling the thermally evaporated sample through exposure, annealing and cooling [39]. From the figure, we can see the effect of thermal history on the transmittance of the chalcogenide film. For example, depending on the annealing temperature, heating the film with a transmittance at G to either 350 K or 400 K can cause the film to have either a lower transmittance at J or a higher transmittance at M when the film cooled down to room temperature at 300 K.

Other than photodecomposition and photodarkening, photo-induced volume change in As_2S_3 also has a major impact on the design of an As_2S_3 waveguide. This is because the effective index that control the propagation constant of the optical signal is determined by the physical thickness and width of the waveguide. Although several studies

conducted on thermally evaporated on glassy As_2S_3 film have demonstrated an 0.5% expansion in the thickness after illumination, the mechanism of the photoexpansion is still regarded as speculative because x-ray structural studies have not been able to provide reliable results to account for the macroscopic expansion phenomenon [40]. It was also shown that the photoexpansion can be recovered with annealing at the glass-transition temperature of 470 K, and the phenomenon can occur concurrently with photodarkening [41]. In the extreme case, a thermally evaporated As_2S_3 film can experience a giant photo-expansion of about 5 % upon illumination with a He-Ne laser ($h\nu$ = 2.0 eV) for roughly 10 s [42].

3. FABRICATION OF AS_2S_3 WAVEGUIDES BY MAGNETRON SPUTTERING

3.1 Background

Even though the As_2S_3 bulk glasses offer large third-order optical nonlinearities and low optical losses, As_2S_3 films are well known to exhibit physical properties that are different from their bulk counterparts. For instance, the as-grown films prepared by laser ablation or thermal evaporation always include molecular clusters and cross-linked bonds, which degrade the network of the glass. Moreover, different phases of these clusters may coexist in the films. Although thermal annealing can accelerate the structural relaxation of amorphous films, complete transformation from homopolar (total dipole moment is zero) covalent bonds to heteropolar (non-zero dipole moment) covalent bonds cannot be achieved [38]. As a result, there are always structural differences between the films prepared by laser ablation or thermal evaporation and the bulk material [43-46].

A major motivation for magnetron sputtering *a*-As_2S_3 is that it not only produces films that are structurally closer to the equilibrium state of a bulk glass, the as-deposited films also show no significant amount of As_2O_3 crystals in them when they are exposed to the ambient environment. This is especially important for the fabrication of *a*-As_2S_3 waveguides, as very often the as-deposited *a*-As_2S_3 film prepared by resistive thermal evaporation or pulsed laser deposition, will oxidize into As_2O_3 when it comes into contact with oxygen in the ambient environment [39, 47, 48]. Since these crystals can be

numerous and are usually big enough to serve as a scattering centre for any light propagating in the film, they can be the main source of scattering losses in an optical waveguide with sub-micron thicknesses. Even though a number of advanced processing methods have been proposed to solve these problems, the proposed methods in the literature still require the breaking of vacuum after the film is deposited and so will not effectively stop the oxidation process in the *a*-As_2S_3 film [43-46].

In this section, we will report on the chemical and optical properties of a magnetron sputtered *a*-As_2S_3 thin film and the fabrication of various hybrid *a*-As_2S_3 waveguides [49]*.

3.2 The Characterization of a Magnetron Sputtered *a*-As_2S_3 Film

While the optical properties and propagation loss of *a*-As_2S_3 have been studied by several authors, they were either using bulk glasses or thin films prepared by methods other than magnetron sputtering [16, 50, 51]. Since *a*-As_2S_3 film is a photosensitive material and the emission spectra of the argon plasma contains spectra lines well within the optical bandgap of As_2S_3, it is reasonable to suspect that *a*-As_2S_3 film made by magnetron sputtering can have properties different from those made by other deposition techniques. This is the reason we have to investigate its optical properties.

3.2.1 Experimental Technique

Films of *a*-As_2S_3 were deposited in room temperature on glass slides (~ 20 mm by 20 mm), silicon wafers (~ 10 mm by 10 mm), and titanium diffused lithium niobate wafers (~ 23 mm by 20 mm) in a magnetron sputtering system using a commercially available 2-inch AMTIR-6 target (Amorphous Materials, Inc., Garland, TX 75042). The sputtering was done at a low pressure of ~ 0.6 mTorr with the argon gas flowing at a rate of 50 sccm and a RF power of 8W. The sample was placed 8 cm away from the target, the deposition rate from the crystal thickness monitor was about 1.0 Å/s, and the average deposition time was 50 minutes. A thermal conductive paste was applied on the As_2S_3 target to improve its thermal conductivity with the sputtering gun. The substrate holder and the target were both water cooled to 15 °C. Fig. 10 shows a typical 3-gun magnetron sputtering system and the basic operation of a magnetron sputtering process. The main difference between magnetron sputtering and other sputtering methods is the application of magnetic field around the target. The magnetic field enhances the plasma in the system by trapping the electrons in such a way that they are always around the target. As a result, the system will have higher argon ionization and bombarding rate, and thus a higher deposition rate even at low working pressure.

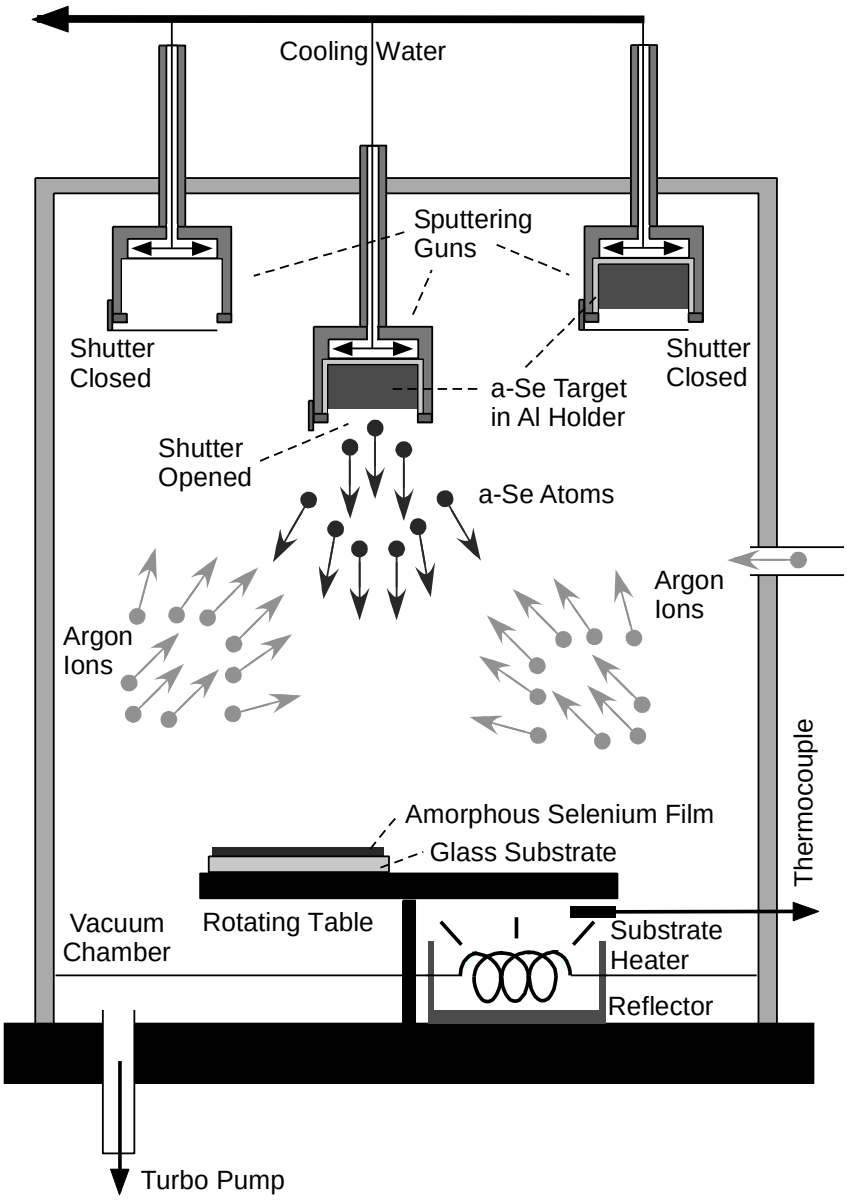

Fig. 10. A typical 3-gun magnetron sputtering system. The diagram illustrates the basic operation of a magnetron sputtering process. The main difference between magnetron sputtering and other sputtering methods is the application of magnetic field around the target. This will trap electrons around the target and enhances the plasma in system. As a result, the system will have higher ionization of argon atoms and thus increased deposition rate [28].

The refractive index n, extinction coefficient κ, and the thickness of the film, which includes the non-uniformity of the thickness, were measured by reflection spectroscopy over the wavelength range of 400 – 850 nm (F20, Filmetrics, Inc., San Diego, CA 921123). The average non-uniformity of the films was around ± 15 nm and the film's thickness was independently verified with a surface profiler. The variations in the measured thickness among the spectrometer, crystal thickness monitor, and surface profiler, were within ± 20 nm. In order to obtain the optical properties beyond the measured range, the real part of the measured dielectric constant of the film, $\varepsilon_1 = n^2 - \kappa^2$, was fitted to the Drude model. The refractive index beyond the wavelength range of 400 – 850 nm was then obtained by subtracting the extinction coefficient κ that was curve fitted to a logistic function from the real part of the dielectric constant of the film. In order to find out whether there are any differences in the optical properties between the as-deposited and the annealed films, thermal annealing was conducted in the dark at around 5 mTorr in an annealing oven at 160 °C for 2 hours.

The magnetron sputtered *a*-As_2S_3 film was visually inspected for As_2O_3 surface crystals at × 1000 magnification using an optical microscope fitted with a polarizer. In order to quantitatively analyze the elements at the surface, x-ray photoelectrons spectroscopy (XPS) was also carried out with a Kratos AXIS ULTRA system (Kratos Analytical Inc., Chestnut Ridge, NY 10977) on the *a*-As_2S_3 film and the As_2S_3 sputter target. XPS is a quantitative spectroscopic technique that measures the elemental composition, empirical formula, chemical state and electronic state of the elements that exist within a material.

The XPS spectra were obtained by irradiating a material with a beam of X-rays while simultaneously measuring the kinetic energy and number of electrons that escape from the top 1 to 10 nm of the material being analyzed. The instrument was calibrated using carbon 1s line (Binding Energy = 284.8 eV) as a reference energy. Any shifts in the binding energy of the carbon 1s line were used to correct the binding energy of the As_2S_3 obtained from the high resolution scan to the surface of the film and the target. The analyzer is set to spectrum mode, the resolution is 40 eV, the current is 10 mA, and the anode HT is 12 kV. The End eV for each elements, namely O 1s, C 1s, S 2p, and As 3d, are all set to be 3 eV lower than the default value. The sweeps time is 60 s and the number of sweeps was five.

3.2.2 Results and Discussion

Table 1 contains the average optical properties of 26 magnetron sputtered *a*-As_2S_3 films that were measured immediately after the deposition. As seen from the table, the average refractive index of the as-deposited film is higher than those made from resistive thermal evaporation and pulsed laser deposition. The average Tauc's optical bandgap, E_{op}, is 2.35 eV and the reproducibility calculated was about 0.9% for the index of refraction n and 2.3% for the optical bandgap E_{op}.

Table 1. The optical properties *a*-As_2S_3. The average optical properties, refractive index n and absorption coefficient α, of *a*-As_2S_3 bulk glasses and as-deposited thin films prepared by magnetron sputtering, thermal evaporation and PLD. The reproducibility, 2σ deviations, of the refractive index taken from 26 sputtered samples with thicknesses ranging from 184 to 484 nm was around 1%.

λ (nm)	**Sputtered *n***	**Bulk *n* [50]**	**Ref. *n***	**Ref. Method of Deposition**
632	2.586	2.617	2.44	Resistive Thermal Evaporation [52]
810	2.497	2.522	2.46	Pulsed Laser Deposition [46]
1150	2.437	2.460	2.33	Resistive Thermal Evaporation [52]

λ (nm)	**Sputtered α (per cm)**	**Bulk α (per cm) [16]**
454	4.1×10^4	3.8×10^4
643	7.6×10^1	7.8×10^1

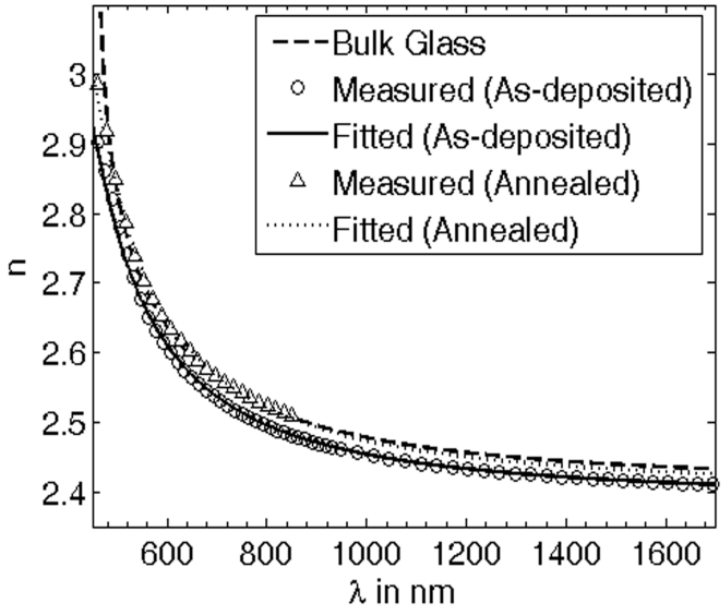

Fig. 11. The refractive index of *a*-As_2S_3. The refractive index of a magnetron sputtered *a*-As_2S_3 thin film (as-deposited and annealed) and a bulk As_2S_3 glass taken from the literature. The thickness of the film was 377 ± 20 nm and goodness of fit was 0.990. The measured result of the as-deposited film was obtained from a spectrometer with an extended measuring range from 400 – 1700 nm (F20EXR, Filmetrics, Inc., San Diego, CA 921123).

The Fig. 11 describes the wavelength dependency of the refractive index of a magnetron sputtered *a*-As_2S_3 thin film and compares it to an As_2S_3 bulk glass reported in the literature [50]. It shows how close the refractive index of a magnetron sputtered film is to the bulk glass. In addition to the index of refraction, Fig. 12 shows the absorption coefficient of an As_2S_3 bulk glass, an as-deposited and an annealed magnetron sputtered *a*-As_2S_3 thin film, and a thermally evaporated *a*-As_2S_3 thin film that has been exposed to bandgap light [16, 51]. It can be seen that the absorption coefficient of the annealed

magnetron sputtered film approaches the value of the As_2S_3 bulk glass [39]. This is different from the evaporated *a*-As_2S_3 film, whose absorption coefficient only approaches the bulk glass when it was exposed to bandgap light, for example, from a 514.5nm Argon laser. In fact, the absorption coefficient of the as-deposited film prepared by magnetron sputtering was closer to the As_2S_3 bulk glass than those (i.e. S-Unexposed) prepared by thermal evaporation.

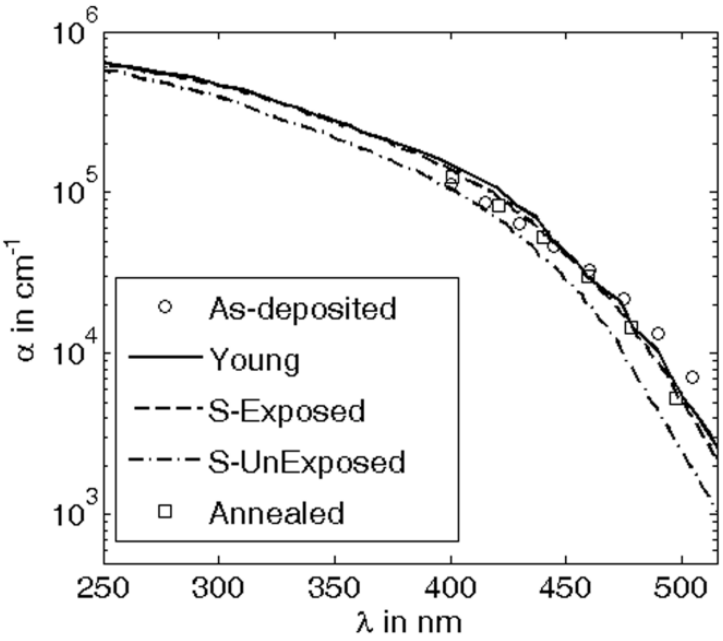

Fig. 12. The absorption coefficient of *a*-As_2S_3. The absorption coefficient of a As_2S_3 bulk glass taken from Young, and *a*-As_2S_3 thin films prepared by magnetron sputtering (as-deposited and annealed) and thermal evaporation (exposed and unexposed to bandgap light) taken from Keneman. The thickness of the magnetron sputtered film was 377 ± 20 nm.

Table 2. The optical properties of an annealed *a*-As_2S_3 film. The average optical properties, refractive index *n* and absorption coefficient α, of *a*-As_2S_3 bulk glasses and thermally annealed thin films prepared by magnetron sputtering, thermal evaporation and PLD. The reproducibility, 2σ deviations, of the refractive index taken from 10 sputtered samples with thicknesses ranging from 184 to 484 nm was around 2%. N.A. refers to data not available.

λ (nm)	**Sputtered *n***	**Bulk *n* [50, 53]**	**Ref. *n***	**Ref. Method of Deposition**
632	2.599	2.617	2.598	Resistive Thermal Evaporation [52].
810	2.508	2.522	2.52	Pulsed-Laser Deposition [46].
1014	2.450	2.476	N.A.	
1150	2.448	2.460	2.453	Resistive Thermal Evaporation [52].
1530	2.425	2.438	N.A.	

λ (nm)	**Sputtered α (per cm)**	**Bulk α (per cm) [16]**
454	3.5×10^4	3.8×10^4
643	4.0×10^1	7.8×10^1

The Table 2 contains the average optical properties of 10 thermally annealed *a*-As_2S_3 films prepared by magnetron sputtering. As it can be seen from the table, these values are around those reported for bulk glass and other thin film deposition methods [16, 46, 52, 53]. The average optical bandgap, E_{op}, of an annealed film from the Tauc plot was 2.37 eV and was also within the published value for As_2S_3 bulk glass [54, 55]. The

reproducibility, 2σ deviations, calculated was about 2.1% for the index of refraction *n* and 0.6% for optical bandgap E_{op}. By comparing the results in Table 1 and Table 2, and also Fig. 11 and Fig. 12, it is evident that the optical properties of the as-deposited *a*-As_2S_3 film prepared by magnetron sputtering were closer to its equilibrium state than those prepared by resistive thermal evaporation and pulsed-laser deposition. Fig. 13 shows how closely the calculated reflectance, which was regenerated using the optical properties and thickness obtained from the spectrometer, resembles the measured reflectance of our sputtered film.

According to the literature, when as-deposited thin films of *a*-As_2S_3 were exposed to visible light of wavelengths longer than 428 nm, the molecular structure of the thin film was modified via photodarkening in such a way that it had the same X-ray Diffraction (XRD) spectra as that produced by thermal annealing [56]. Since it has been shown that at pressure lower than 10 mTorr, the Ar spectrum in the chamber has no UV (200–400 nm) spectral lines and only contains wavelengths that are longer than 400 nm, it is therefore possible to photo-anneal or photo-polymerize an *a*-As_2S_3 film by sputtering it at a low pressure [57]. These attributes are unique to a magnetron sputtered *a*-As_2S_3 film and in our opinion cannot be easily achieved with other methods of deposition. This includes conventional non-magnetron RF sputtering, especially if very low RF power is required in the run to prevent excessive heat from cracking the 2-inch As_2S_3 target during the process.

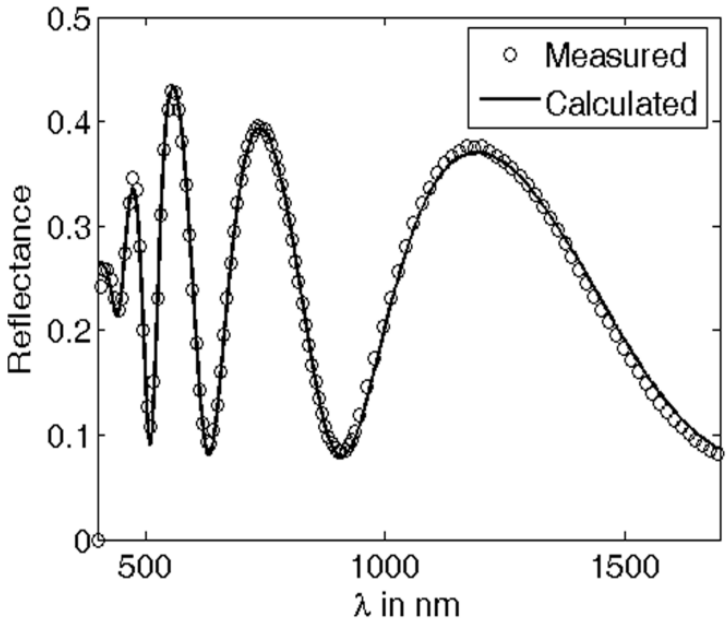

Fig. 13. The reflectance spectroscopy of an *a*-As_2S_3 film. The measured and calculated reflectance of a magnetron RF-sputtered *a*-As_2S_3 film on a glass substrate (Fisher Scientific cat. #12-550-A3). The thickness of the film was 377 ± 20 nm and the goodness of fit was 0.993 with 1.0 being the maximum value. The measured result obtained in this figure was from a spectrometer with an extended measuring range from 400 – 1700 nm (F20EXR, Filmetrics, Inc., San Diego, CA 921123).

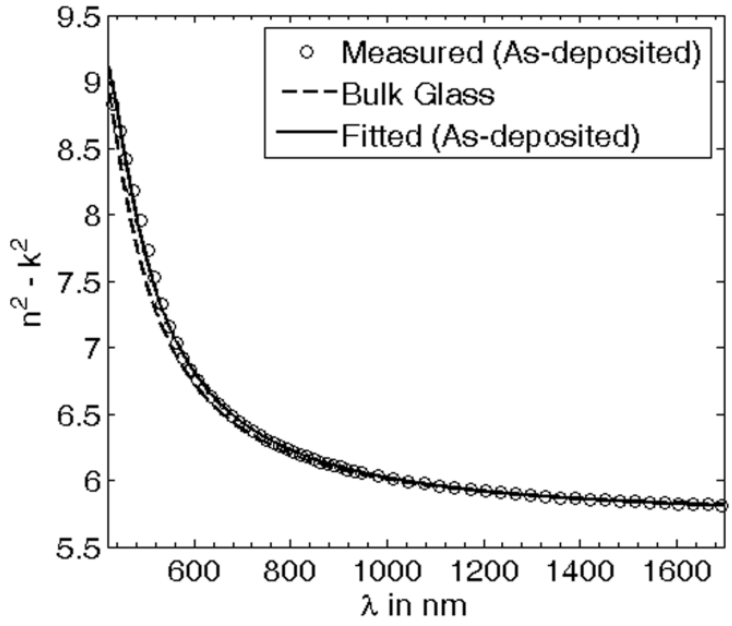

Fig. 14. . The dielectric constants of a magnetron sputtered *a*-As_2S_3 film. The real part of the dielectric constants, $\varepsilon_1 = n^2 - \kappa^2$, of a magnetron sputtered *a*-As_2S_3 thin film (as-deposited) and a bulk As_2S_3 taken from the reference [16]. The fitted values were derived from Drude model using measured data obtained from the spectrometer. The thickness of the film was 377 ± 20 nm and goodness of fit was 0.996.

The parameters, A_d, n_0, F_1, F_2, λ_1, and λ_2, shown in Table 3 are the terms used in the fitting of the real part of the dielectric constant of magnetron sputtered *a*-As_2S_3 thin film to the Drude model,

$$n^2 - \kappa^2 = n_0^2 + A_d \sum_{j=1}^{2} \frac{f_j(\lambda_j^{-2} - \lambda^{-2})}{(\lambda_j^{-2} - \lambda^{-2})^2 + \gamma_j \lambda^{-2}} \tag{19}$$

where $\gamma_1 = 4.194 \times 10^6$ and $\gamma_2 = 2.997 \times 10^{11}$. It also shows the average fitting parameters, A_k, b and λ_k, of the model used in the extrapolation of the measured

extinction coefficient κ, where $\kappa = A_k \times [1.0 + (\lambda/\lambda_k)^b]^{-1}$, and the parameters, A_n and λ_n, of the Sellmeier model, $n^2 = 1 + A_n\lambda^2/(\lambda^2 - \lambda_n^2)$, that was fitted to the measured refractive index. Fig. 14 shows how the real part of the dielectric constant, ε_1, of the as-deposited magnetron sputtered *a*-As_2S_3 thin film compared with the published results for a bulk material [16].

Table 3. The fitting parameters of the optical properties of *a*-As_2S_3 film. The average fitting parameters of the various models used in extending the optical properties of a magnetron sputtered *a*-As_2S_3 thin film (thermally annealed) beyond the measured wavelength. A_d, n_0, F_1, F_2, λ_1, and λ_2, belongs to the Drude model used in fitting the dielectric constant (real part), A_k, b and λ_k, are used for extending the extinction coefficient and A_n and λ_n, are used in the Sellmeier model for describing the dispersion of refractive index. G.O.F. refers to goodness of fit with a maximum value of 1.0.

A_n	λ_n (nm)	G.O.F.	A_k	b	λ_n (nm)	G.O.F.
4.640	284.2	0.988	0.482	19.39	429.0	0.998
A_d ($\times 10^{14}$)	F_1	F_2	n_0	λ_1 (μm)	λ_2 (nm)	G.O.F.
0.398	0.000	0.405	1.887	25.96	368.7	0.997

The XPS spectrum in Fig. 15 shows the binding energy of the electrons inside the 3d shell of the arsenic atom (As-3d) in the magnetron sputtered *a*-As_2S_3 film (as-deposited) and the As_2S_3 sputter target. The film's thickness is 303 ± 20 nm with a non-uniformity

of 6 nm and the refractive index at λ = 640 nm is 2.580. From the diagram, it can be seen that the binding energy of the arsenic atom (3d shell) is 43.2 eV. This value is not only near to the As_2S_3 sputter target at 43.3 eV, but also agrees with what was reported for a uncontaminated thermally evaporated *a*-As_2S_3 film [58]. The binding energy of the arsenic atom (3d shell) in an As_2S_3 film with photo-decomposition at the surface will be greater than 43.9 eV.

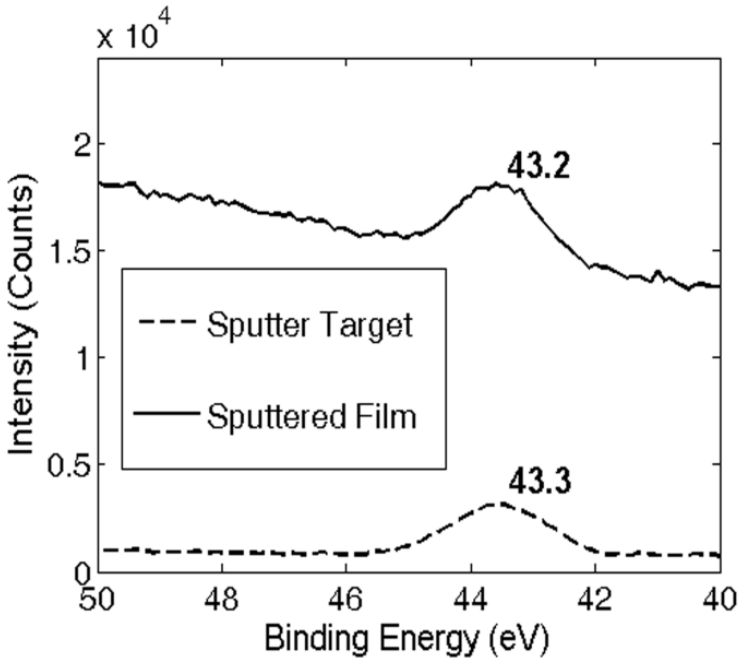

Fig. 15. The XPS spectrum of *a*-As_2S_3 film. No significant amount As_2O_3 was detected on the sputtered film. The thickness of the film was 303 ± 20 nm. The figure above shows the measured XPS spectrum of the As (3d shell) atom in the As_2S_3 sputter target and the as-deposited magnetron sputtered *a*-As_2S_3 film. No significant amount As_2O_3 was detected on the sputtered film. The thickness of the film was 303 ± 20 nm.

Quantitative analysis of the elements at the surface is derived from the peak areas of the XPS multiplex after background subtraction using standard CASA XPS processing software [59]. The atomic concentration calculated from the survey scan of the sputtered film shows that it contains 38.3% of arsenics and 61.7% of sulfur, which is close to the values obtained for the As_2S_3 sputter target (5 mm thick) at 40.6% of arsenics and 59.4% of sulfur. Since the measurement accuracy depends on several parameters, some of which can be difficult to account for, such as surface volume homogeneity and degree of sample degradation due to analysis, a more meaningful indication of measurement error would be to compare the results obtained from our As_2S_3 sputter target to the typical value (i.e. 39.1% of arsenics and 60.9% of sulfur) specified by the manufacturer in its MSDS data sheet. Based on this calculation, the measurement error worked out to be 4%. In other words, our sputtered film contains 38.3 ± 1.5 % of arsenics and 61.7 ± 1.5 % of sulfur, which is close to the desired stoichiometric of an As_2S_3. From the XPS spectrum, we can also see that there is no signal around 44.4 eV that would indicate the presence of any photo-induced As_2O_3 crystals on our as-deposited film [58, 60]. The test was conducted on a 4 days old film that was kept in ambient condition. No special coating or arrangement was applied to prevent oxidation. The micrograph shown in Fig. 16 was taken at × 1000 magnification by an optical microscope fitted with a polarizer. The picture shows a magnetron sputtered *a*-As_2S_3 film on top of a 7.0 μm straight Ti-diffused $LiNbO_3$ waveguide with no visible sign of any photo-induced crystals on the surface.

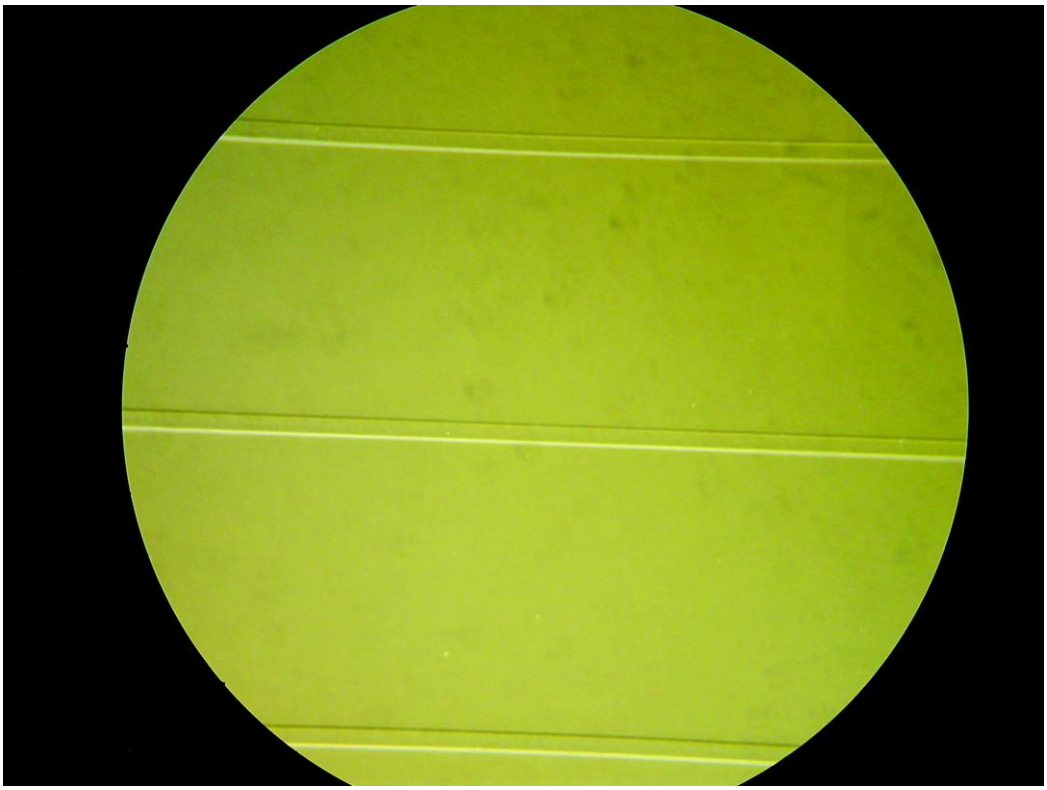

Fig. 16. A micrograph of an *a*-As_2S_3 film on top of some Ti:$LiNbO_3$ waveguides. The picture shows a magnetron sputtered *a*-As_2S_3 film on top of some Ti:$LiNbO_3$ waveguides taken by an optical microscope with a polarizer at × 1000 magnification. The film looks smooth with no visible signs of any photo-induced As_2O_3 crystals on the surface. The straight Ti:$LiNbO_3$ waveguide was 7 μm wide and measured thickness of the *a*-As_2S_3 film was 310 ± 20 nm.

3.3 Hybrid Integration of a Straight As_2S_3 Waveguide on $LiNbO_3$ Substrate

With the high-quality magnetron sputtered *a*-As_2S_3 thin films, we are now able to demonstrate some passive As_2S_3 waveguides designed for integrated optics on $LiNbO_3$ substrate. The vertically integrated *a*-As_2S_3 waveguides were made using standard semiconductor fabrication techniques. It begins with making the Ti:$LiNbO_3$ waveguide underneath the *a*-As_2S_3. First of all, a titanium thickness of 60 or 90 nm ± 5 nm was

sputtered on a diced y-cut x-propagating $LiNbO_3$ chip. The pattern was then formed by photolithography and etched onto the substrate using a reactive ion etching machine. After etching, the sample was put into a furnace and diffused for 5-6 hours at 1025°C in wet breathing air ambient. The end facets of the waveguide chip are then polished to optical quality. A 290 ± 20 nm thick *a*-As_2S_3 film was then magnetron sputtered onto the Ti:$LiNbO_3$ waveguide and a 200 ± 20 nm layer of spin-on-glass (Futurrex Inc., Franklin, NJ 07416) was covered on the *a*-As_2S_3 as a cladding. Contact photolithography was again used to define the pattern and a subsequent reactive-ion etching step forms the *a*-As_2S_3 waveguides. The resulting structure is illustrated in Fig. 17.

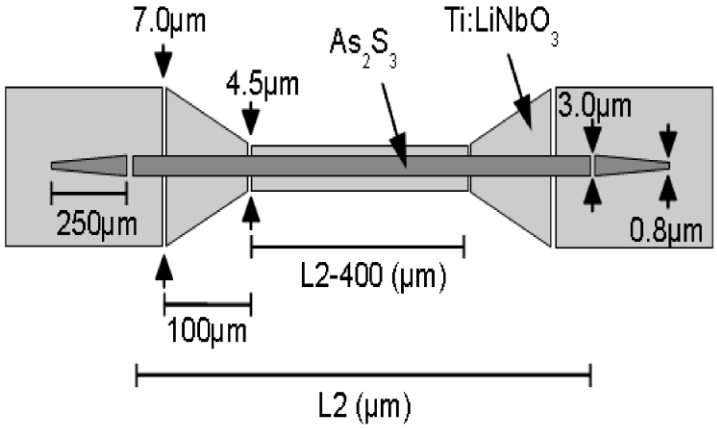

Fig. 17. The schematic diagram of a hybrid As_2S_3 straight waveguide. The picture shows a straight 3.0 μm wide As_2S_3 waveguide with propagation distance, L2 = 0.5, 1.0, 1.5, or 2.0 cm, fabricated on a 4.5 μm wide Ti:$LiNbO_3$ waveguide. This is an illustration of the waveguide structure used in the measurement of the propagation loss of a photo-annealed *a*-As_2S_3 waveguide deposited by magnetron sputtering.

The sample was tested by butt coupling light into the waveguide ends using a single-mode fiber. The laser source launched into the waveguides is a highly coherent laser that sweeps the wavelength from 1490 to 1570 nm. The mode of propagation was determined from a polarizer and the transmission loss was obtained from an Optical Vector Analyzer (OVA CTe, LUNA Tech., Roanoke, VA 24016). The propagation and the coupling losses were calculated from the insertion losses of several 3 μm wide hybrid As_2S_3 waveguides. The schematic diagram in Fig. 17 shows how these waveguides were vertically integrated with a 4.5 μm wide Ti:$LiNbO_3$ waveguide. The design allows us to couple optical signal in a relatively simple and low loss manner from a single mode fiber into our integrated optics.

3.3.1 Results and Discussion

Since the coupling of the TE propagation from the Ti:$LiNbO_3$ waveguide into the As_2S_3 waveguide suffers from various problems caused by the out-diffusion of Li ions during the diffusion process of the Ti:$LiNbO_3$ waveguide, we have designed our devices to work with only TM propagation [61-63]. In this way, we eliminate the additional fabrication steps that have to be taken to prevent the formation of a unwanted planar waveguide that will interfere with the coupling of the TE propagation mode from the Ti:$LiNbO_3$ channel waveguide. Fig. 18 displays the insertion losses of TM propagation at various wavelengths in the 4.5 μm Ti:$LiNbO_3$ waveguide with and without the vertical

integration of the 3.0 μm *a*-As_2S_3 waveguide. The Ti:$LiNbO_3$ waveguide had an initial thickness of 60 nm and has been diffused for 6 hours. The experimental result shows that the magnetron sputtered *a*-As_2S_3 waveguide was able to improve the TM propagation in the 4.5 μm wide by 20 mm long Ti:$LiNbO_3$ by at least 12 dB.

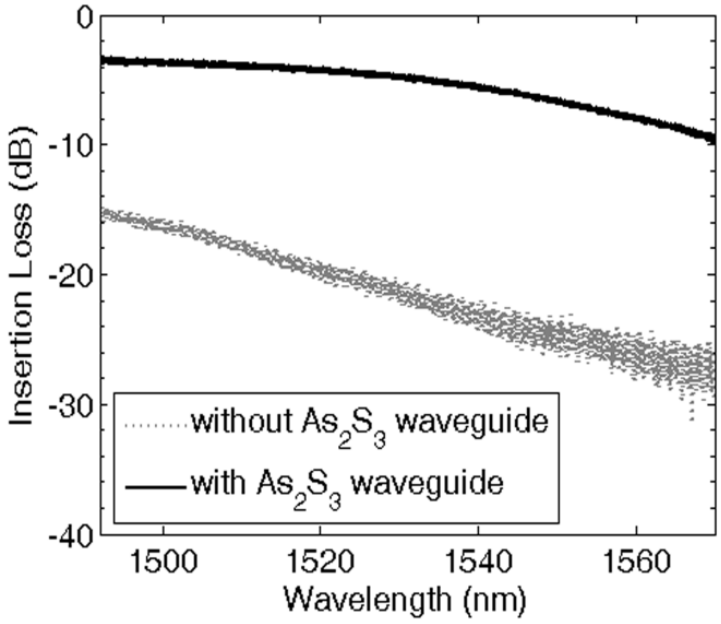

Fig. 18. The insertion loss of an *a*-As_2S_3 waveguide. The figure shows the measured TM insertion loss of a 4.5 μm Ti:$LiNbO_3$ optical waveguide (Ti thickness = 60 ± 5 nm and diffusion hours = 6 hours) with and without the vertical integration of the straight 3.0 μm wide *a*-As_2S_3 waveguide prepared by magnetron sputtering. The measurement error was ± 0.1 dB.

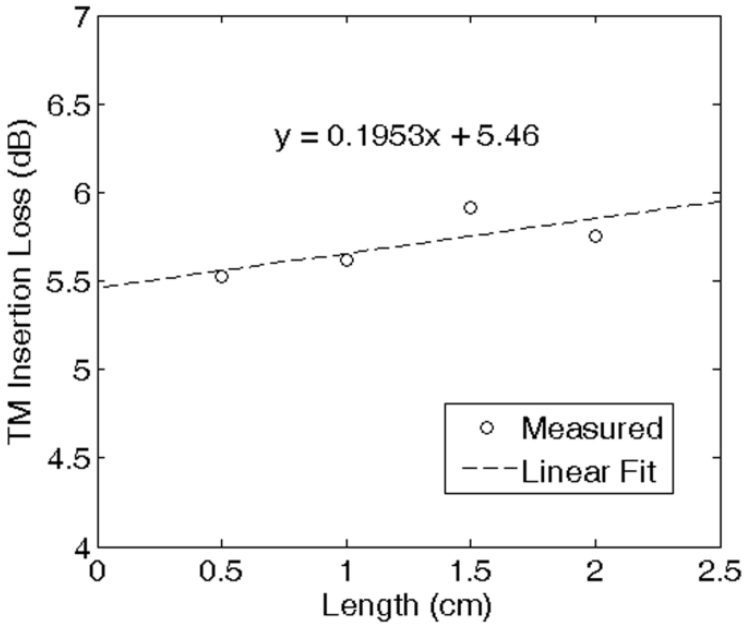

Fig. 19. The propagation loss of a hybrid *a*-As_2S_3 waveguide. The TM propagation loss of a magnetron sputtered *a*-As_2S_3 film at λ = 1.5 μm on a 4.5 μm Ti:$LiNbO_3$ (Ti thickness = 90 ± 5 nm and diffusion hours = 5 hours). The as-deposited *a*-As_2S_3 film was 290 ± 20 nm thick and its width was 3.0 μm. The *a*-As_2S_3 waveguides were 0.5, 1.0, 1.5, and 2.0 cm long, with a 200 ± 20 nm layer of spin-on-glass as an over-cladding. The measurement error of the insertion loss was ± 0.1 dB.

The Fig. 19 displays the insertion loss, ± 0.1 dB, of the hybrid *a*-As_2S_3 waveguides for different propagation lengths at λ = 1.5 μm. The straight line in the figure represents the best linear fit to the insertion losses and it gave us the propagation loss and the coupling loss of the *a*-As_2S_3 waveguide on Ti:$LiNbO_3$. The propagation and coupling losses, which includes fiber-to-waveguide coupling loss, calculated for a TM propagation mode at λ = 1.5 μm for a 3.0 μm as-deposited hybrid *a*-As_2S_3 waveguide on a 4.5 μm

Ti:$LiNbO_3$, (i.e. As_2S_3-on-Ti:$LiNbO_3$ waveguide) was 0.20 ± 0.05 dB/cm and 2.75 ± 0.05 dB/coupler respectively.

We have measured the optical properties of *a*-As_2S_3 thin films and the propagation loss of a hybrid *a*-As_2S_3 straight waveguide on Ti:$LiNbO_3$ deposited by magnetron sputtering. While the average E_{op} of an as-deposited film remains relatively unchanged at 2.35 ± 0.04 eV when annealed, its refractive index n at λ = 1530 nm increased slightly from 2.42 to 2.43. The stoichiometry was correct and the binding energy of the As3d of the film was 43.2eV with no significant amount of As_2O_3 crystals found on the surface. The optical and structural properties agree with published results on As_2S_3 bulk glass and our as-deposited films are closer to the equilibrium state than *a*-As_2S_3 films made by thermal evaporation and PLD. These attributes are unique to a magnetron sputtered *a*-As_2S_3 film and we attribute it to the photo-annealing effect caused by the visible light emitted by the argon plasma during the sputtering process. The TM propagation loss at λ = 1.5 μm of a 3.0 μm as-deposited hybrid *a*-As_2S_3 waveguide on a 4.5 μm Ti:$LiNbO_3$ was 0.20 ± 0.05 dB/cm.

This result compares favorably with a recent paper on the losses of an As_2S_3 waveguide prepared by thermal evaporation with sub-micrometer thickness [64]. From the reference, we realized that the same process used in the fabrication of a record low-loss As_2S_3 ridge waveguide (0.05 dB/cm), is now producing a waveguide with a loss of 0.2 dB/cm. Apparently, scattering losses from surface roughness can no longer be ignored

when the thickness of the waveguide is in the sub-micrometer range. The thickness of the As_2S_3 waveguide reported in the reference is 0.83 μm. This thickness is greater than the typical As_2S_3 thickness (~ 0.46 μm) used in the hybrid waveguides demonstrated here using magnetron sputtering.

3.4 Hybrid Integration of an As_2S_3 Mach-Zehnder Interferometer

A Mach-Zehnder interferometer (MZI) is a device that is used to determine the relative phase shift between two collimated beams from a coherent light source. It is a very versatile component and plays an essential role in any integrated photonics circuits as they are often made into more advance optical devices like multiplexer or high speed modulator [3, 4].

Other than method used in the previous section (i.e. vertically coupling), As_2S_3 waveguides can also be integrated with Ti:$LiNbO_3$ by side coupling. In this section, we will demonstrate a hybrid integration of an As_2S_3 S-Bends with a straight Ti:$LiNbO_3$ waveguide by side coupling. The combined structure is a hybrid As_2S_3 Mach-Zehnder interferometer. An As_2S_3 MZI integrated with a Ti:$LiNbO_3$ waveguide offers the ability for electrical tuning of the frequency response by making use of the inherent electro-optic effect of the $LiNbO_3$. This will further reduce the size of a $LiNbO_3$ based modulator currently in used in the industry. In order to avoid the changes in physical properties caused by physical aging, the hybrid MZI was thermally annealed and photo-exposed to completely saturate the aging process.

3.4.1 Experimental Techniques

Titanium diffused lithium niobate (Ti:$LiNbO_3$) waveguide was fabricated with a titanium thickness of 95 nm ± 5 nm on a 20-by-23 mm y-cut x-propagating $LiNbO_3$ chip. The chip was diffused for 9.5 hours at 1025 °C in wet breathing air ambient. The side coupled MZI, with an As_2S_3 thickness = 460 ± 20 nm, was integrated to the Ti:$LiNbO_3$ waveguides using standard semiconductor fabrication techniques. The sputtering of As_2S_3 was done at a 1.5 mTorr with the argon flowing at 35 sccm and a RF power of 35W in an automated magnetron sputtering system (ATC 2200 IBAD, AJA Intl, Inc., Scituate, MA 02066). Thermal annealing was conducted in the dark in a vacuum oven at 130 °C for 27 hours. The photo-induced experiment was carried out on a well annealed film by a mercury vapor lamp (λ_c = 365.4 nm) at 2.5 mW/cm^2 for 120 sec. The sample was then allowed to age in the dark for 6 days at room temperature and atmospheric pressure. The integrated hybrid MZI was tested with single-mode fiber by butt coupling method. The Jones matrix that represents the frequency response of the MZI is taken from the optical vector analyzer, (OVA CTe, LUNA Tech., Roanoke, VA 24016). Fig. 20 shows the schematic drawing of a hybrid As_2S_3 MZI integrated with a Ti:$LiNbO_3$ waveguide. The width of the Ti:$LiNbO_3$ waveguide is 7 μm, the As_2S_3 waveguide is 3.5 μm, and the 2-stage As_2S_3 taper vary from 1-to-1.6 μm and then 1.6-to-3.5 μm. The As_2S_3 waveguide is designed to couple only the TM propagation mode in the Ti:$LiNbO_3$ waveguide. Three integrated MZIs with different spacing between the two S-Bends were fabricated. The spacing was 2750 μm, 5500 μm, and 11000 μm.

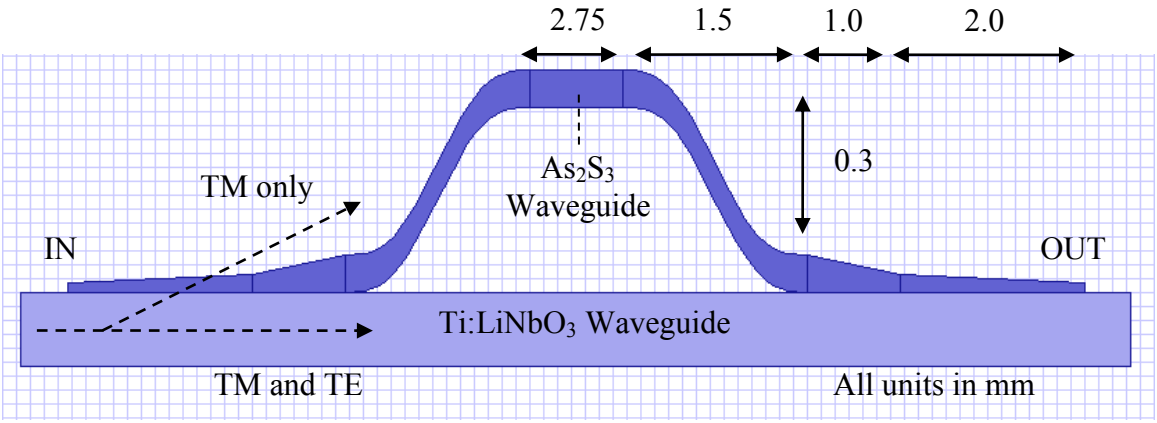

Fig. 20. The schematic drawing of a hybrid As_2S_3 MZI. A set of As_2S_3 S-Bend and reversed S-Bend is integrated with a straight Ti:$LiNbO_3$ to create a MZI. The width of the Ti:$LiNbO_3$ waveguide is 7 μm, the As_2S_3 waveguide is 3.5 μm, and the 2-stage As_2S_3 taper vary from 1-to-1.6 μm and then 1.6-to-3.5 μm. The arc length of the S-Bend is 1536.353 μm. TM refers to transverse magnetic propagation mode and TE refers to transverse electric mode. Three integrated MZIs with different spacing between the two S-Bends were fabricated. The spacing was 2750 μm, 5500 μm, and 11000 μm.

3.4.2 Results and Discussion

The Fig. 21 shows the frequency responses of three well annealed hybrid As_2S_3 MZIs. Basically it resembles a typical interferometric response, i.e. constructive and destructive interferences, one get from mixing two coherent lights together. In this case, the TM signal that travel through the As_2S_3 waveguide arrives at the output and recombined with the TM signal that travels through the Ti:$LiNbO_3$ waveguide. From the free spectral

range (FSR) of their frequency responses, which is defined as the spacing in optical frequency or wavelength between two successive optical intensity maxima or minima of an interferometer, the average group index of the three integrated As_2S_3 waveguide was calculated to be 2.36 ± 0.01. This average value represents the group index of the complete signal path through the As_2S_3 structure, which includes not only the 3.5 μm straight waveguide and the S-bends but also the 2-stage tapers. The 2-stage taper is specially designed to have a taper width that is linearly increasing at two different rates. The index was calculated from the definition of free spectral range derived for our interferometer, FSR = λ^2 / ($n_A \times d_A - n_T \times d_T$), where λ is the central wavelength of the nearest transmission peak, n_A and d_A are the group index and signal path length of the As_2S_3, and n_T and d_T are the group index and signal path length of the Ti:$LiNbO_3$ waveguide for a TM mode. The group index of the Ti:$LiNbO_3$ waveguide is obtained from the design tool, FIMMWAVE, and is 2.27 ± 0.01.

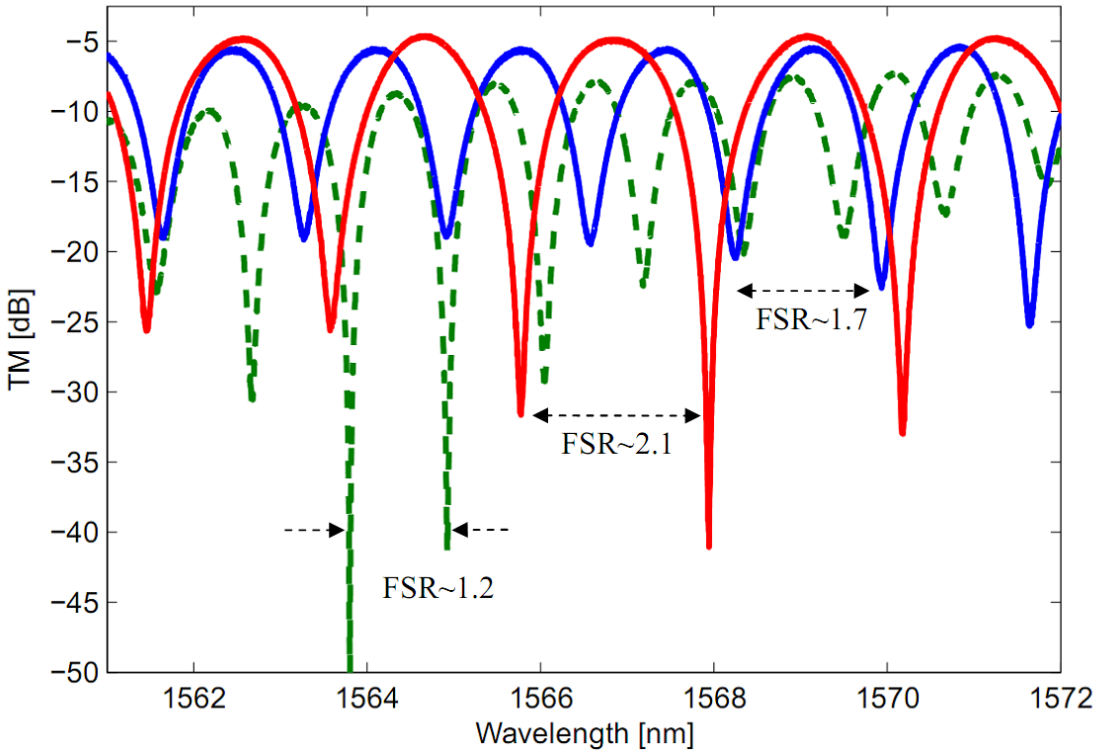

Fig. 21. Frequency response of thermally annealed hybrid MZI. The "red" line is from an annealed MZI shown in Fig. 20. The MZI represented by the "blue" line is similar to the one in Fig. 20 except that its Ti and As_2S_3 optical path length is longer by 2750 µm. The MZI represented by the "green" dash line is also similar to the one in Fig. 20 except that its Ti and As_2S_3 optical path length is longer by 8250 µm.

The impulse response of the hybrid MZI can be obtained from performing an inverse Fourier transform of the measured frequency response. The difference in the group delay, τ_g, of the TM pulse travelling in the Ti:$LiNbO_3$ waveguide and the one propagating in the As_2S_3 waveguide can be expressed as, $\Delta\tau_g = (n_A \times d_A - n_T \times d_T) / c$, where c is the speed of light in vacuum, n_A and d_A are the group index and signal path length of the As_2S_3, and n_T and d_T are the group index and signal path length of the Ti:$LiNbO_3$ waveguide for a TM mode. The group index calculated from the average group delay of a well annealed hybrid As_2S_3 MZI as shown in Fig. 20 is $n_g = 2.353$. This is close to the average group index extracted from the frequency response. Fig. 22 compares the frequency response of the well annealed hybrid interferometer to the frequency response taken six days after the exposure. It shows the FSR increases from 2.1 ± 0.1 nm (“red” dash line) to 2.5 ± 0.1 nm (“blue” solid line). The average group index of the exposed integrated As_2S_3 waveguide is 2.35 ± 0.01.

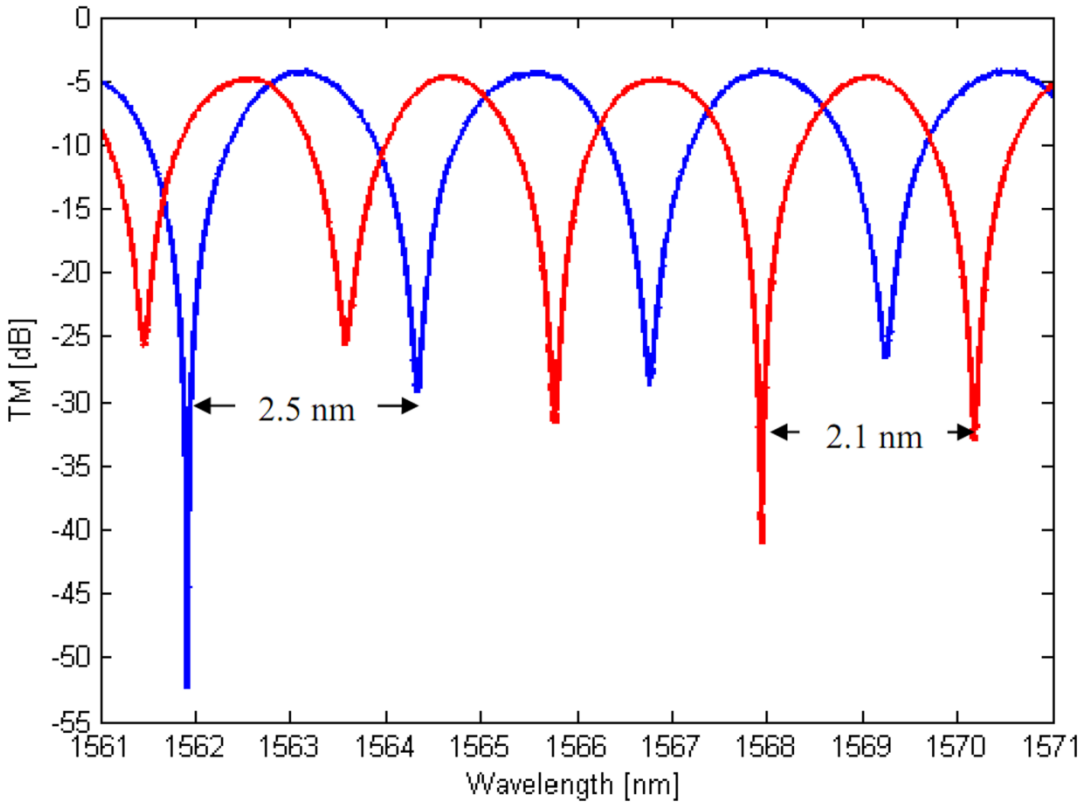

Fig. 22. Photo-induced phenomenon of an As_2S_3 hybrid MZI. The "red" line is from an annealed MZI shown in Fig. 20 and the "blue" line is the frequency response taken 6 days after the exposure.

Fig. 23 shows the transfer function of the thermally annealed hybrid MZI shown in Fig. 20 taken 6 months after the last exposure. It shows the frequency response of the TM propagating mode in the hybrid MZI, and also the cross polarization terms represented by TMin-TEout terms in the figure. In other words, if the MZI is represented by a four-port network, then the term TMin-TEout is the signal detected at the TE mode output of the MZI for a TM mode input. The relatively low magnitude of the cross polarization

terms indicates no significant amount of cross polarizations in our hybrid MZI. This result is important as unintended polarization conversion which distorts the output can sometime happened at the coupling regions, both at the tapers and at the fiber to waveguide regions. The FSR measured at around λ = 1566 nm is 2.2 ± 0.1 nm. This is closed to the FSR of the annealed state, FSR = 2.1 ± 0.1 nm, 6 months before the exposure.

We have successfully demonstrated the feasibility of integrating an As_2S_3 Mach-Zehnder interferometer on a Ti:$LiNbO_3$ waveguide with magnetron sputtering. The impulse response confirms the splitting of the TM propagation mode into two pulses, one travelling in the Ti:$LiNbO_3$ and the other in the As_2S_3 waveguides. The photo-induced change in the average group index of the integrated As_2S_3 waveguide is -0.4% and is lower than the photo-induced change experienced by an As_2S_3 ring resonator prepared by thermal evaporation [65].

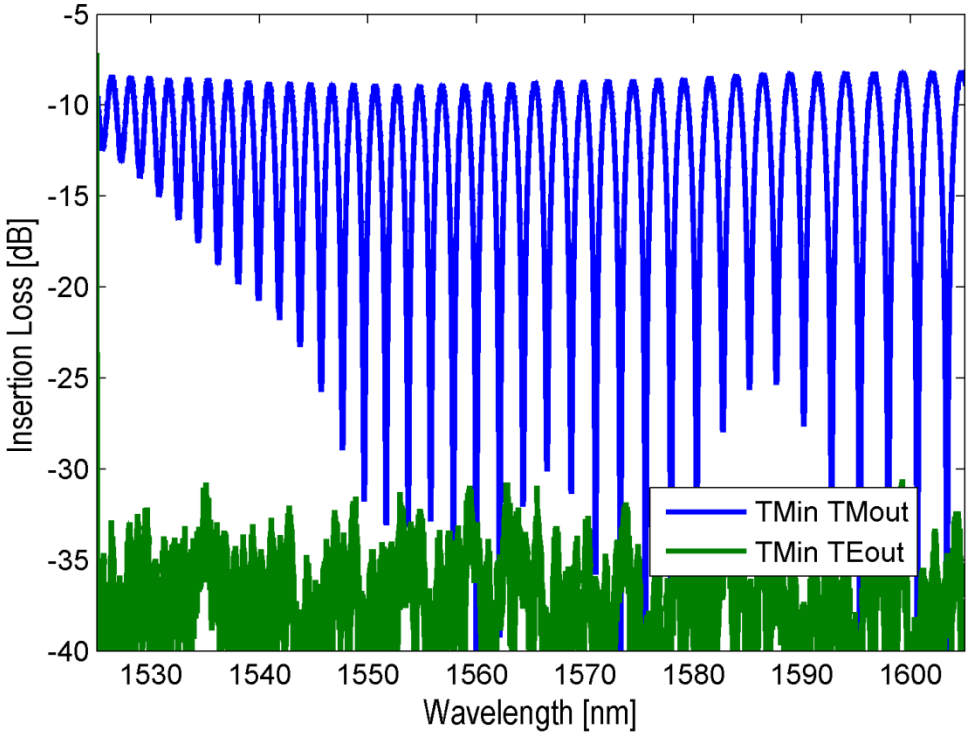

Fig. 23. The transfer function of an integrated As_2S_3 MZI. The result was taken from a thermally annealed MZI taken 6 months after the exposure. It shows the frequency response of the TM propagating mode in the hybrid MZI.

4. ERBIUM-DOPED LITHIUM NIOBATE WAVEGUIDE AMPLIFIER

4.1 Background

Erbium is a chemical element in the lanthanide series, with the symbol Er and atomic number 68. A silvery-white solid metal when artificially isolated, natural erbium is always found in chemical combination with other elements on Earth. This lanthanide series begins with the element lanthanum (Z = 57) and ends with the elements lutetium (Z = 71). The elements of this series are generally found in the +3 oxidation state and the 4f shell can accommodate a total of 14 electrons in total. The Er^{3+} ion contains 11 electrons in its 4f shell and the ground state has the term $^4I_{15/2}$. The electrons from this ground state can be promoted to any one of the higher energy states through the absorption of a photon of sufficient energy. The trivalent erbium ion, Er^{3+}, exhibits a strong emission band that is situated around 1535 nm wavelength from the emission of a photon due to the transition of an electron from the $^4I_{13/2}$ meta-stable state to the $^4I_{15/2}$ ground state. The $^4I_{13/2}$ is the meta-stable state that exhibits long luminescent lifetimes enabling this atom to sustain population inversion.

Since the Er^{3+} ion can sustain population inversion at telecommunication frequencies, it has been heavily employed for use in devices that operate in the popular “C”-band (1530 nm to 1565 nm wavelength) and “L”-band (1565 to 1625 nm wavelength) of the optical telecommunications spectrum. One of the most important uses of Er^{3+} is its inclusion into silica to form the erbium doped fiber amplifier (EDFA). The EDFA is particularly

attractive because it allows the amplification of an optical signal without the need to first take the optical signal out of the fiber and converting it into an electrical signal before the amplification step, thus enabling a dramatic simplification in the equipment that is used. Secondly, because Er^{3+} ions display photoluminescence covering both the C- and L- bands, it is well suited for a high-capacity wavelength-division-multiplexed system.

In this section, we will demonstrate the fabrication and characterization of erbium-doped optical waveguide amplifiers (EDWA) in x-cut y-propagating lithium niobate ($LiNbO_3$) by erbium (Er) and titanium (Ti) diffusion.

4.2 Experimental Technique

A 20-by-20 mm and 40-by-20 mm sample of commercially available x-cut y-propagating $LiNbO_3$ was cleaned and dehydrated. An erbium film of 19 ± 5 nm and 13 ± 5 nm were deposited respectively onto the 20-by-20 mm and 40-by-20 mm samples by magnetron sputtering from a 2-inch 99.9% pure erbium target (American Elements Inc., Los Angeles, CA 90024). The film thickness was estimated from a calibrated thickness monitor installed in the sputtering system. The run was carried out at 5.0 mTorr with a DC current of 100 mA and 8 sccm of argon. The Er samples were then placed in a furnace for thermal diffusion at 1100 °C for 120 hrs in a dry oxygen atmosphere at a flow rate of 150 sccm for the 20-by-20 mm sample and 103 sccm of argon for the 40-by-20 mm. Thereafter, a 80 ± 5 nm and 105 ± 5 nm layer of Ti film were deposited respectively onto the 20-by-20 mm and 40-by-20 mm samples by magnetron sputtering a

2-inch 99.9% pure titanium target (American Elements Inc., Los Angeles, CA 90024). Various straight waveguides with a width of 7 and 11 μm were then photo-lithographically patterned over the Ti film. Optical channel waveguides were formed by thermal diffusion of the Ti stripes into the sample in a furnace at a temperature of 1025 °C for 9 to 11 hrs with breathing air at a flow rate of 150 sccm. Once the Ti is diffused into the Er-diffused samples, the edges of the samples were mechanically polished using diamond lapping microfilms and the sample tested for insertion loss. Fig. 24 illustrates the typical fabrication process for an Er-doped Ti-diffused LiNbO3 waveguide amplifier.

Over the past two decades, a number of papers have reported on various kinds of Er-doped waveguide amplifiers (EDWAs), which have the potential for application in optical fiber communication system. Many nomenclatures such as internal gain, net gain, signal enhancement, on–off gain, internal net gain, net internal gain, etc were proposed for the description of the amplification performance of the EDWA device. Among these nomenclatures, the internal gain, net gain, and signal enhancement are often cited in the literatures.

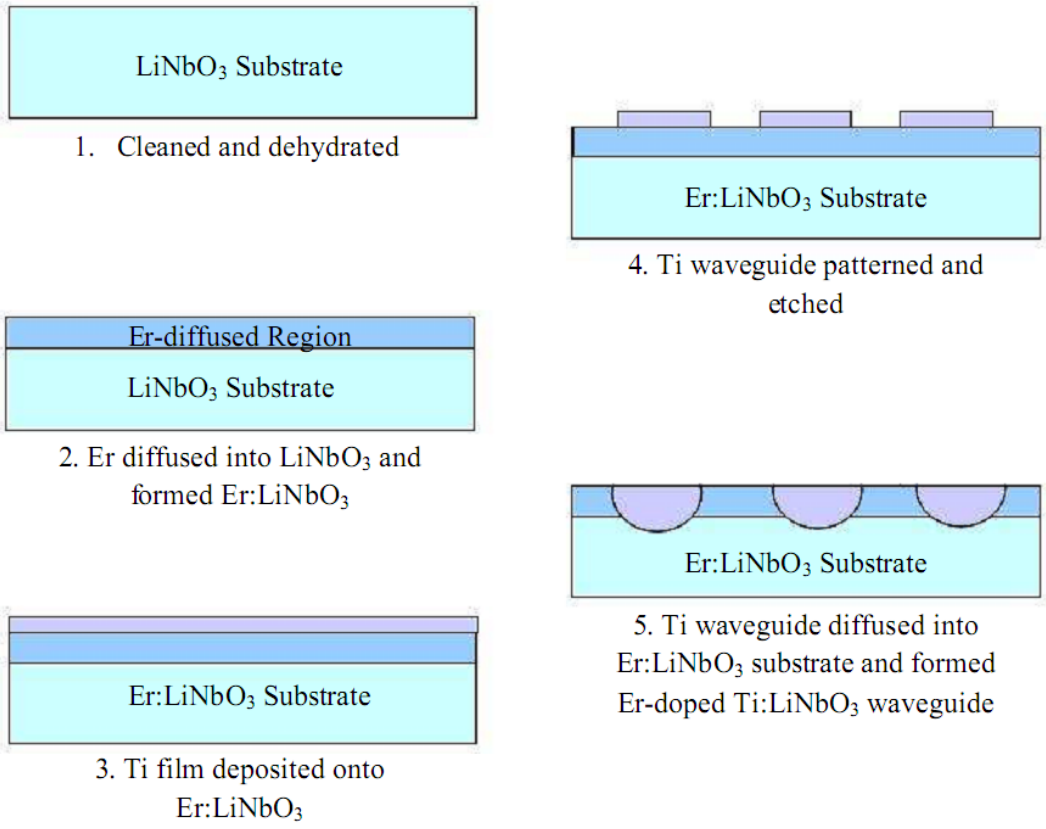

Fig. 24. The fabrication process for a Er:Ti:$LiNbO_3$ waveguide amplifier.

However, the definitions for these three physical quantities are rather confusing in the literature. We have decided to follow the definitions described in this reference [66]. The definition of each parameter will be described as follows using the measurement setup illustrated in Fig. 25.

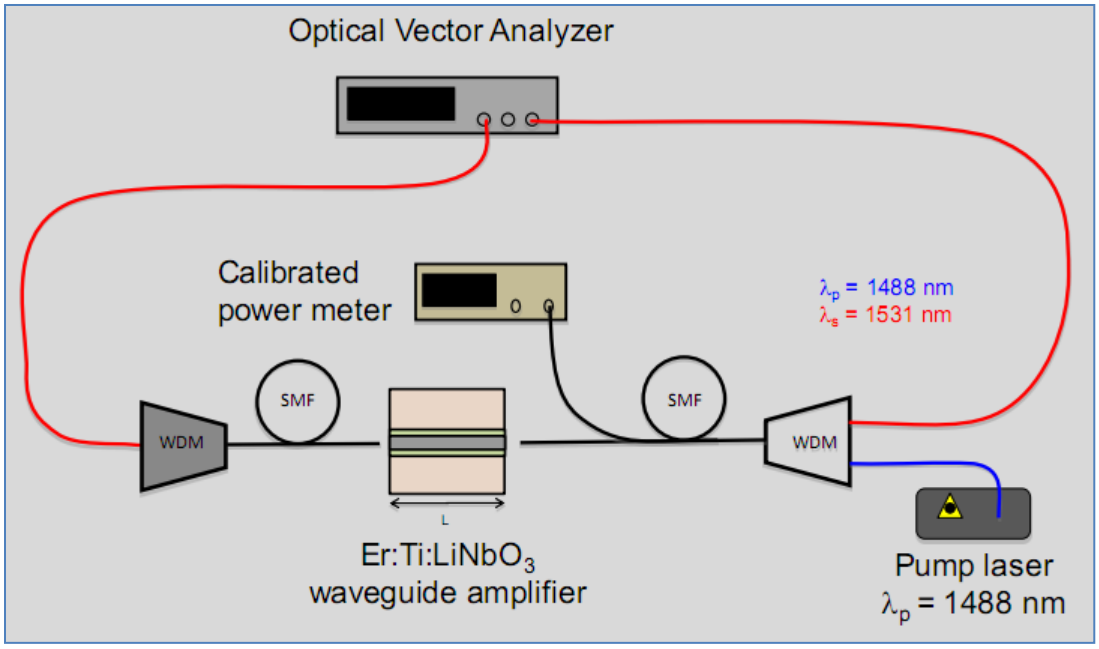

Fig. 25. Measurement setup for Er:Ti:$LiNbO_3$ waveguide amplifier. SMF refers to single mode optical fiber and WDM is wavelength division multiplexer.

Input signal from the optical vector analyzer (OVA) is multiplexed (via WDM) with the 1488 nm pump laser and then butt coupled into the Er:Ti:$LiNbO_3$ waveguide amplifier by a single mode optical fiber. The output signal from the amplifier is then routed through another WDM to filter out the pump signal before being sent back to the OVA. The optical power of the signal is read from the OVA and the input pump power to the Er:Ti:$LiNbO_3$ waveguide amplifier is measured by a calibrated power meter. The definition of the various performance parameters, such as net gain and internal gain, of an EDWA is described in the following ways.

With reference to Fig. 26, the net gain of the amplifier, which is defined as a fiber-to-fiber optical power ratio with the pump laser turned on, is expressed as,

$$\text{Net Gain} = 10\log_{10}\frac{P_s(L)}{P_s(0)} \tag{20}$$

and the internal gain of the amplifier, which is defined as the power ratio within the waveguide with the pump laser turned on, is described as follows,

$$\text{Internal Gain} = 10\log_{10}\frac{P_s(L)}{P_s(0)} + Loss_{\text{coupling}}^{\text{input}} + Loss_{\text{coupling}}^{\text{output}} \tag{21}$$

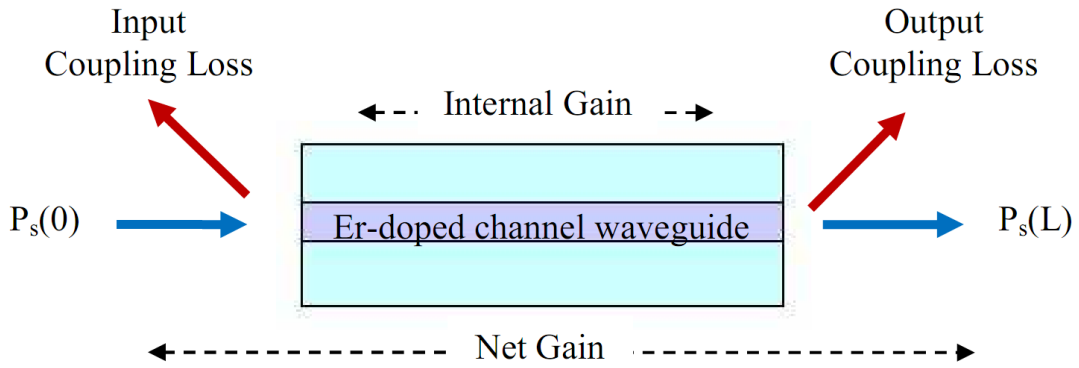

Fig. 26. The definition of net gain and internal gain of EDWA. The length of the amplifier is L. P_s refers to the optical power of the input signal.

4.3 Results and Discussion

The Fig. 27 shows the measured insertion gain or net gain of an 11 μm waveguide amplifier on the 20-by-20 mm sample. From the figure, we can see that the maximum net gain of the amplifier measured for a TM mode at 182mW of pump power is 2.29 ± 0.05 dB at around λ = 1532 nm. Since the input and output coupling losses of the 11 μm waveguide were estimated to be about 0.4 dB each, the internal gain of the amplifier worked out to be 3.1 ± 0.1 dB. The backward pump in the figure refers to the case when the pump signal is travelling in a direction opposite to the input signal. This is accomplished by connecting another pump laser to the WDM responsible for filtering out the pump signal. It is the WDM that is placed in between the output of the device under test and the OVA in Fig. 25. The backward pump laser is not shown in the measurement setup in Fig. 25.

In order to gauge the performances of our EDWA, we have to compare our results to the highest gain reported in the literature for an erbium doped $LiNbO_3$ amplifier [67, 68]. However, due to a different definition of net gain used by those groups, we have to define a new term in our measurement before we can compare our results.

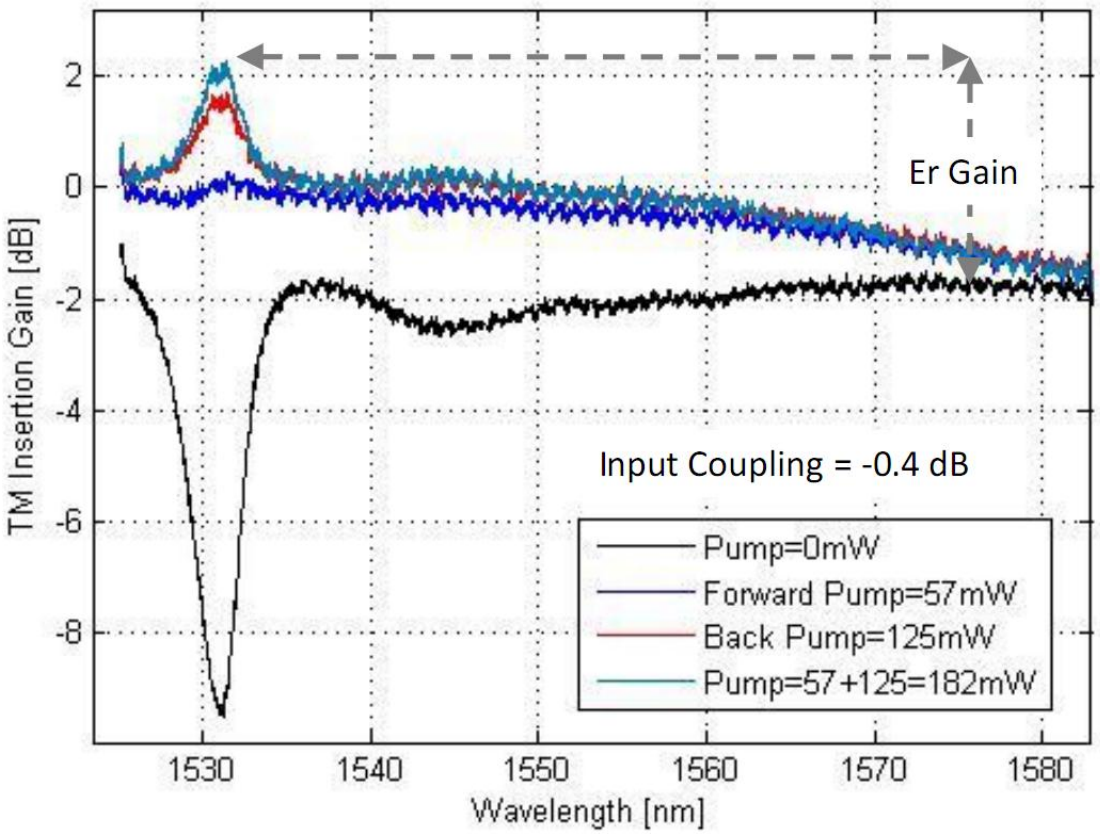

Fig. 27. Small-signal TM net gain of a 11 μm Er:Ti:$LiNbO_3$ waveguide amplifier. The backward pump refers to the case when the pump signal is travelling in a direction opposite to the input signal via the WDM responsible for filtering out the pump signal. The measured net gain at 182mW of pump power is 2.29 ± 0.05 dB around λ = 1532 nm.

In their definition, the net gain of the amplifier is measured with respect to another similar waveguide that is not doped with any erbium, i.e. comparing the insertion loss of a Er:Ti:$LiNbO_3$ waveguide to a Ti:$LiNbO_3$ waveguide. The "net gain" that they have used is different than our definition where 0 dB gain implies transparent transmission. In Fig. 27, we defined our Er gain as the power ratio of the maximum insertion gain at λ = 1532 nm to the insertion gain of the amplifier away from the absorption region, which in our case is λ = 1585 nm. In our opinion, this is equivalent to comparing the net gain of the Er:Ti:$LiNbO_3$ waveguide amplifier to an undoped Ti:$LiNbO_3$ waveguide as will be explained in the followings based on the measurement shown in Fig. 28.

The Fig. 28 shows the measured Er absorption for a TE propagation mode as a function of the length of a Er:Ti:$LiNbO_3$ amplifier fabricated by co-diffusion [69]. As we can see in the figure, at a wavelength, e.g. at λ = 1570 nm, away from the main absorption region of Er centered around λ = 1525 nm to 1555 nm, the absorption approaches zero. Since an undoped Ti-diffused waveguide is just like a Er:Ti:$LiNbO_3$ waveguide with zero absorption or "no erbium", the insertion loss of the Er:Ti:$LiNbO_3$ waveguide amplifier at this wavelength, i.e. at λ = 1570 nm, can be said to be equivalent to an undoped Ti-diffused $LiNbO_3$ waveguide.

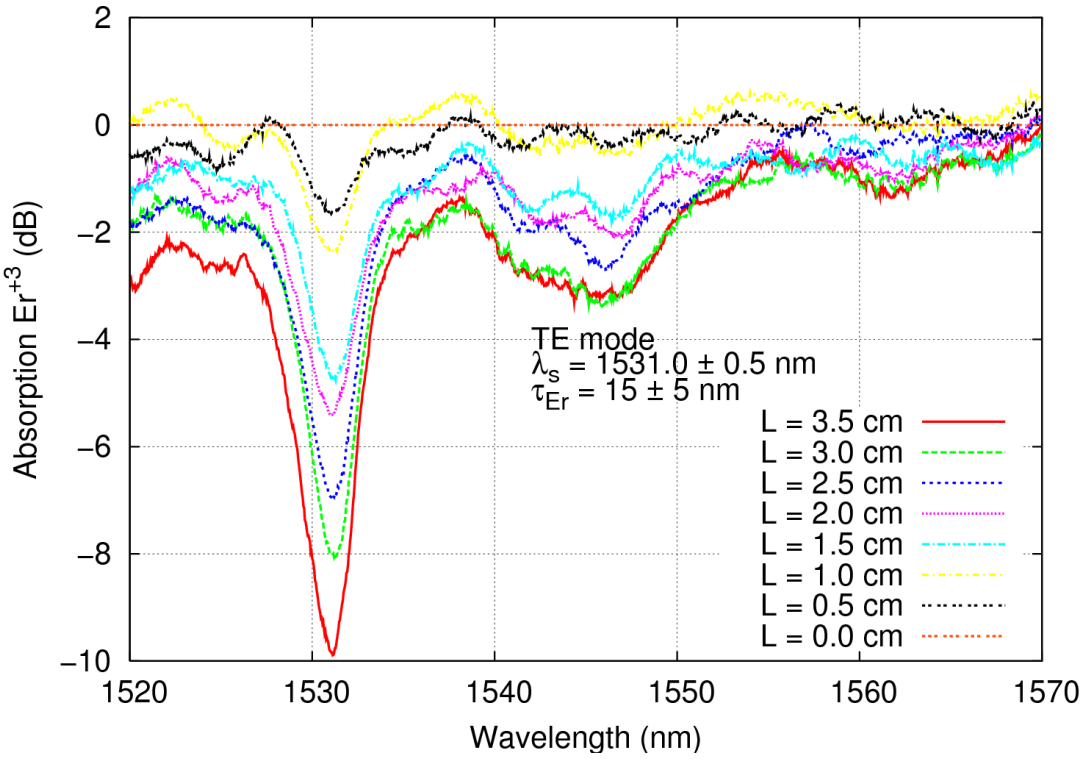

Fig. 28. The absorption spectra of Er:Ti:$LiNbO_3$ waveguide amplifier. The figures shows the measured Er absorption for a TE propagation mode as a function of the length of a Er:Ti:$LiNbO_3$ amplifier fabricated by co-diffusion [69]. τ_{Er} refers to the initial thickness of the erbium film before diffusion.

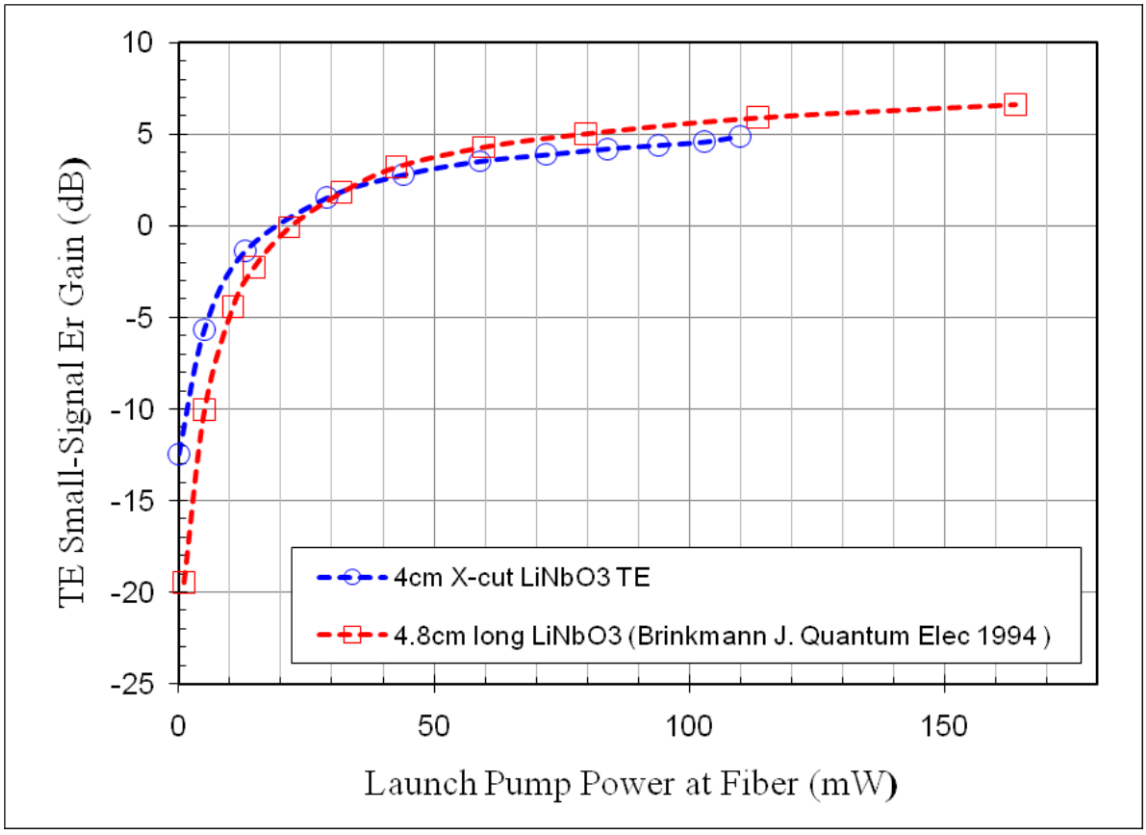

Fig. 29 The TE small-signal gain of Er-doped Ti:$LiNbO_3$ waveguide amplifiers. The open circle represents the results obtained by our group on a 4 cm long x-cut $LiNbO_3$ and the open square values were obtained from the results published in the literature for a 4.8 cm long z-cut $LiNbO_3$ [67]. The Er gain of our 4 cm long amplifier at 110mW is just 0.2 dB below the longer 4.8 cm amplifier.

Having established the same set of reference, we can now compare our results with those reported in the literatures. In Fig. 29, we have the TE small-signal gain of two Er-doped Ti:$LiNbO_3$ waveguide amplifiers. The open circle represents the results obtained by our group on a 40-by-20 mm Er:Ti:$LiNbO_3$ waveguide amplifier and the open square values were obtained from the reference for a 4.8 cm long Er:Ti:$LiNbO_3$ waveguide amplifier

[67]. Their initial Er and Ti thickness was respectively 13 nm and 95 nm. Both results were obtained from a 7 μm wide Er:Ti:$LiNbO_3$ waveguide. As we can see from the figure, the Er gain of our 40 mm long amplifier at 110mW is just 0.2 dB below the longer 48 mm EDWA.

Table 4. The incremental small-signal internal gain (Er gain) of Er-doped $LiNbO_3$ amplifier. Unlike Er:Ti:$LiNbO_3$, Ti:Er:$LiNbO_3$ refers to a Ti diffused Er-doped $LiNbO_3$ waveguide, i.e. erbium is introduced into the $LiNbO_3$ substrate not by diffusion but by mixing erbium powder in the melt during the making of the $LiNbO_3$ wafer.

Sample	Max. Er Gain Pump=180-200mW TE (dB/cm)
Kogahara (Z-cut Ti:Er:$LiNbO_3$) [68]	2.1
Texas A&M (X-Cut Er:Ti:$LiNbO_3$)	1.8 ± 0.1
Brinkmann (X-Cut Er:Ti:$LiNbO_3$) [67]	1.0
Brinkmann (Z-Cut Er:Ti:$LiNbO_3$) [67]	1.4

In Table 4, we have compared the amount of amplification per unit length measured for TE mode of our 40-by-20 mm Er:Ti:$LiNbO_3$ waveguide amplifier to those reported in the literature. From the table, we can see that the result we have obtained from our process is among the highest reported by others for an EDWA fabricated on $LiNbO_3$ substrate. Although the amplifier with the highest gain in the table is from a Z-cut

Ti:Er:$LiNbO_3$ waveguide amplifier, the fabrication of an Er-doped amplifier on $LiNbO_3$ in this way is not practical from the stand point of an integrated optics. This is because unlike our Er:Ti:$LiNbO_3$, the erbium in the Ti:Er:$LiNbO_3$ amplifier is introduced into the $LiNbO_3$ substrate not by diffusion but by mixing erbium powder in the melt during the making of the $LiNbO_3$ wafer. As a result, all regions on the Ti:Er:$LiNbO_3$ will have erbium ions in it and thus renders the whole wafer useless for other passive devices as they will be very lossy due to the erbium absorption at the 1.5 μm wavelength range.

We have demonstrated on-chip optical amplification through the fabrication of Er-doped Ti:$LiNbO_3$ waveguide amplifier. The doping of erbium was carried out in a diffusion furnace at 1100 °C in dry oxygen and argon. The maximum net gain or fiber-to-fiber device gain for an 11 μm wide and 20 mm long Er:Ti:$LiNbO_3$ waveguide amplifier is 2.3 ± 0.1 dB at around λ = 1532 nm. This includes the fiber to waveguide coupling losses and was reached at a combined pump power of 182mW with two 1488 nm lasers. Optical small-signal internal gain of 1.8 dB/cm (TE mode) and 1.5 dB/cm (TM mode) at 1531 nm was also obtained from a 7 μm wide and 40 mm long Er:Ti:$LiNbO_3$ waveguide amplifier . The internal gain discounts the fiber to waveguide coupling losses and was also reached at a combined pump power of 182mW with two 1488 nm lasers. Although the optical gain of our Er:Ti:$LiNbO_3$ waveguide amplifier is among the highest reported so far, we have decided to explore other ways of making EDWA with our fabrication processes. This will further increase the versatility of our hybrid waveguides.

5. ERBIUM-DOPED AS_2S_3 THIN FILM BY MULTI-LAYER SPUTTERING

5.1 Background

Chalcogenide hosts such as As_2S_3 is particularly suited as a host for erbium because this material exhibits very low phonon energies and does not inherently contain any hydroxyl or silicon oxide groups. Hosts with low-phonon energy are desired for rare-earth ions because multi-phonon relaxation pathways can result in a rapid depopulation of the upper excited state and cause quenching of the photoluminescence. As a rule-of-thumb, the rare-earth photoluminescence will be completely quenched by multi-phonon relaxations if the phonon cut-off energy of the matrix is greater than 25 % of the energy gap between the upper excited state and the lower electronic state of the rare earth ion. Since the phonon energy of As_2S_3 was reported to be about 6.9 % of the energy gap of erbium, quenching due to multi-phonon relaxation in As_2S_3 will be negligible [27].

As is mentioned in section 4, the telecommunications spectrum is not a continuous spectrum, but it is separated into low-loss windows. The reason for this division is because silica, which is used in the manufacturing of optical glass fibers, intrinsically contains hydroxyl- and Si-O groups. The free-radical and vibration overtones of these hydroxyl- and Si-O species are situated at 950 nm, 1240 nm, and 1400 nm and the presence of these absorption bands is the reason why the telecommunications spectrum is divided into several low-loss windows. Although, a decrease in Rayleigh scattering through the reduction of impurities is technically achievable by using highly pure quartz

as the precursor material, the presence of hydroxyl- and Si-O groups are intrinsic to silica and cannot be eliminated. Therefore, the added benefit of using chalcogenide based glasses such as As_2S_3 is its absence of the hydroxyl- and Si-O groups. In fact, As_2S_3 is free of absorbers between the wavelengths of 700 nm to 3 μm and is therefore highly transparent at these wavelengths. This suggests that devices fabricated with this material can access the entire telecommunications spectrum from 1200 nm wavelength to 1600 nm wavelength thus enabling access to an extra 100 nm or 25 % more wavelength channels over silica based devices [27].

There are a several ways to incorporate rare earth elements into chalcogenide films. It can be done by RF sputtering from custom made target or vacuum co-evaporation of chalcogenide glass and rare earth doped chalcogenide powder [25, 70, 71]. The custom-made sputtering target can either be from a commercial undoped target with erbium pieces on the surface, or made from grounding a rare earth doped chalcogenide bulk glass ingot into powder and hot pressing the power into a disk. Similar methods have also been adopted to incorporate erbium into As_2S_3 thin film. To date, demonstrations include co-evaporation method and the ion implantation method, which the As_2S_3 films were formed by thermal evaporation and the erbium was doped into the film by subsequent ion implantation [27, 72].

Since a direct current sputtering process is often very stable and reproducible, and we can independently control the sputtering rate of erbium, we believe that multi-layer

magnetron sputtering can provides a more precise control on the doping concentration of erbium. Once calibrated, the concentration level can either be determined by the number of erbium layers in the film or by the sputtering rate. Moreover, the region with the highest concentration of erbium in the Er:As_2S_3 can be tailored to match the mode profiles of both the pump laser and the signal propagating in the waveguide. In this way, we can increase the effective absorption and emission cross-sections of erbium in the Er:As_2S_3 and raise the gain of the erbium doped waveguide amplifier.

Another major motivation for magnetron sputtering Er:As_2S_3 is that the process will produce an As_2S_3 film that is closer to their ideal stoichiometry. Any deviation from the ideal stoichiometry is undesired because it would not only change the optical properties of the film, e.g. refractive index, which is a critical parameter in waveguide design, but also make the material more susceptible to room temperature oxidation such as photo-induced As_2O_3 crystals. This is especially important for the fabrication of As_2S_3 waveguides, as very often the as-deposited As_2S_3 film prepared by resistive thermal evaporation or pulsed laser deposition, will oxidize into As_2O_3 when it comes into contact with oxygen in the ambient environment [39, 47, 48]. Even though a number of advanced processing methods have been proposed to solve these problems, the proposed methods in the literature still require the breaking of vacuum after the film is deposited and so will not effectively stop the oxidation process in the As_2S_3 film [43-46].

5.2 Experimental Techniques

Multi-layer sputtering of Er and As_2S_3 on $LiNbO_3$ substrate can be done by staggered deposition of erbium from a 2-inch 99.99% pure erbium target (American Elements Inc., Los Angeles, CA 90024)) and As_2S_3 from a 2-inch AMTIR-6 target (Amorphous Materials, Inc., Garland, TX 75042) in a sputtering system. However, due to the need to keep both plasmas lit throughout the process and to balance a relatively slower deposition rate of As_2S_3 (~ 0.06 nm/s) with the tiny amount of erbium needed (~ 0.5 – 2.0 at. % Er), we will have to slow down the deposition rate of erbium by modulating its shutter during the run. Lowering the DC power alone is not enough to slow down erbium deposition rate, as the process is usually fixed at the working pressure and flow rate of argon of As_2S_3 due to the very demanding deposition conditions of magnetron sputtering As_2S_3 [49]. By setting the on and off time of the shutter, we are then able to maintain the deposition rate of erbium at a fractional rate of As_2S_3. This allows us to eventually control the desired concentration level of erbium in the composite film. Fig. 30 illustrates the multi-layer film structure created by the staggered deposition of Er and As_2S_3 and by modulating the erbium shutter.

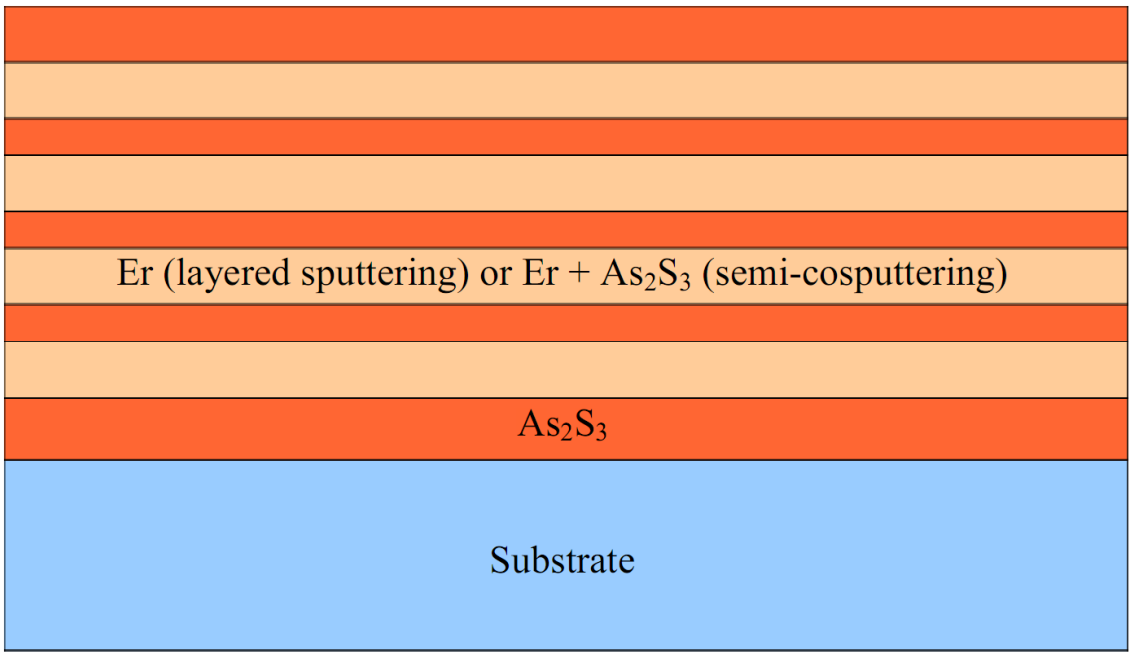

Fig. 30. A staggered deposition of a multi-layer Er:As_2S_3 film. The film structure of a multi-layer Er:As_2S_3 film prepared by staggered deposition. If the shutter of the As_2S_3 target is closed during the deposition of Er, the process is called layered sputtering, otherwise it is semi-cosputtering.

In Fig. 31, the picture shows the location of the three sputtering targets used for preparing the Er:As_2S_3 film. To the left we have the As_2S_3 target, Er target is at the center of the chamber and the SiO_2 target is to the right. All the shutters are positioned in such a way that the argon plasma can still be maintained at the closed position. The working pressure and argon flow rate of our process is kept at 2.0 mTorr and 35 sccm respectively. The film is deposited using 25 W of DC power for erbium and 35 W of RF power for As_2S_3. After the film is deposited, the Er:As_2S_3 film can then be thermally annealed at 130°C to relieve the stress in the multi-layer film. The erbium distribution

can be further improved by keeping the As_2S_3 shutter opened during the deposition of erbium. Although we termed this process cosputtering, strictly speaking it is semi-cosputtering because the erbium shutter is closed during As_2S_3 deposition.

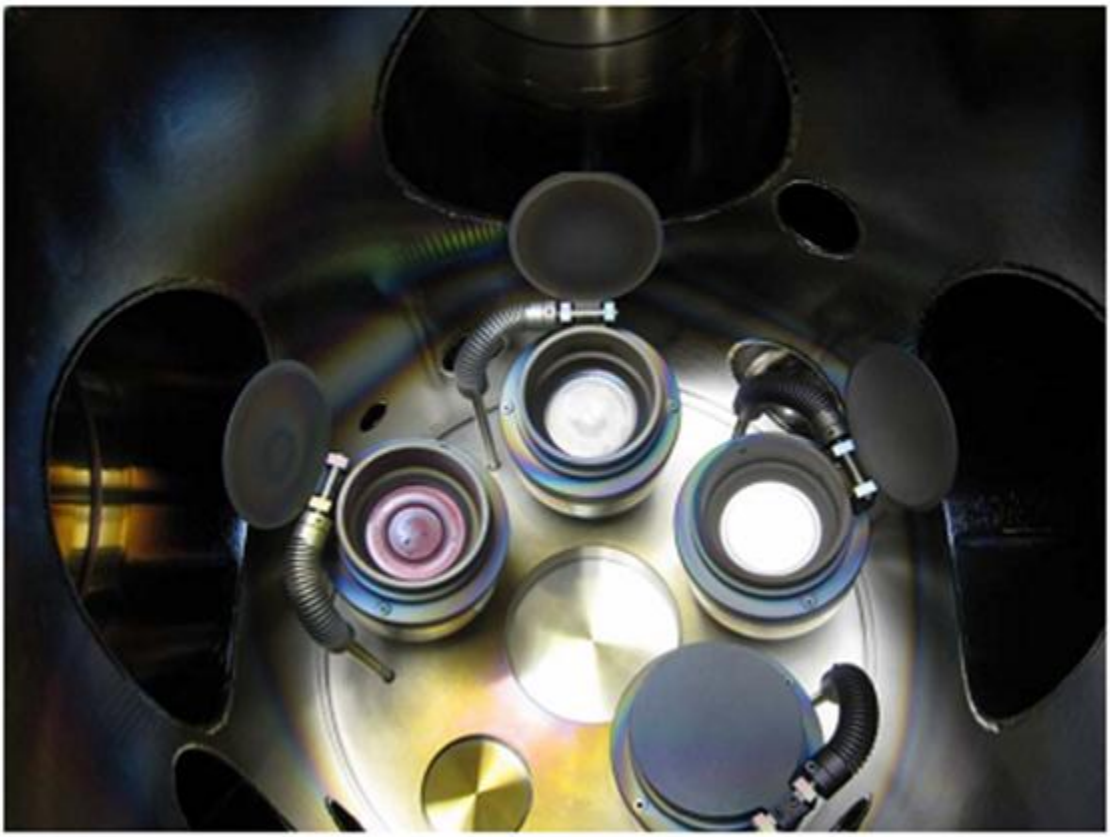

Fig. 31. A photograph of the deposition chamber inside the magnetron sputter. The picture shows the location of the three sputtering targets used for preparing the Er;As_2S_3 film. To the left we have the As_2S_3 target, Er target is at the center of the chamber and the SiO_2 target is to the right. All the shutters are positioned in such a way that the Ar plasma can still be maintained at the closed position.

The optical properties, refractive index n and extinction coefficient κ, and the thickness of the film were measured by reflection spectroscopy over the wavelength range of 400 – 850 nm with a spectrometer (F20, Filmetrics, Inc., San Diego, CA 921123). The average non-uniformity of the films was around ± 15 nm and the film's thickness was independently verified with a surface profiler. The variations in the measured thickness among the spectrometer and surface profiler were within ± 20 nm.

X-ray photoelectron spectroscopy (XPS) is used to examine the chemical composition on the surface of the film. This will determine the degree of deviation from ideal As_2S_3 stoichiometry the multilayer sputtering process has introduce into the Er:As_2S_3 film, as we have just incorporated an Er dopant into the As_2S_3 host matrix. Any deviation from the ideal stoichiometry is undesired because it would not only change the optical properties of the film, e.g. refractive index, which is a critical parameter in waveguide design, but also made the material more susceptible to room temperature oxidation such as photo-induced As_2O_3 crystals [49]. Although XPS is only a surface analysis tool, a surface examination that shows little deviation from its ideal stoichiometry is also a strong indication of the overall integrity of the chemical composition of the film. Since all the surface of the film is exposed to the environment and thus most prone to any contaminations. This can be verified with Rutherford backscattering spectroscopy.

The XPS analysis is carried out on a Kratos Axis Ultra Imaging X-ray photoelectron spectrometer (Kratos Analytical Inc., Chestnut Ridge, NY 10977). The scanning of the

kinetic energy of the electrons is done at a chamber pressure, $P < 9\times10^{-7}$ Torr. The analyzer is set to spectrum mode, the resolution is 40 eV, the current is 10 mA, and the anode HT is 12 kV. The End eV for each elements, namely O 1s, C 1s, S 2p, and As 3d, are all set to be 3 eV lower than the default value. The sweeps time is 60 second and the number of sweep is five. All the binding energies were corrected to reflect the correct binding energy of C 1s at 284.8 eV.

We study the stoichiometry and homogeneity of the Er:As_2S_3 thin films prepared by multi-layer magnetron sputtering using Rutherford back-scattering spectroscopy (RBS). In RBS, the Rutherford backscattering of an elastic (hard-sphere) collision between a high kinetic energy particle from the incident beam (the projectile) and a stationary particle located in the sample (the target) is measured. The energy loss of a backscattered ion is dependent on two processes: the energy lost in scattering events with sample nuclei, and the energy lost to small-angle scattering from the sample electrons.

The first process is dependent on the scattering cross-section of the nucleus and thus on its mass and atomic number. For a given measurement angle, nuclei of two different elements will therefore scatter incident ions to different degrees and with different energies, producing separate peaks on an N(E) plot of measurement count versus energy. These peaks are characteristic of the elements contained in the material, providing a means of analyzing the composition of a sample by matching scattered energies to

known scattering cross-sections. Relative concentrations can be determined by measuring the heights of the peaks.

The second energy loss process, the stopping power of the sample electrons, does not result in large discrete losses such as those produced by nuclear collisions. Instead it creates a gradual energy loss dependent on the electron density and the distance traversed in the sample. This energy loss will lower the measured energy of ions which backscatter from nuclei inside the sample in a continuous manner dependent on the depth of the nuclei. The result is that instead of the sharp backscattered peaks one would expect on an N(E) plot, with the width determined by energy and angular resolution, the peaks observed trail off gradually towards lower energy as the ions pass through the depth occupied by that element. Elements which only appear at some depth inside the sample will also have their peak positions shifted by some amount which represents the distance an ion had to traverse to reach those nuclei.

In practice, a compositional depth profile can then be determined from an RBS N(E) measurement. The elements contained by a sample can be determined from the positions of peaks in the energy spectrum. Depth can be determined from the width and shifted position of these peaks, and relative concentration from the peak heights. This is especially useful for the analysis of a multilayer sample, for example, or for a sample with a composition which varies more continuously with depth.

The RBS analysis for our films is carried out with a 2 MeV He beam incident along the sample normal direction, with backscattered He atoms detected by a solid state detector with an energy resolution of 20 keV. The detector is located 165 degrees away from the beam incident directions.

Other than Rutherford back-scattering spectroscopy, Raman spectroscopy can also be used to examine the chemical composition of our film. It is a spectroscopic technique used to study vibrational, rotational, and other low-frequency modes in a system. It relies on inelastic scattering, or Raman scattering, of monochromatic light, usually from a laser in the visible, near infrared, or near ultraviolet range. The laser light interacts with molecular vibrations, phonons or other excitations in the film, resulting in the energy of the laser photons being shifted up or down. The shift in energy gives information about the phonon modes in the film. Typically, a sample is illuminated with a laser beam. Light from the illuminated spot is collected with a lens and sent through a monochromator. Wavelengths close to the laser line, due to elastic Rayleigh scattering, are filtered out while the rest of the collected light is dispersed onto a detector. In this application, Raman spectroscopy is especially useful for detecting any clustering of erbium dopants with the host elements, especially sulphur, in the As_2S_3 host matrix.

The Raman analysis is carried out on the Horiba Jobin-Yvon LabRam IR system, which combines both the confocal Raman microscopy and complementary FTIR micro-spectroscopy in a single benchtop system. The CCD detector has a spectral range of 400

to 950 nm. The excitation is done with a 633 nm He Ne laser capable of reaching 17 mW. The pinhole is set to 200 μm, the grating is 1800 lines per mm, the objective lens is at 50 times, and the optical density filter is set at 0.6.

5.3 Results and Discussion

Once we have determined the deposition conditions required for generating the Er:As_2S_3 film, the optical properties, thickness, chemical composition and erbium concentration must also be determined before it can be used for device fabrication.

In Fig. 32, we have the refractive index of an as-deposited As_2S_3 and two as-deposited Er:As_2S_3 films with 4 and 16 layers of erbium. This constitutes about 0.6 and 0.7 atomic percent of erbium in the Er:As_2S_3 films respectively. All the films including the As_2S_3 were prepared by magnetron sputtering. It can be seen from the figure that both the 4-layer and 16-layer Er:As_2S_3 films follow closely the As_2S_3 with a maximum difference in the refractive index of about 0.02. Moreover, increasing the number of erbium layers four times to increase the homogeneity of erbium in the Er:As_2S_3 film does not result in any drastic changes in refractive index. In fact, the index of refraction looks almost identical to the sputtered As_2S_3 film. The film thickness of the Er:As_2S_3 with four layers of erbium is 276 ± 2 nm and 460 ± 20 nm for the sixteen layers of erbium. The thickness of the magnetron sputtered As_2S_3 film is 461 ± 20 nm.

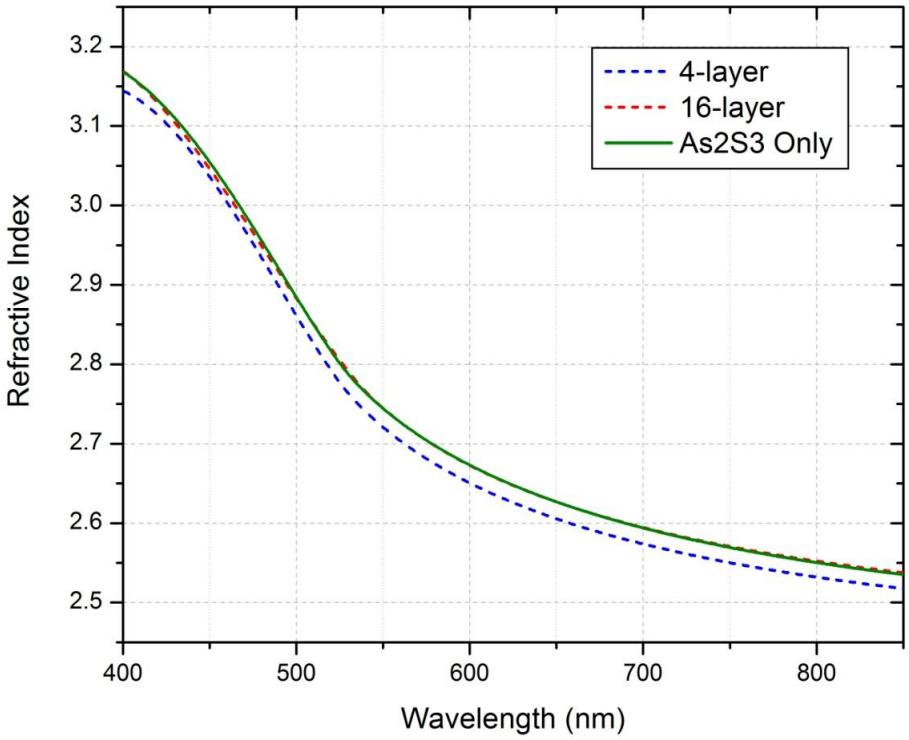

Fig. 32. The refractive index of as-deposited As_2S_3 and Er:As_2S_3 films. The films were prepared by magnetron sputtering. In the figure, As2S3 refers to a magnetron sputtered As_2S_3 film. It shows both the 4-layer and 16-layer Er:As_2S_3 films follow closely the As_2S_3 film and increasing the number of erbium layers four times to increase the homogeneity of erbium in the Er:As_2S_3 film does not result in any drastic changes in refractive index. The film thickness of the Er:As_2S_3 with four layers of erbium is 276 ± 2 nm and 460 ± 20 nm for the sixteen layers of erbium. The magnetron sputtered As_2S_3 film is 461 ± 20 nm.

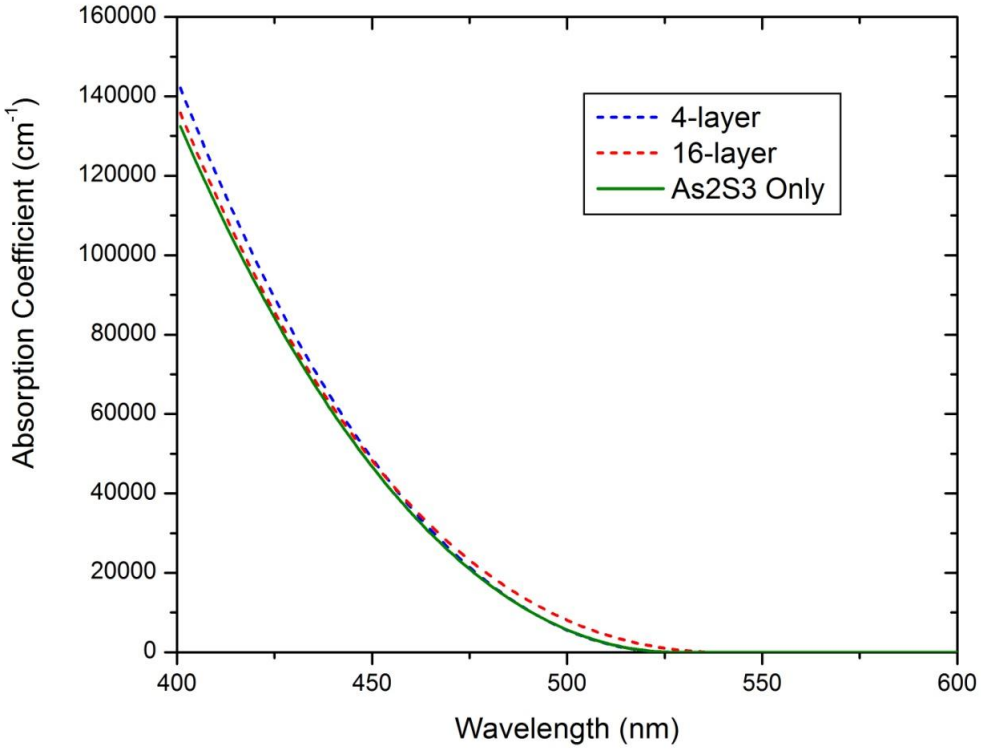

Fig. 33. The absorption coefficient of as-deposited As_2S_3 and Er:As_2S_3 films. The films were prepared by magnetron sputtering. It shows both the 4-layer and 16-layer Er:As_2S_3 films follow closely the As_2S_3 film and increasing the number of erbium layers 4 times to increase the homogeneity of erbium in the Er:As_2S_3 film caused no drastic changes in the absorption coefficient of the film. The film thickness of the Er:As_2S_3 with four layers of erbium is 276 ± 2 nm and 460 ± 20 nm for the sixteen layers of erbium. The magnetron sputtered As_2S_3 film is 461 ± 20 nm.

The Fig. 33 shows the absorption coefficient of the as-deposited As_2S_3 and Er:As_2S_3 films with 4 and 16 layers of erbium. Similar to the refractive index measurement, the absorption coefficient of the 4-layer and 16-layer Er:As_2S_3 films, which can be easily derived from the extinction coefficient taken from the spectrometer, also follow closely

the As_2S_3 film. Increasing the number of erbium layers 4 times to increase the homogeneity of erbium in the Er:As_2S_3 film also does not result in any drastic changes in the coefficient. The result proves that the doping process will not change the optical properties of As_2S_3 film and thus the same design parameters developed for As_2S_3 waveguide can be used for Er:As_2S_3 waveguide.

X-ray photoelectron spectroscopy is used to examine the chemical composition on the surface of the film. In Fig. 34, we have the XPS high resolution spectrum of the electrons in arsenic 3d shell in four magnetron sputtered Er:As_2S_3 films on a 1 cm^2 silicon wafer. From the peaks of the binding energy, we can see that no amount of oxidation can be found on the surface of the film as the energy peaks of the electrons in the arsenic 3d shell (As-3d) of all the films are lower than 44.0 eV. This result implied that the surface of our films, whether as-deposited or annealed at 130 °C, have not oxidized into As_2O_3 or As_2O_5. According to data published by NIST, the binding energy of the electrons in arsenic 3d shell in a film with As_2O_3 ranges from 43.9 eV to 46.3 eV and for As_2O_5 it ranges from 45.9 eV to 46.5 eV. The refractive index of the film at λ = 640 nm with four layers of erbium is 2.61 and 2.64 for the one with eight layers of erbium and 4 layers of erbium. Thermal annealing was carried out at 130 °C in a vacuum oven in the dark.

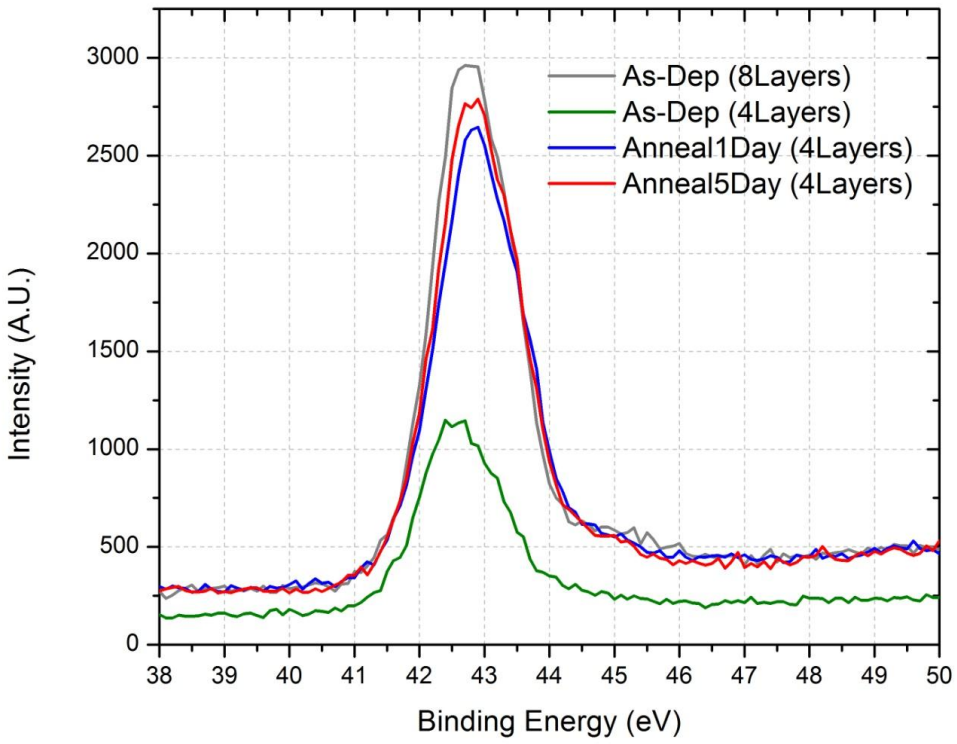

Fig. 34. High resolution XPS spectrum of As-3d shell in Er:As_2S_3 films. Since binding energy of the electrons in the arsenic 3d shell in all the sputtered films are lower than 44.0eV, the figure shows that the films, whether as-deposited or annealed at 130 °C, have not oxidized into As_2O_3 or As_2O_5 crystals on the surface. As-Dep refers to as-deposited. The film thickness of the Er:As_2S_3 with four layers of erbium is 276 ± 2 nm and 523 ± 20 nm for the eight layers of erbium.

The Fig. 35 shows the high resolution x-ray photoelectron spectroscopy spectrum of the arsenic 3d shell in four as-deposited Er:As_2S_3 films on a 1 cm^2 silicon wafer. All the binding energies were corrected to reflect the correct binding energy of C 1s at 284.8 eV and 4CoSput in the figure refers to the film with four layers of semi-cosputtered erbium. From the peaks of the binding energy, we can see that some amount of As_2O_3 crystals have been found on the surfaces of the Er:As_2S_3 with one layer of erbium and four layer of semi-cosputtered erbium. This is indicated by the binding energy of the electrons in the arsenic 3d shell in the film. Both films displayed binding energy greater than 43.8 eV, which according to the data published by NIST, is within the binding energy of As_2O_3 of 43.9 eV to 46.3 eV. The refractive index of the film at λ = 640 nm with four layers of semi-cosputtered erbium is 2.63 and 2.61 for the one with one layers of erbium and 4 layers of erbium. As for the Er:As_2S_3 film with eight layers of erbium, its refractive index at the wavelength of 640 nm is 2.64.

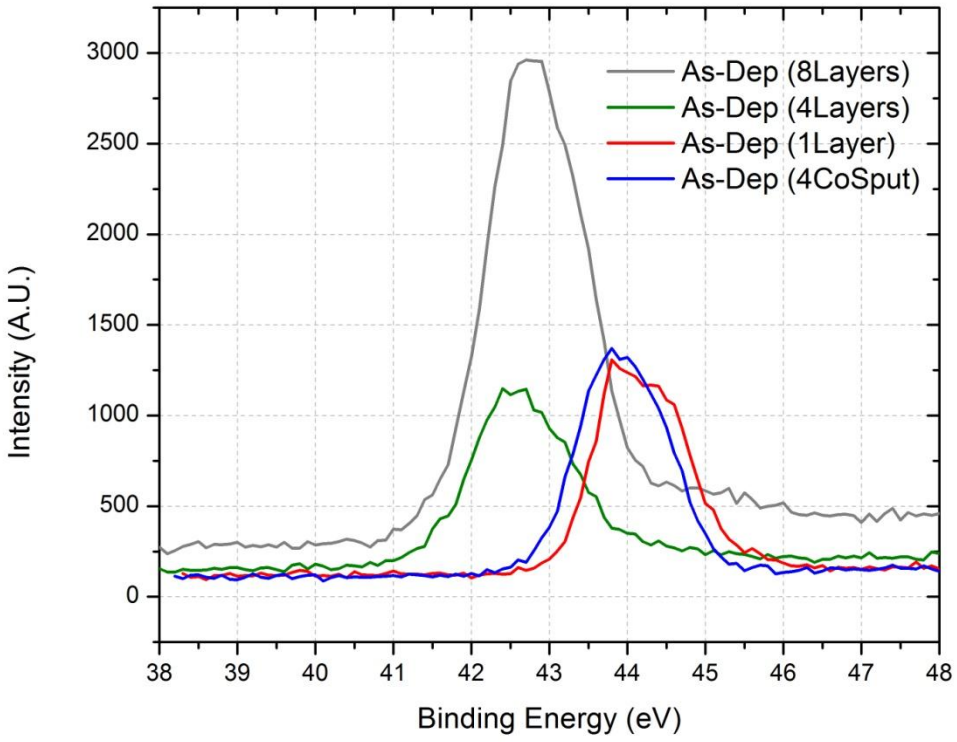

Fig. 35. High resolution XPS spectrum of As-3d shell in as-deposited Er:As_2S_3 film. In the figure, 4CoSput refers to a four layer semi-cosputtered erbium film. The figure shows that some amount of As_2O_3 crystals have been found on the surfaces of the Er:As_2S_3 film with one layer of erbium and four layer of semi-cosputtered erbium in the as-deposited state. The film thickness of the Er:As_2S_3 with four layers of erbium is 276 ± 2 nm and 523 ± 20 nm for the eight layers of erbium. The film with single layers of erbium is 456 ± 18 nm while the one with four layers of semi-cosputtered erbium is 491 ± 20 nm.

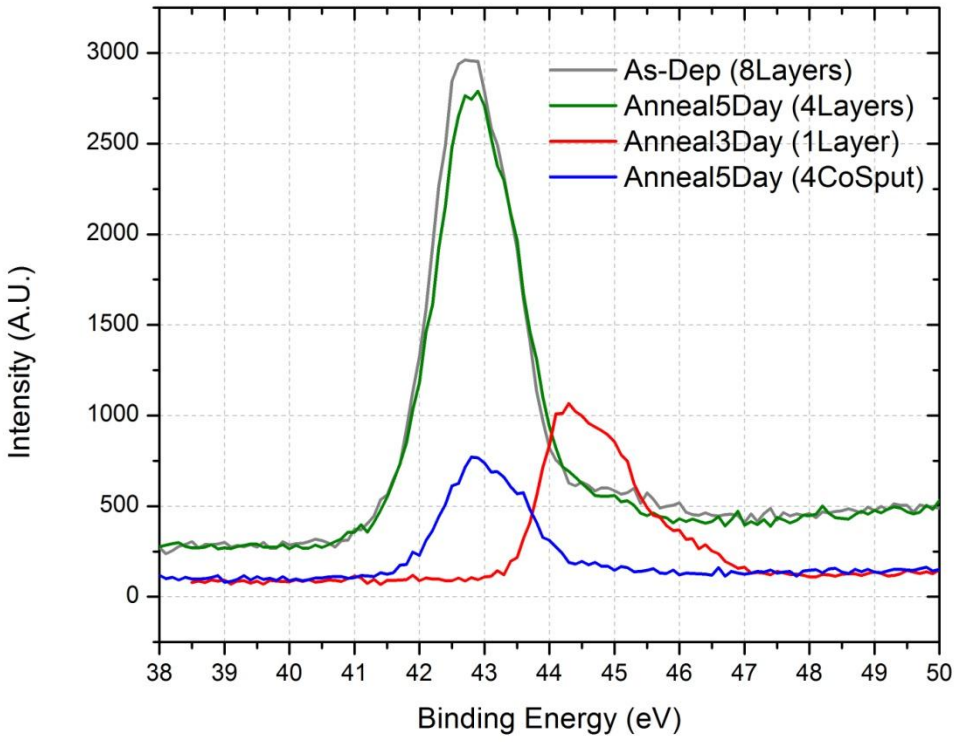

Fig. 36. High resolution XPS spectrum of As-3d shell in annealed Er:As_2S_3 films. In the figure, 4CoSput refers to four layers of semi-cosputtered Er film. The figure shows that except for the Er:As_2S_3 film with one layer of erbium, all other films showed no signs of oxidation. The film thickness of the Er:As_2S_3 with four layers of erbium is 276 ± 2 nm and 523 ± 20 nm for the eight layers of erbium. The film with single layers of erbium is 456 ± 18 nm while the one with four layers of semi-cosputtered erbium is 491 ± 20 nm.

The Fig. 36 shows the high resolution x-ray photoelectron spectroscopy spectrum of the arsenic 3d shell in Er:As_2S_3 film on a 1 cm^2 silicon wafer in their as-deposited and annealed states. All the binding energies were corrected to reflect the correct binding energy of C 1s at 284.8 eV and 4CoSput in the figure refers to the film with four layers of semi-cosputtered erbium. From the peaks of the binding energy, we can see that except for the Er:As_2S_3 with one layer of erbium, no oxidation can be found on the surface of all the other Er:As_2S_3 films. This is indicated by the binding energy of the electrons in the arsenic 3d shell in their films. Of all the films in the figure, only the film with a single layer of erbium displayed a binding energy greater than 44 eV, which according to the data published by NIST, is within the binding energy of As_2O_3 of 43.9 eV to 46.3 eV. Thermal annealing was carried out at 130 °C in a vacuum oven in the dark. For the film with four layers of semi-cosputtered erbium, the refractive index at λ = 640 nm is 2.63. It is 2.61 for the film with four layers of erbium and 2.64 for the film with eight layers of erbium. The film with one layers of erbium has a refractive index of 2.61 at λ = 640 nm.

We study the stoichiometry and homogeneity of the Er:As_2S_3 thin films prepared by multi-layer magnetron sputtering using Rutherford back-scattering spectroscopy. In the RBS experimental spectrum, the signal of each element can be clearly resolved in its own channel. The channel beginning at 460 is assigned to erbium, 400 assigned to arsenic, 285 assigned to sulfur, 235 and 215 are assigned to silicon. There are two channels for silicon because elements which only appear at some depth inside the sample

will also have their peak positions shifted by some amount which represents the distance an ion had to traverse to reach those nuclei. Fig. 37 shows the RBS spectrum of two thermally annealed Er:As_2S_3 films on a 1 cm^2 Si wafer. In the figure, 16-Layer refers to the Er:As_2S_3 film with sixteen layers of erbium and 4-cosput refers to four layers of semi-cosputtered erbium. The spectrums of pure Er and As_2S_3 films are included as a reference to help us differentiate the various elements, e.g. Er, As and S, in our Er:As_2S_3 films. The figure confirms we have the right type element in our Er:As_2S_3 film. There are no unknown elements in the spectrum that indicate contamination or oxidation. It also shows that the semi-cosputtered film is thicker than the Er:As_2S_3 film with sixteen layers of erbium.

The Fig. 38 shows the RBS spectrum of the Er element in those thermally annealed Er:As_2S_3 films prepared by multi-layer magnetron sputtering. In the figure, 16-Layer refers to Er:As_2S_3 film with sixteen layers of erbium and 4-cosput refers to four layers of semi-cosputtered erbium. The spectrum of pure Er is included as a reference to help us locate the elements in the Er:As_2S_3. The figure not only shows the staggered nature of the semi-cosputtered Er:As_2S_3, but also confirms we have produced a homogeneously doped Er:As_2S_3 film with sixteen layers of erbium. Bad homogeneity of a glass during fabrication can lead to the presence of stripes with different densities, which will cause additional losses in the optical signal due to scattering.

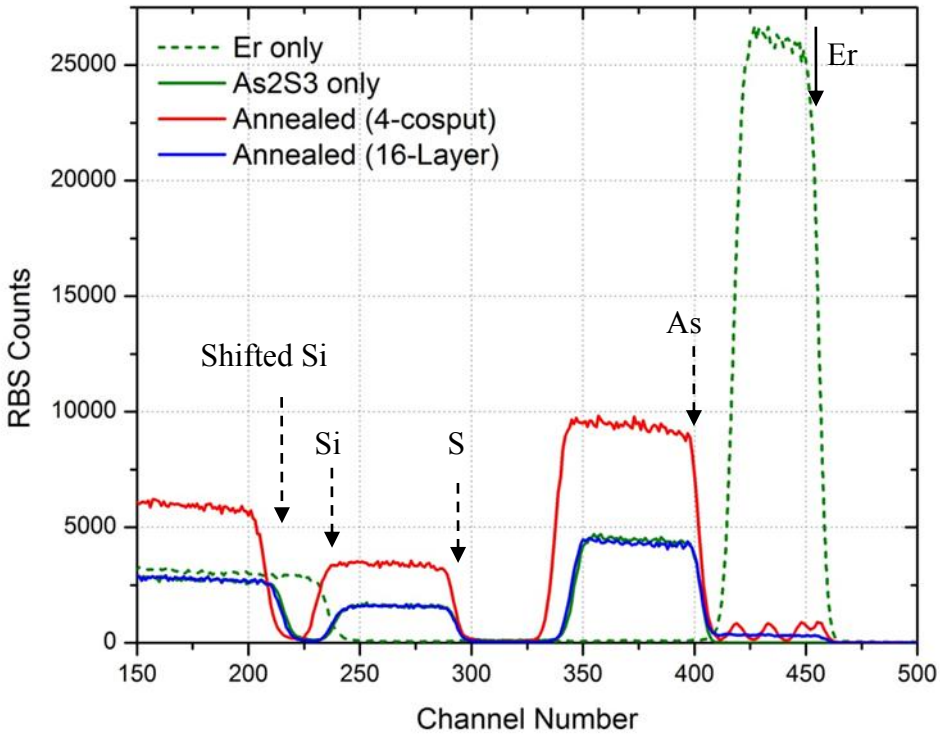

Fig. 37. The RBS spectrum of thermally annealed Er:As_2S_3 films on Si wafer. In the figure, 16-Layer refers to sixteen layers of erbium and 4-cosput refers to four layers of semi-cosputtered erbium. The spectrum of pure Er and As_2S_3 are included as a reference to help us differentiate the various elements, Er, As and S, in the Er:As_2S_3. The figure confirms no unknown elements in the spectrum that can indicate contamination or oxidation in Er:As_2S_3. The thickness of the erbium film is 200 ± 20 nm and 461 ± 20 nm for As_2S_3. The film with sixteen layers of erbium is 460 ± 20 nm while the one with four layers of semi-cosputtered erbium is 491 ± 20 nm.

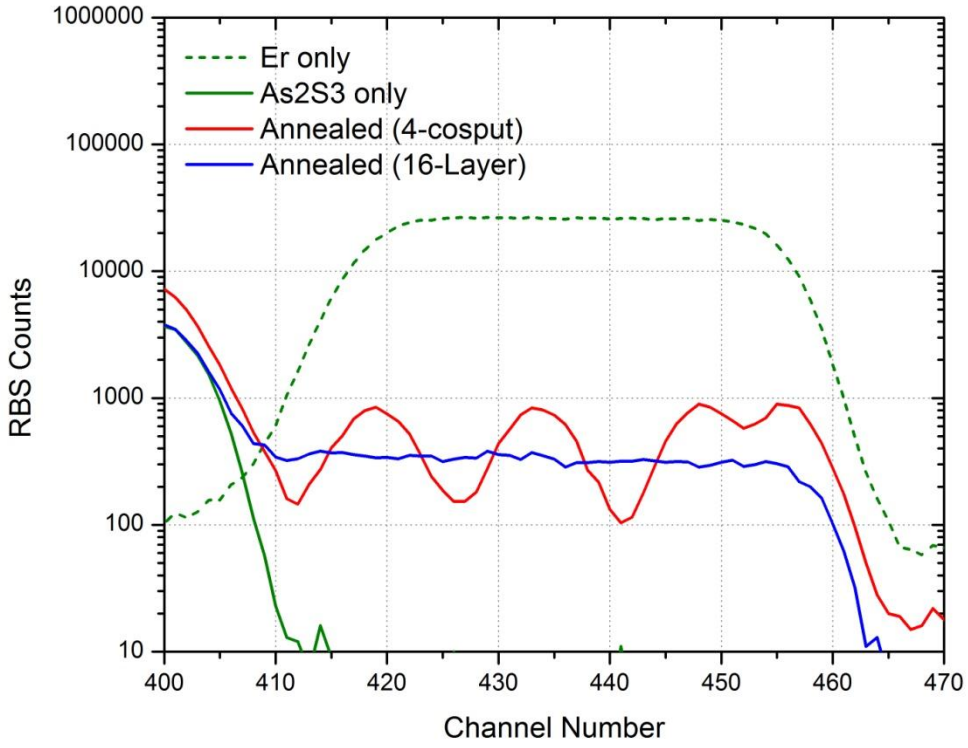

Fig. 38. The RBS spectrum of Er element in thermally annealed Er:As_2S_3 films. In the figure, 16-Layer refers to sixteen layers of erbium and 4-cosput refers to four layers of semi-cosputtered erbium. The spectrum of pure Er film is included as a reference to help us locate the elements in Er:As_2S_3. The figure confirms we have achieved a homogeneously doped Er:As_2S_3 film with sixteen layers of erbium. It also shows the staggered nature of the semi-cosputtered Er:As_2S_3. The number of layers agrees with the deposition process. The thickness of the erbium film is 200 ± 20 nm and 461 ± 20 nm for As_2S_3. The film with sixteen layers of erbium is 460 ± 20 nm while the one with four layers of semi-cosputtered erbium is 491 ± 20 nm.

To analyze the data, the erbium, arsenic and sulfur channels in the experimental spectrum were simulated with a box shaped profile as shown in Fig. 39. In the simulation, the overall width of the peak was proportional to the physical thickness of the film, and its area beginning at the high energy edge and ending at the low energy edge, represented the concentration of each element in the film. In order to extract the compositional information from the experimental data, each peak is simulated by a summation of thin slices. Physically, the thickness of each thin slice in the simulation represented a planar layer inside the film that was parallel to the substrate. The height of each slice represented the concentration of that element at a particular planar layer. Fig. 39 shows the simulation of a RBS spectrum of a thermally annealed Er:As_2S_3 film. The film has four layers of semi-cosputtered erbium.

The simulation software, RBX, found 4 layers of As_2S_3 and Er in the film. Starting from the substrate, we have 120 nm of As_2S_3, follow by 0.5 nm of Er. This is follows by 130 nm of As_2S_3 and 0.5 nm of Er, and top up by another 130 nm of As_2S_3 and 0.5 nm of Er. Finally a 100 nm of As_2S_3, and 0.5 nm of Er at the top. The density of the As_2S_3 and Er are around 3.3×10^{22} atoms per cm^3 and 3.2×10^{22} atoms per cm^3 respectively. Using the density and the total thickness of all the erbium layers from the simulation, the erbium concentration in the Er:As_2S_3 film with four layers of semi-cosputtered erbium is calculated to be 0.4 atomic percent. The measured thickness of the Er:As_2S_3 with four layers of semi-cosputtered erbium is 491 ± 20 nm and this is closed to the thickness of 482 nm obtained from the simulation.

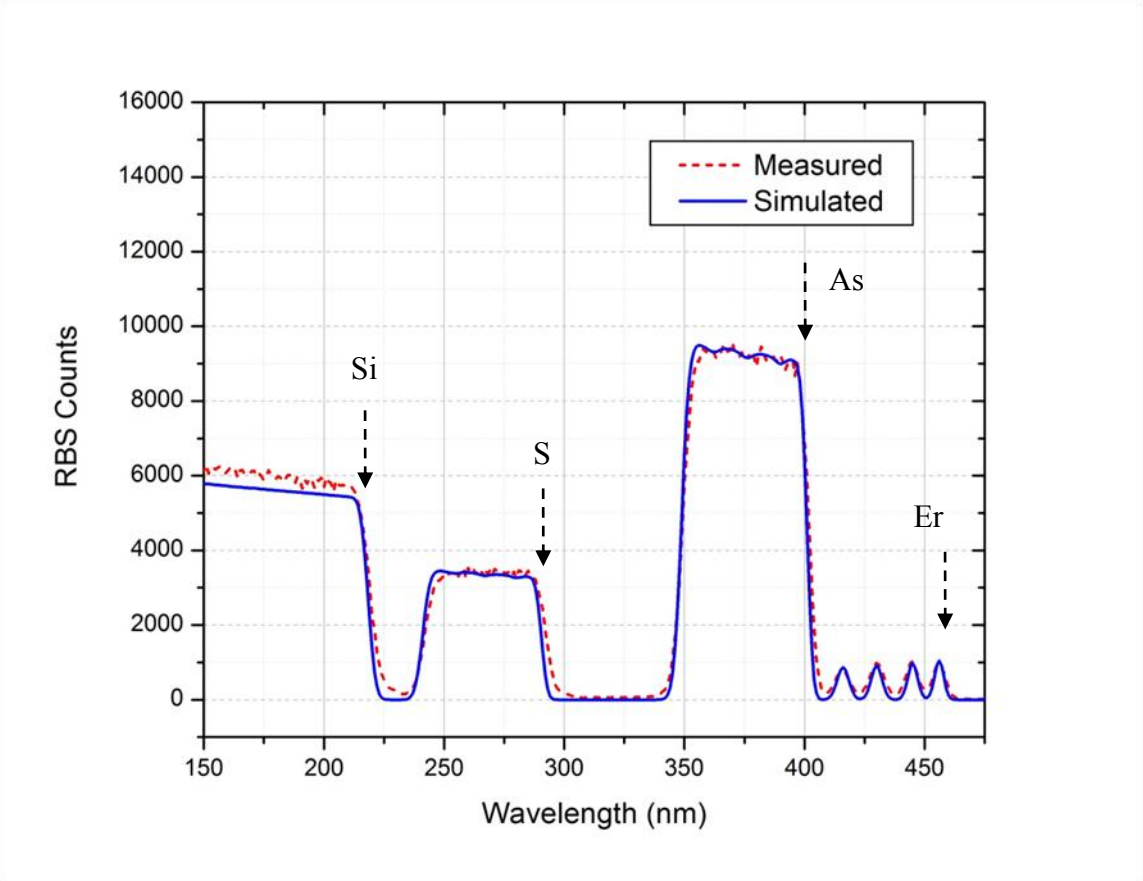

Fig. 39. The simulation of a RBS spectrum of a thermally annealed Er:As_2S_3 film. The film has four layers of semi-cosputtered erbium. The simulation software, RBX, found four layers of As_2S_3 and Er in the film. Starting from the substrate, we have 120 nm of As_2S_3, follow by 0.5 nm of Er, follow by 130 nm of As_2S_3, follow by 0.5 nm of Er, follow by another 130 nm of As_2S_3, follow by another 0.5 nm of Er, and finally a 100 nm of As_2S_3, and 0.5 nm of Er at the top. The density of the As_2S_3 and Er are 3.3×10^{22} atoms per cm^3 and 3.2×10^{22} atoms per cm^3 respectively. The erbium concentration in the film is calculated to be 0.4 atomic percent. The measured thickness of the Er:As_2S_3 with four layers of semi-cosputtered erbium is 491 ± 20 nm and this is closed to the thickness of 482 nm obtained from the simulation.

The Fig. 40 shows the simulation of the RBS spectrum of another Er:As_2S_3 film prepared by multi-layer magnetron sputtering. The film is thermally annealed and has sixteen layers of erbium in it. From the figure, we can see that the width of the boxes representing each of the elements is approximately equal to each other and the tops of the boxes are relatively flat. This indicates that the film is homogenously doped as each element present in the film had a constant concentration throughout the thickness of the film. According to the simulation, the stoichiometry of the film is $Er_{0.7}As_{39.1}S_{60.2}$, the film thickness is 475 nm, the density of the film is 3.6×10^{22} atoms per cm^3 and the erbium concentration in the film is calculated to be 2.35 wt. %. This agrees with the measured thickness taken from a spectrometer is 460 ± 20 nm and the average thickness taken from a surface profiler is 467 ± 21 nm. The RBS spectrum obtained looks very similar to a homogeneously Er-doped As_2S_3 photo-resist fabricated by co-evaporation reported in the literature [73]. These RBS results clearly showed that the multi-layer technique was able to produce homogeneous Er:As_2S_3 film with controlled stoichiometry that is free of contamination too.

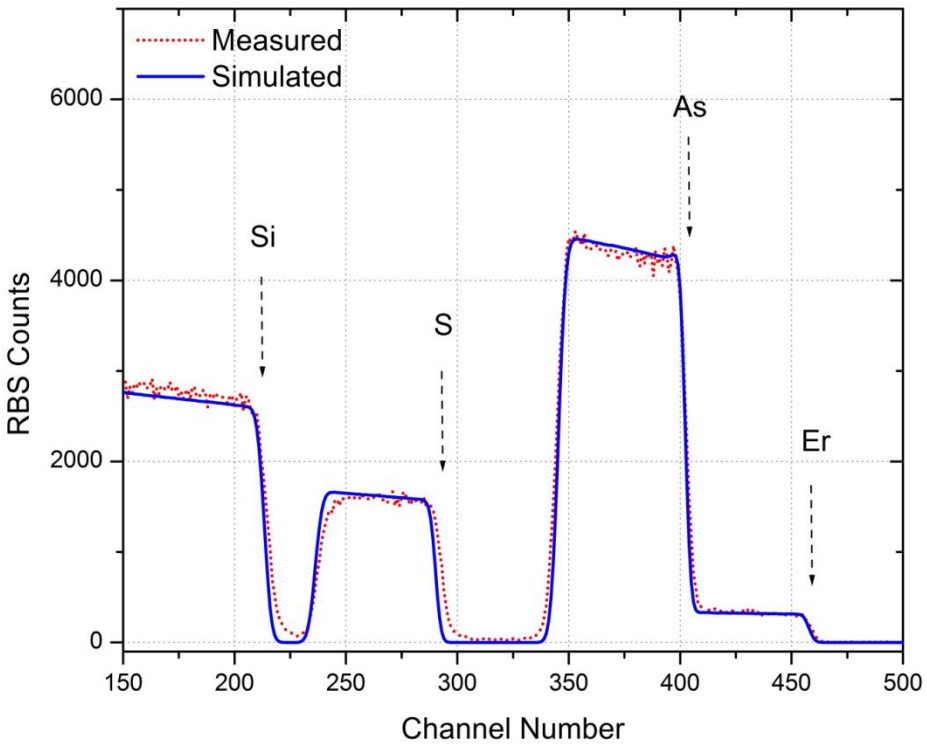

Fig. 40. The simulation of a RBS spectrum of a homogeneously doped Er:As_2S_3. The film is thermally annealed and has 16 layers of erbium in it. The figure shows that the simulation agrees well with the measured spectrum and the erbium is uniformly distributed in the film. The stoichiometry of the film is $Er_{0.7}As_{39.1}S_{60.2}$ and according to the simulation, density of the film is 3.6×10^{22} atoms per cm^3 and the erbium concentration in the film is calculated to be 2.35 wt. %.

Raman spectroscopy was also be used to examine the chemical composition of our film. The Fig. 41 shows the Raman spectrum of some as-deposited Er:As_2S_3 films on Si substrate. In the figure, 16-Layer refers to an Er:As_2S_3 films with sixteen layers of erbium and 4-Cosput refers to four layers of semi-cosputtered erbium. The Raman spectrum of As_2S_3 film and the Si wafer are included as a reference for identifying the various Raman's peaks in the Er:As_2S_3 film. As is evident from the figure, the spectrum shows no characteristic Raman signature for Er_2S_3. It implies that Er dopant has not agglomerated into Er_2S_3 or Er-S clusters inside the As_2S_3 host matrix during the sputtering process and the film is homogeneous. This result is important because the clustering of Er centers in a host material will enhance the cooperative upconversion of Er and is detrimental to an Er-doped waveguide amplifier. According to the reference in the literature, the characteristic Raman shift of Er_2S_3 is around 700 to 900 cm^{-1} [27]. The refractive index of the magnetron sputtered As_2S_3 film is 2.638 (error = 1.29 %).

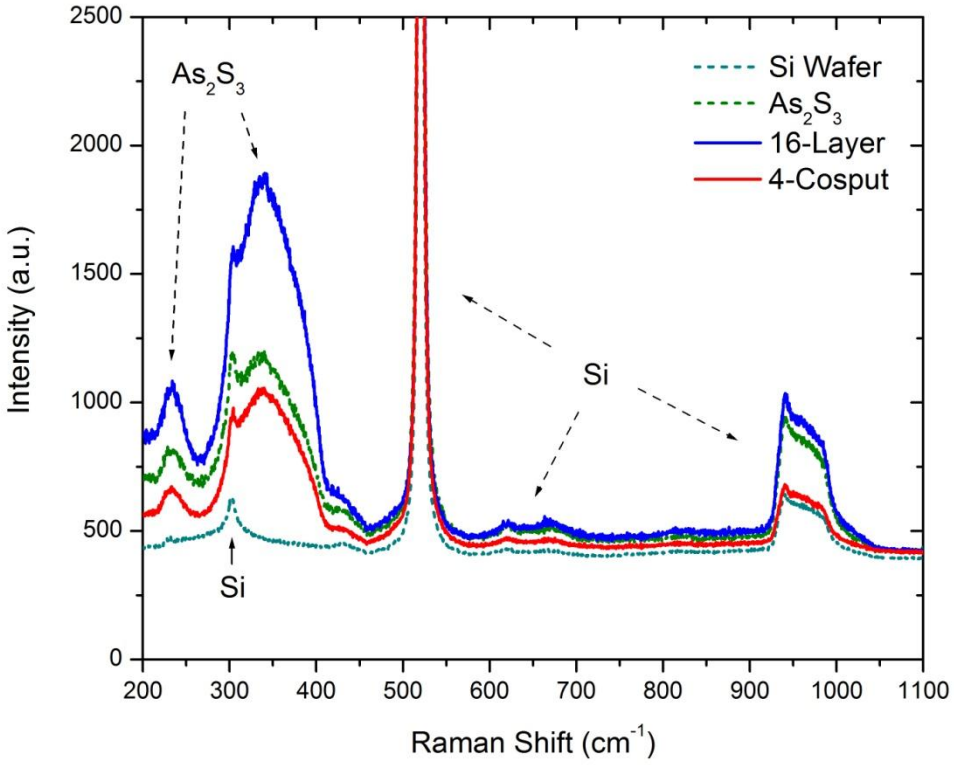

Fig. 41. Raman spectrum of as-deposited Er:As_2S_3 films on Si substrate. In the figure, 16-Layer refers to an Er:As_2S_3 films with sixteen layers of erbium and 4-Cosput refers to an Er:As_2S_3 films four layers of semi-cosputtered erbium. The spectrum shows no Raman's peak for Er_2S_3. This implies that Er dopant has not agglomerated into Er_2S_3 clusters inside the As_2S_3 host matrix during the sputtering process. The Raman spectrum of As_2S_3 film and the Si wafer are included as a reference for the various Raman's peaks in the Er:As_2S_3 films. The thickness of the As_2S_3 film is 461 ± 20 nm. The film with sixteen layers of erbium is 460 ± 20 nm while the one with four layers of semi-cosputtered erbium is 491 ± 20 nm.

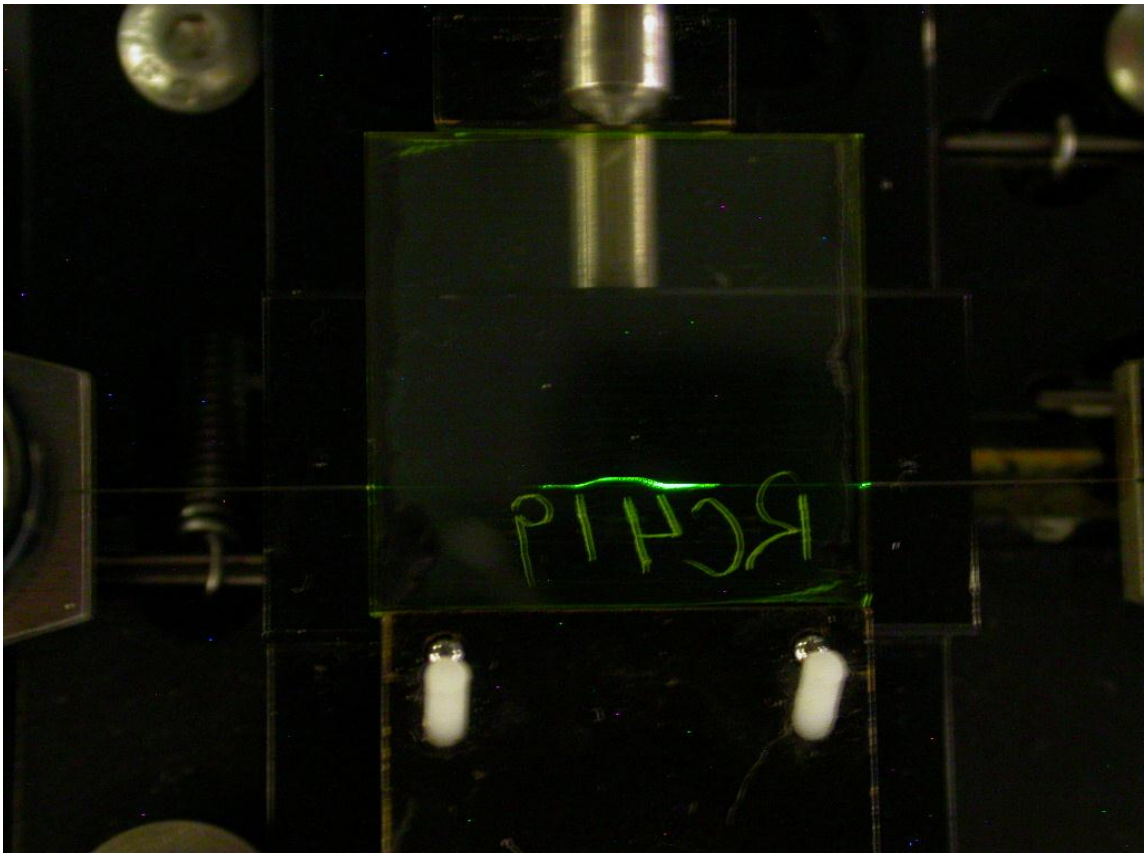

Fig. 42. The green luminescence from an Er:As_2S_3 MZI waveguide. The film was deposited by multi-layer magnetron sputtering. The 1488 nm pump signals are butt coupled into a 7 μm Ti:$LiNbO_3$ waveguide from a single mode fiber and then transfer over to the Er:As_2S_3 MZI by side coupling. The Er:As_2S_3 contains four layers of erbium deposited by cosputtering As_2S_3 during erbium deposition. The film is 490 ± 20 nm and the Er:As_2S_3 waveguide is 3.5 μm wide. The Er concentration in the film is measured to be 0.4 at. %.

In Fig. 42 we show the typical green luminescence from an integrated Er:As_2S_3 MZI waveguide prepared by multi-layer magnetron sputtering. The result implied that first of all, the coupling tapers that we have designed is able to couple the 1488 nm pump signal up into the Er:As_2S_3 waveguide. Secondly, the presence of active erbium ions in the integrated Er:As_2S_3 MZI waveguide is evident from the green luminescence it emitted when it was pumped by 1488 nm diode laser. The Er:As_2S_3 contains eight layers of erbium deposited by cosputtering As_2S_3 during erbium deposition. The film is thermally annealed at 130 C for a day, its thickness is 490 ± 20 nm and the Er:As_2S_3 waveguide is 3.5 μm wide. The measured concentration of erbium in the film is found to be 0.4 atomic percent (at. %).

Fig. 43 compares the photoluminescence of a 7 μm Er:Ti:$LiNbO_3$ waveguide amplifier described in section 4 to the Er:As_2S_3 MZI shown in Fig 44. As we can see from the figure, unlike the broad photoluminescence spectrum obtained for the Er:Ti:$LiNbO_3$ waveguide amplifier, a portion of the photoluminescence spectrum of the Er:As_2S_3 MZI is missing. This is different from the photoluminescence reported in the literature for Er:As_2S_3 glass and Er:As_2S_3 film prepared by thermal evaporation [24, 72]. Although we have no evident, we suspect it might be due the two linear tapered couplers in the hybrid MZI. This is because the proper functioning of the couplers depends on the fabrication conditions. Any unintentional changes, e.g. taper width, to the physical dimensions of the couplers during fabrication might change the coupling wavelength of the MZI. In

this case wavelength above 1530 nm is no longer able to couple up into the Er:As_2S_3 waveguide.

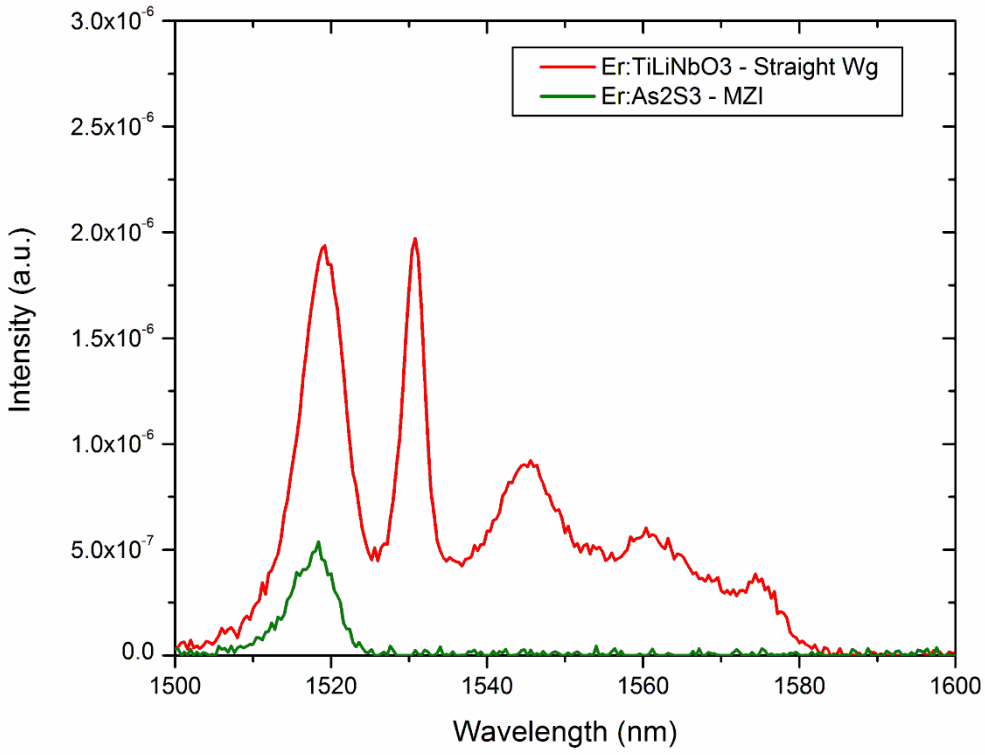

Fig. 43. The photoluminescence of Er-doped waveguides. The figure compares the photoluminescence of a 7 μm Er:Ti:$LiNbO_3$ waveguide amplifier described in section 4 to the Er:As_2S_3 MZI shown in Fig. 42.

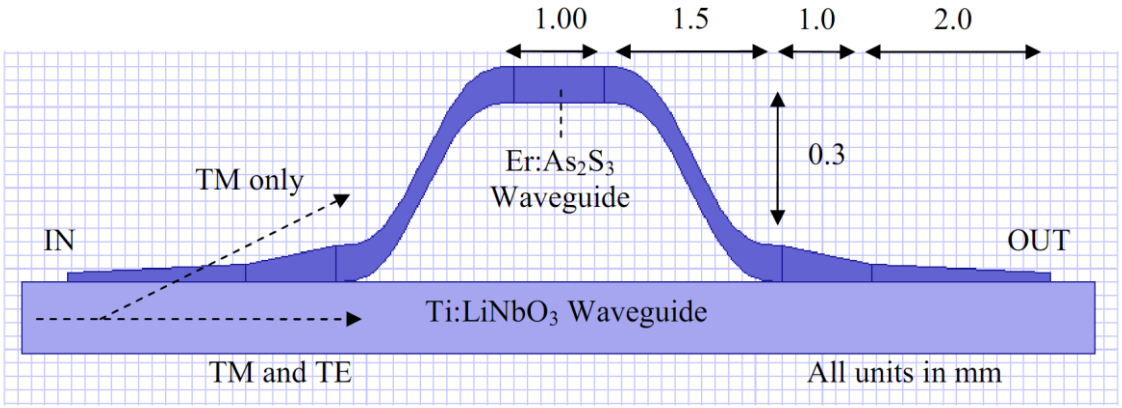

Fig. 44. The schematic drawing of an integrated Er:As_2S_3 MZI. A set of As_2S_3 S-Bend and reversed S-Bend is integrated with a straight Ti:$LiNbO_3$ to create a MZI. The width of the Ti:$LiNbO_3$ waveguide is 7 μm, the As_2S_3 waveguide is 3.5 μm, and the 2-stage As_2S_3 taper vary from 1-to-1.6 μm and then 1.6-to-3.5 μm. The arc length of the S-Bend is 1536.353 μm. TM refers to transverse magnetic propagation mode and TE refers to transverse electric mode.

In Fig. 44 we show the schematic diagram of the hybrid Er:As_2S_3 MZI. The 1488 nm pump signals are butt coupled into a 7 μm Ti:$LiNbO_3$ waveguide from a single mode fiber and then transfer over to the Er:As_2S_3 MZI by side coupling. The integrated Er:As_2S_3 MZI waveguide is pumped in both direction with a forward pump and a backward pump, which is travelling in the opposite direction to the signal. The maximum pump power obtained in this way is about 182 mW. The coupling of the pump signal is accomplished with a two-stage taper. The tip width of the first stage taper varies linearly from 1.0 μm to 1.6 μm and the taper length is about 1000 μm long. The tip width of the second stage taper varies linearly from 1.6 μm to 3.5 μm and the taper length is also about 1000 μm long. The MZI was designed using the commercial software,

OptiBPM, and consists of two cosine S-bends with one a mirror image of the other. The calculated bending radius of the S-Bend is 380 μm.

To summarize, we have demonstrated the feasibility of incorporating erbium into As_2S_3 film using multi-layer magnetron sputtering. The RBS spectrum of the Er:As_2S_3 film with sixteen layers of erbium shows a homogeneous film and Raman spectroscopy confirms there is no significant amount of Er-S clusters in the sputtered film. Moreover, the atomic concentration (39.1% of arsenics and 60.2% of sulfur) calculated from RBS is also close to the values obtained from the XPS survey scan of the sputtered As_2S_3 film (38.3% of arsenics and 61.7% of sulfur) and the As_2S_3 sputter target (40.6% of arsenics and 59.4% of sulfur). The presence of active erbium ions in the integrated Er:As_2S_3 MZI waveguide is evident from the green luminescence it emitted when it was pumped by 1488 nm diode laser.

6. SUMMARY AND CONCLUSIONS

6.1 Summary

We have measured the optical properties of *a*-As_2S_3 thin films and the propagation loss of *a*-As_2S_3 thin films on Ti:$LiNbO_3$ deposited by magnetron sputtering. While the average E_{op} of an as-deposited film remains relatively unchanged at 2.35 ± 0.04 eV when annealed, its refractive index n at λ = 1530 nm increased slightly from 2.42 to 2.43. The stoichiometry was correct and the binding energy of the As3d of the film was 43.2eV with no significant amount of As_2O_3 crystals found on the surface. The optical and structural properties agree with published results on As_2S_3 bulk glass and thus our as-deposited films are closer to the equilibrium state than *a*-As_2S_3 films made by thermal evaporation and PLD. These attributes are unique to a magnetron sputtered *a*-As_2S_3 film and we attribute it to the photo-annealing or photo-polymerizing effect caused by the visible light emitted by the argon plasma during the sputtering process. The TM propagation loss at λ = 1.5 μm of a hybrid straight waveguide is 0.20 ± 0.05 dB/cm. This result compare favorably with a recent paper on the propagation loss of an As_2S_3 waveguide with a sub-micrometer thickness of 0.83 μm.

Using the process developed, a hybrid Mach-Zehnder interferometer has been successfully fabricated with magnetron sputtering. The impulse response confirms the splitting of the TM light mode into the two pulses, one travelling in the Ti:$LiNbO_3$ and

the other in the As_2S_3 waveguide. The average group index of the integrated As_2S_3 waveguide is 2.36 when it is annealed and 2.35 when it is exposed to bandgap light.

On-chip optical amplification was achieved through the fabrication of Er-doped Ti:$LiNbO_3$ waveguide amplifier. The doping of erbium was carried out in a diffusion furnace at 1100 °C in dry oxygen and argon. The TM net gain or fiber-to-fiber device gain for an 11 μm wide and 20 mm long Er:Ti:$LiNbO_3$ waveguide amplifier is 1.2 ± 0.1 dB/cm at around λ = 1532 nm. This includes the fiber to waveguide coupling losses and was reached at a combined pump power of 182mW with two 1488 nm lasers. The TE internal gain, which discounts any coupling losses, obtained for a 7 μm wide and 40 mm long Er:Ti:$LiNbO_3$ waveguide amplifier is 1.8 dB/cm at around λ = 1532 nm. This was also reached at a combined pump power of 182mW with two 1488 nm lasers. This result put the optical gain of our Er:Ti:$LiNbO_3$ waveguide amplifier among the highest reported so far for a similar device.

We have also successfully demonstrated the feasibility of incorporating erbium into As_2S_3 film using a novel deposition method with multi-layer magnetron sputtering. The RBS spectrum of the Er:As_2S_3 film with 16 layers of erbium shows a homogeneous film and Raman spectroscopy confirms there is no significant amount of Er-S clusters in the sputtered film. The deposition method was used to fabricate an Er:As_2S_3 hybrid MZI and the presence of active erbium ions in the waveguide is evident from the green luminescence it emitted when it was pumped by 1488 nm diode laser. It also

demonstrated the viability of transferring the pump signal up into the Er:As_2S_3 waveguide with our unique two-stage coupler.

6.2 Conclusion

While telecommunications and other applications already use lasers to transmit information, current technologies are too expensive and bulky to be used across a wide range of industry. Integrated photonics research aims to bring down the dramatic cost of production and reach a data rates of more than one Tera bits per second. Tomorrow's datacenter or supercomputer may see components spread throughout a building or even an entire campus, communicating with each other at high speed, as opposed to being confined by heavy copper cables with limited capacity and reach. This will allow datacenter users, such as government agencies, universities, financial institutions, or internet companies like Google to increase their performance, and lower the costs in space and energy. With the success in magnetron sputtering As_2S_3 thin film and the fabrication of various active and passive hybrid devices on $LiNbO_3$ substrate, we have achieved the main purpose of this work. We have demonstrated the feasibility of a hybrid integration of As_2S_3 and $LiNbO_3$ waveguides with magnetron sputtering.

6.3 Future Work

First of all, The TM and TE propagation loss of As_2S_3 waveguide could still be lowered to reached the lowest ever reported value of about 0.05 dB/cm. This was obtained for a 4 μm wide ridge waveguide with a thickness of about 2 to 3 μm. It can be accomplished

by fine tuning the waveguide fabricating process and paying special attention on how to reduce the surface roughness of the As_2S_3 waveguide.

The net gain of the Er:Ti:$LiNbO_3$ waveguide amplifier can be further improved by increasing the overlap between the propagating mode profile of both the pump and signal, and the distribution of erbium in the amplifier. Based on some preliminary findings, both experimental and simulated, we have realized that a well-placed As_2S_3 waveguide near the Er:Ti:$LiNbO_3$ waveguide amplifier might alter the pump signal in such a way that the overall gain of the amplifier can be improved.

As for the doping of erbium into As_2S_3 film with multi-layer magnetron sputtering, we could upgrade the semi-cosputtering process to full co-sputtering. This would require the simultaneous sputtering of As_2S_3 and Er throughout the run. This should distribute the erbium even more evenly in the film and further decrease the cooperative upconversion of erbium in the erbium doped waveguide amplifier.

REFERENCES

1. A. Lamprechter, "Photonics – The key technology for tomorrow's computers and entertainment electronics," (2010), http://download.intel.com/pressroom/pdf/photonics/SiliconPhotonics_Backgrounder.pdf?iid=pr_smrelease_vPro_materials3.

2. R. Soref, and B. Bennett, "Electrooptical effects in silicon," Quantum Electronics, IEEE Journal of **23**, 123-129 (1987).

3. A. Liu, L. Liao, D. Rubin, H. Nguyen, B. Ciftcioglu, Y. Chetrit, N. Izhaky, and M. Paniccia, "High-speed optical modulation based on carrier depletion in a silicon waveguide," Opt. Express **15**, 660-668 (2007).

4. D. W. Kim, A. Barkai, R. Jones, N. Elek, H. Nguyen, and A. Liu, "Silicon-on-insulator eight-channel optical multiplexer based on a cascade of asymmetric Mach-Zehnder interferometers," Opt. Lett. **33**, 530-532 (2008).

5. M. Paniccia, "The 50G silicon photonics link " (2010), http://download.intel.com/pressroom/pdf/photonics/50G_Silicon_Photonics_Link.pdf?iid=pr_smrelease_vPro_materials1.

6. Y. Kang, L. Han-Din, M. Morse, M. Paniccia, M. Zadka, S. Litski, G. Sarid, A. Pauchard, K. Ying-Hao, C. Hui-Wen, W. Zaoui, J. Bowers, A. Beling, D. McIntosh, Z. Xiaoguang, and J. Campbell, "Monolithic germanium/silicon avalanche photodiodes with 340 GHz gain-bandwidth product," Nature Photonics **3**, 59-63 (2009).

7. Y. Vlasov, "Silicon integrated nanophotonics," (2010), http://domino.research.ibm.com/comm/research_projects.nsf/pages/photonics.index.html.

8. C. Andrews, "Made in IBM labs: breakthrough chip technology lights the path to exascale computing," (2010), http://www-03.ibm.com/press/us/en/pressrelease/33115.wss.

9. W. Sohler, H. Hu, R. Ricken, V. Quiring, C. Vannahme, H. Herrmann, D. Büchter, S. Reza, W. Grundkötter, S. Orlov, H. Suche, R. Nouroozi, and Y. Min, "Integrated optical devices in lithium niobate," Opt. Photon. News **19**, 24-31 (2008).

10. E. L. Wooten, K. M. Kissa, A. Yi-Yan, E. J. Murphy, D. A. Lafaw, P. F. Hallemeier, D. Maack, D. V. Attanasio, D. J. Fritz, G. J. McBrien, and D. E.

Bossi, "A review of lithium niobate modulators for fiber-optic communications systems," IEEE Journal of Selected Topics in Quantum Electronics **6**, 69-82 (2000).

11. T. J. Wang, and J. S. Chung, "Electrooptically wavelength-tunable polarization converter utilizing strain-optic effect on X-cut LiNbO3," IEEE Photonics Technology Letters **16**, 2275-2277 (2004).

12. H. Jung, and Y. Chung, "Polarization-independent electro-optically tuned add/drop multiplexers in LiNbO3 utilizing strain optic effect," Japanese Journal of Applied Physics **47**, 1579-1583 (2008).

13. M. Kazumasa, M. Masamitsu, and K. Jiro, "Optical waveguide isolator in Ti-diffused LiNbO3," Optics Communications **27**, 361-364 (1978).

14. M. Asobe, and K. i. Suzuki, "Nonlinear refractive index measurement in chalcogenic-glass fibers by self-phase modulation," Applied Physics Letters **60**, 1153 (1992).

15. S. Ramachandran, and S. Bishop, "Photoinduced integrated-optic devices in rapid thermally annealed chalcogenide glasses," IEEE Journal of Selected Topics in Quantum Electronics **11**, 260-270 (2005).

16. P. A. Young, "Optical properties of vitreous arsenic trisulphide," Journal of Physics C: Solid State Physics, 93 (1971).

17. V. Ta'eed, N. J. Baker, L. Fu, K. Finsterbusch, M. R. E. Lamont, D. J. Moss, H. C. Nguyen, B. J. Eggleton, D.-Y. Choi, S. Madden, and B. Luther-Davies, "Ultrafast all-optical chalcogenide glass photonic circuits," Opt. Express **15**, 9205-9221 (2007).

18. J. J. Hu, V. Tarasov, A. Agarwal, L. Kimerling, N. Carlie, L. Petit, and K. Richardson, "Fabrication and testing of planar chalcogenide waveguide integrated microfluidic sensor," Optics express **15**, 2307-2314 (2007).

19. M. E. Solmaz, W. C. Tan, O. Eknoyan, C. K. Madsen, D. B. Adams, X. Xia, and S. Grover, "Compact bends for achieving higher integration densities for LiNbO 3 waveguides," IEEE Photonics Technology Letters **21**, 557-559 (2009).

20. M. Solmaz, D. Adams, and W. Tan, "Vertically integrated As2S3 ring resonator on LiNbO3," Optics letters **34**, 1735-1737 (2009).

21. V. G. Ta'eed, S. Madden, B. Eggleton, K. Finsterbusch, D. Choi, D. Moss, H. Nguyen, N. Baker, M. R. E. Lamont, B. Luther-Davies, and L. Fu, "Ultrafast all-

optical chalcogenide glass photonic circuits," Optics Express **15**, 9205-9221 (2007).

22. J. F. Viens, C. Meneghini, A. Villeneuve, T. V. Galstian, E. J. Knystautas, M. A. Duguay, K. A. Richardson, and T. Cardinal, "Fabrication and characterization of integrated optical waveguides in sulfide chalcogenide glasses," Journal of Lightwave Technology **17**, 1184-1191 (1999).

23. R. G. DeCorby, N. Ponnampalam, M. M. Pai, H. T. Nguyen, P. K. Dwivedi, T. J. Clement, C. J. Haugen, J. N. McMullin, and S. O. Kasap, "High index contrast waveguides in chalcogenide glass and polymer," IEEE Journal of Selected Topics in Quantum Electronics **11**, 539-546 (2005).

24. S. Q. Gu, S. Ramachandran, E. E. Reuter, D. A. Turnbull, J. T. Verdeyen, and S. G. Bishop, "Photoluminescence and excitation spectroscopy of Er-doped As2S3 glass: Novel broad band excitation mechanism," Journal of Applied Physics **77**, 3365 (1995).

25. A. Fuchs, J. Fick, V. Balan, C. Vigreux, and A. Pradel, "Photoluminescence and waveguiding in sputtered films of Er-doped chalcogenide glasses," Proceedings of SPIE **5451**, 327-336 (2004).

26. C. Meneghini, J. F. Viens, A. Villeneuve, É. J. Knystautas, M. A. Duguay, and K. A. Richardson, "Luminescence from neodymium-ion-implanted As2S3 waveguides," Journal of the Optical Society of America B **15**, 1305-1308 (1998).

27. S. H. E. Wong, "Inorganic arsenic trisulfide photoresist for three-dimensional photolithography," in *Faculty of Chemistry and BioSciences* (Karlsruhe Institute of Technology, Karlsruhe, Germany, 2008), p. 225.

28. W. C. Tan, "Optical properties of amorphous selenium films," in *Electrical Engineering* (University of Saskatchewan, Saskatoon, 2006), p. 128.

29. N. F. Mott, "Electrons in disordered structures," Advances in Physics **50**, 865-945 (2001).

30. M. H. Cohen, "Review of the theory of amorphous semiconductors," Journal of Non-Crystalline Solids **4**, 391-409 (1970).

31. J. M. Marshall, and A. E. Owen, "Drift mobility studies in vitreous arsenic triselenide," Philosophical Magazine **24**, 1281 (1971).

32. J. Tauc, *Amorphous and liquid semiconductors* (Plenum, New York, 1974).

33. J. Singh, and K. Shimakawa, *Advances in amorphous semiconductors* (Taylor & Francis, London, 2003).

34. W. C. Tan, K. Koughia, J. Singh, and S. O. Kasap, "Fundamental optical properties of materials I," in *Optical properties of condensed matter and applications*, J. Singh, ed. (John Wiley & Sons Ltd, West Sussex, 2006), pp. 1-25.

35. S. H. Wemple, and Didomeni.M, "Behavior of the electronic dielectric constant in covalent and ionic materials," Physical Review. B, Solid State **3**, 1338 (1971).

36. P. J. L. Herve, and L. K. J. Vandamme, "Empirical temperature dependence of the refractive index of semiconductors," Journal of Applied Physics **77**, 5476 (1995).

37. C. Lopez, "Evaluation of the photo-induced structural mechanisms in chalcogenide glass materials," in *College of Optics and Photonics* (University of Florida, Orlando, 2004), p. 231.

38. R. P. Wang, A. Rode, S. Madden, and B. Luther-Davies, "Physical aging of arsenic trisulfide thick films and bulk materials," Journal of the American Ceramic Society **90**, 1269-1271 (2007).

39. J. S. Berkes, S. W. Ing, and W. J. Hillegas, "Photodecomposition of amorphous As2Se3 and As2S3 " Journal of Applied Physics **42**, 4908 (1971).

40. H. Hisakuni, and K. Tanaka, "Giant photoexpansion in As2S3 glass," Applied Physics Letters **65**, 2925-2927 (1994).

41. Z. Yang, N. C. Anheier, H. A. Qiao, and P. Lucas, "Simultaneous microscopic measurements of photodarkening and photoexpansion in chalcogenide films," Journal of Physics D: Applied Physics **42**, 135412-135416 (2009).

42. K. Tanaka, A. Saitoh, and N. Terakado, "Giant photo-expansion in chalcogenide glass," Journal of Optoelectronics and Advanced Materials **8** (2006).

43. M. Solmaz, X. Cheng, H. Park, and C. K. Madsen, "Patterning chalcogenide glass by direct resist-free thermal nanoimprint," Journal of Vacuum Science & Technology. B, Microelectronics and Nanometer Structures **26**, 606-610 (2008).

44. Y. L. Ruan, W. T. Li, R. Jarvis, N. Madsen, A. Rode, and B. Luther-Davies, "Fabrication and characterization of low loss rib chalcogenide waveguides made by dry etching," Optics Express **12**, 5140-5145 (2004).

45. D. Y. Choi, S. Madden, A. Rode, R. P. Wang, and B. Luther-Davies, "Advanced processing methods for As2S3 waveguide fabrication," in *IEEE Conference on Optoelectronic and Microelectronic Materials & Devices* (IEEE 2006), pp. 132-135.

46. A. V. Rode, R. B. Charters, B. Luther-Davies, A. Zakery, E. G. Gamaly, and M. Samoc, "Laser-deposited As2S3 chalcogenide films for waveguide applications," Applied Surface Science **197-198**, 481-485 (2002).

47. P. J. Allen, B. R. Johnson, R. T. Baran, N. C. Anheier, S. K. Sundaram, M. H. Engelhard, and B. T. Broocks, "Surface degradation of As2S3 thin films," Physics and Chemistry of Glasses **47**, 681-687 (2006).

48. J. Dikova, N. Starbov, and K. Starbova, "The mechanism of photoinduced transformations in amorphous As2S3 thin films," Journal of Non-Crystalline Solids **167**, 50-58 (1994).

49. W. C. Tan, M. E. Solmaz, J. Gardner, R. Atkins, and C. Madsen, "Optical characterization of a-As2S3 thin films prepared by magnetron sputtering," Journal of Applied Physics **107**, 033524 (2010).

50. W. S. Rodney, I. H. Malitson, and T. A. King, "Refractive Index of arsenic trisulfide," Journal of the Optical Society of America **48**, 633-635 (1958).

51. S. A. Keneman, J. Bordogna, and J. N. Zemel, "Evaporated films of arsenic trisulfide: dependence of optical properties on light exposure and heat cycling " Journal of the Optical Society of America **68**, 32-38 (1978).

52. G. Stewart, R. H. Hutchins, and P. J. R. Laybourn, "Controlled growth of arsenic trisulphide films for coupling integrated optical devices " Journal of Physics. D, Applied Physics **14**, 323-331 (1981).

53. A. R. Hilton, G. Whaley, and J. McCord, "Production of arsenic trisulfide glass," Proceedings of SPIE **3060**, 335-343 (1997).

54. J. Tauc, and A. Menth, "States in the gap," Journal of Non-Crystalline Solids **8-10**, 569-585 (1972).

55. D. L. Wood, and J. Tauc, "Weak absorption tails in amorphous semiconductors," Physical Review. B, Solid State **5**, 3144-3151 (1972).

56. P. J. Allen, B. R. Johnson, and B. J. Riley, "Photo-oxidation of thermally evaporated As2S3 thin films," Journal of Optoelectronics and Advanced Materials **7**, 1759-1764 (2005).

57. R. Kawakami, and T. Inaoka, "Effect of argon plasma etching damage on electrical characteristics of gallium nitride," Vacuum **83**, 490-492 (2008).

58. M. K. Bahl, R. O. Woodall, R. L. Watson, and K. J. Irgolic, "Relaxation during photoemission and LMM auger decay in arsenic and some of its compounds " The Journal of Chemical Physics **64**, 1210-1218 (1976).

59. N. Fairley, and A. Carrick, *The casa cookbook: recipes for XPS data processing* (Acolyte Science, Knutsford, U. K. , 2005).

60. S. Seal, K. A. Richardson, C. Lopez, A. Graham, D. K. Verma, A. Saliminia, T. Galstian, and A. Villeneuve, "Structure and chemical studies of As2S3 glasses used for waveguide applications," Physics and Chemistry of Glasses **43**, 59-65 (2002).

61. J. Noda, M. Fukuma, and S. Saito, "Effect of Mg diffusion on Ti-diffused LiNbO3 waveguides " Journal of Applied Physics **49**, 3150-3154 (1978).

62. C. Canali, C. De Bernardi, M. De Sario, A. Loffredo, G. Mazzi, and S. Morasca, "Effects of water vapor on refractive index profiles in Ti:LiNbO3 planar waveguides," Journal of Lightwave Technology **4**, 951-955 (1986).

63. B. Chen, "Elimination of LiO2 out-diffusion waveguide in LiNbO3 and LiTaO3," Applied Physics Letters **30**, 570 (1977).

64. D. Y. Choi, S. Madden, D. A. Bulla, R. Wang, A. Rode, and B. Luther-Davies, "Submicrometer-thick low-loss As2S3 planar waveguides for nonlinear optical devices," Photonics Technology Letters, IEEE **22**, 495-497 (2010).

65. J. Hu, N. Carlie, L. Petit, A. Agarwal, K. Richardson, and L. Kimerling, "Demonstration of chalcogenide glass racetrack microresonators," Opt. Lett. **33**, 761-763 (2008).

66. D. L. Zhang, P.-R. Hua, and E. Y. B. Pun, "Correct determination of net gain in Er-doped optical waveguide amplifier from pump-on/off measurement," Optics Communications **279**, 64-67 (2007).

67. R. Brinkmann, I. Baumann, M. Dinand, W. Sohler, and H. Suche, "Erbium-doped single- and double-pass Ti:LiNbO3 waveguide amplifiers," Quantum Electronics, IEEE Journal of **30**, 2356-2360 (1994).

68. Kogahara, "Optical amplification characteristics of Ti-diffused waveguides on Erbium-doped LiNbO3 crystal," IEICE Electronics Express **4** (2007).

69. R. Salas-Montiel, M. E. Solmaz, W. C. Tan, X. Song, W. T. Snider, and C. K. Madsen, "Selective co-doped erbium Ti:LiNbO3 waveguide amplifiers," Proceedings of SPIE **7605**, 76050L-76058 (2010).

70. J. A. Frantz, J. S. Sanghera, L. B. Shaw, G. Villalobos, I. D. Aggarwal, and D. W. Hewak, "Sputtered films of Er3+-doped gallium lanthanum sulfide glass," Materials Letters **60**, 1350-1353 (2006).

71. V. Lyubin, M. Klebanov, B. Sfez, and B. Ashkinadze, "Photoluminescence and photodarkening effect in erbium-doped chalcogenide glassy films," Materials Letters **58**, 1706 (2004).

72. J. Fick, E. J. Knystautus, A. Villeneuve, F. Schiettekatte, S. Roorda, and K. A. Richardson, "High photoluminescence in erbium-doped chalcogenide thin films," Journal of Non-Crystalline Solids **272**, 200-208 (2000).

73. S. Wong, O. Kiowski, M. Kappes, J. K. N. Lindner, N. Mandal, F. C. Peiris, G. A. Ozin, M. Thiel, M. Braun, M. Wegener, and G. von Freymann, "Spatially localized photoluminescence at 1.5 micrometers wavelength in direct laser written optical nanostructures," Advanced Materials **20**, 4097 (2008).

VITA

Name: Wee Chong Tan

Address: Department of Electrical and Computer Engineering,
Texas A&M University,
214 Zachry Engineering Center, TAMU 3128
College Station, Texas 77843-3128

Email Address: weechng@tamu.edu

Education: B. Sc., Electrical and Computer Engineering, University of Saskatchewan, 2003.
M. Sc., Electrical and Computer Engineering, University of Saskatchewan, 2006.
Ph.D., Electrical Engineering, Texas A&M University 2011.